SINGLE-MOLECULE FLUORESCENCE MICROSCOPY OF MOLECULAR INTERACTIONS AT REVERSED-PHASE CHROMATOGRPAHIC INTERFACES

by

Justin T. Cooper

A dissertation submitted to the faculty of
The University of Utah
in partial fulfillment of the requirements for the degree of

Doctor of Philosophy

Department of Chemistry

The University of Utah

December 2014

The University of Utah Graduate School

STATEMENT OF DISSERTATION APPROVAL

The dissertation of **Justin T. Cooper**

has been approved by the following supervisory committee members:

Joel M. Harris	, Chair	**7/23/2014** Date Approved
Jennifer S. Shumaker-Parry	, Member	**7/23/2014** Date Approved
Marc D. Porter	, Member	**7/23/2014** Date Approved
Michael H. Bartl	, Member	**7/23/2014** Date Approved
Vladimir Hlady	, Member	**7/23/2014** Date Approved

and by **Cynthia J. Burrows**, Chair/Dean of

the Department/College/School of **Chemistry**

and by David B. Kieda, Dean of The Graduate School.

ABSTRACT

The development of techniques to probe molecular transport and the dynamics of molecular interactions at interfaces is important for understanding and optimizing surface-based technologies including surface-enhanced spectroscopies, biological assays, sensors, catalysis, and chemical separations. In particular, the efficiency and resolution of separation via reversed-phase liquid chromatography is governed by the interaction of analytes with the solution/stationary phase interface. Most commonly, the stationary phase material consists of high surface area, micron-sized, mesoporous silica particles functionalized with n-alkane ligands. Understanding the timescales at which analyte molecules are transported through the interior of the particle, as well as adsorbed and desorbed from the particle surface, is of fundamental importance in the development of new, more efficient chromatographic materials.

Probing chemical interactions at interfaces is difficult due to the selectivity needed to measure the small population of molecules at an interface versus bulk solution. Measuring interfacial chemical interactions within chromatographic particles has the added challenge that the majority of the surface area is contained within the particle making it difficult to measure interfacial processes directly.

In this work, single-molecule spectroscopic techniques are used to measure the transport and adsorption/desorption kinetics of molecules at planar reversed-phase chromatographic interfaces and within reversed-phase chromatographic particles.

Fluorescence imaging with single-molecule tracking is used to track the locations of fluorescent molecules during their retention within chromatographic particles. This yields information regarding their diffusion rates and their residence time within the particle. Statistical criteria based on the single-molecule localization resolution are also developed to characterize the population of strongly adsorbed molecules and their effect on intraparticle molecular residence times.

Fluorescence imaging is also combined with fluorescence-correlation spectroscopy and used to measure fast interfacial transport and sorption kinetics at planar models of chromatographic interfaces. This technique has higher temporal resolution relative to imaging and is capable of measuring transport approaching free solution diffusion rates of small molecules.

Finally, a comparison is made between interfacial transport rates and surface populations measured at planar chromatographic interfacial models versus within porous particles. It is found that n-alkyl modified planar interfaces are reasonable models for reversed-phase chromatographic particles with proper interpretation of measured parameters.

To my wife, Cindy, who makes me a better person.

TABLE OF CONTENTS

ACKNOWLEDGMENTS

I would like to extend my sincere thanks to all those who help and influenced me these past 6 years. Firstly, I would like to acknowledge my research advisor, Dr. Joel Harris, who has kindly and patiently mentored me through my graduate school career. His knowledge of chemistry has been an indispensable resource and his tireless dedication to research has been an inspiration to me through all my "afternoons in the lab."

I would like to extend thanks to Dr. Karen Seaward who was our liaison with Agilent Technologies, Inc. Through her, we received samples and funding that were used in a large portion of my work.

I would also like to thank all the members of the Harris group with whom I have had the pleasure of working alongside. Dr. Emily Heider taught me epifluorescence imaging, which was the first thing I learned how to do in the group. Dr. Eric Peterson taught me single-molecule fluorescence imaging and Matlab programming and has been my officemate for the past 5 years. He has always been willing to share his scientific insight, lend help, and of course provide current socio-political-economic commentary. Doug Kriech always knew where everything was kept in the lab and has been an excellent resource to the Utah outdoors. Mike Manhart has always up for a bike ride when the science was getting frustrating. I also appreciate all other Harris group members who have always been willing to help, Dr. Jonathan Schaefer, Dr. Grant

Meyers, Dr. Charlie Ma, Dr. Jennifer Gasser-Ramirez, Dr. Moussa Barhoum, Chris Hardcastle, Jay Kitt, Natascha Knowlton, and David Bryce.

Finally, I would like to thank my parents, family, and friends who have always believed in me. Most importantly, thank you to my wonderful wife, Cindy, whose patience and empathy have been the source of the most strength as we both passed through the graduate school gauntlet together.

CHAPTER 1

INTRODUCTION

1.1 Interfacial Dynamics

Over the last several decades there has been an increased interest in the study of the chemistry of solid/liquid and liquid/liquid interfaces. This interest has been driven by the development of technologies requiring a deeper understanding of interfacial phenomena. Chemical interactions at interfaces are critical to the advancement of a wide range of technologies including heterogeneous catalysis,[1] chromatographic separations,[2] chemical sensors,[3] extraction processes,[4] drug delivery systems,[5] and model biological membranes.[6] To provide surface capacity for these applications, porous, high surface area materials are often utilized. Chromatographic separations, for example, rely on the degree to which molecules are retained on the surface of chromatographic media, which are generally porous materials with specific surface areas between 10^2 and 10^3 m^2/g and a surface area to volume ratio of approximately 10^6 m^{-1}. Thus, *interfacial* processes, as opposed to bulk solution interactions, dominate the chemical interactions occurring within these materials. Of particular importance is how molecular transport and chemical reactions at interfaces are influenced by surface phenomena. The kinetics of chemical reactions at interfaces are governed by rates of transport of molecules to the surface from solution, rates of adsorption and desorption, and lateral diffusion of adsorbed molecules

to reaction sites on the surface (Figure 1.1).[7] Adsorption can encompass varying degrees of interaction with the surface. Chemisorption involves the formation of a chemical bond between the molecule and the surface, while physisorption refers to molecules adsorbed due to attractive physical forces such as electrostatic or van der Waals forces or hydrophobic interactions, which drive organic solutes out of aqueous solution to lower the surface free energy.[8] The extent to which a molecule is adsorbed, along with energies associated with desorption and transport on the surface, influence the residence time of the molecule at the interface and its surface mobility, respectively. Analogous to the dependence of traditional bulk solution reaction rates on the collision frequency of reactants, the interfacial processes of adsorption, desorption, and surface diffusion rates contribute to the frequency of encounters between reacting molecules or between molecules and reaction sites at the interface.[9]

1.2 Dynamic Processes at Chromatographic Interfaces

Chromatographic separations are an example of an application dominated by interfacial dynamics. Chromatographic stationary phases generally are comprised of an interaction ligand, which controls the mode of chemical separation (normal-phase, reversed-phase, ion-exchange, etc.) bonded to a silica-gel support particle. Chromatographic silica particles are typically generated through gelling of colloidal silica into larger three-dimensional aggregates with pores being formed by the interstices between the discrete particles. These hydrogels are then dehydrated and sintered at high temperature to form xerogels, followed by hydrothermal treatment to produce porous particles with a larger average pore diameter and narrow pore size distribution.[10,11] Characterization of the pore structure of porous silica particles has been conducted via

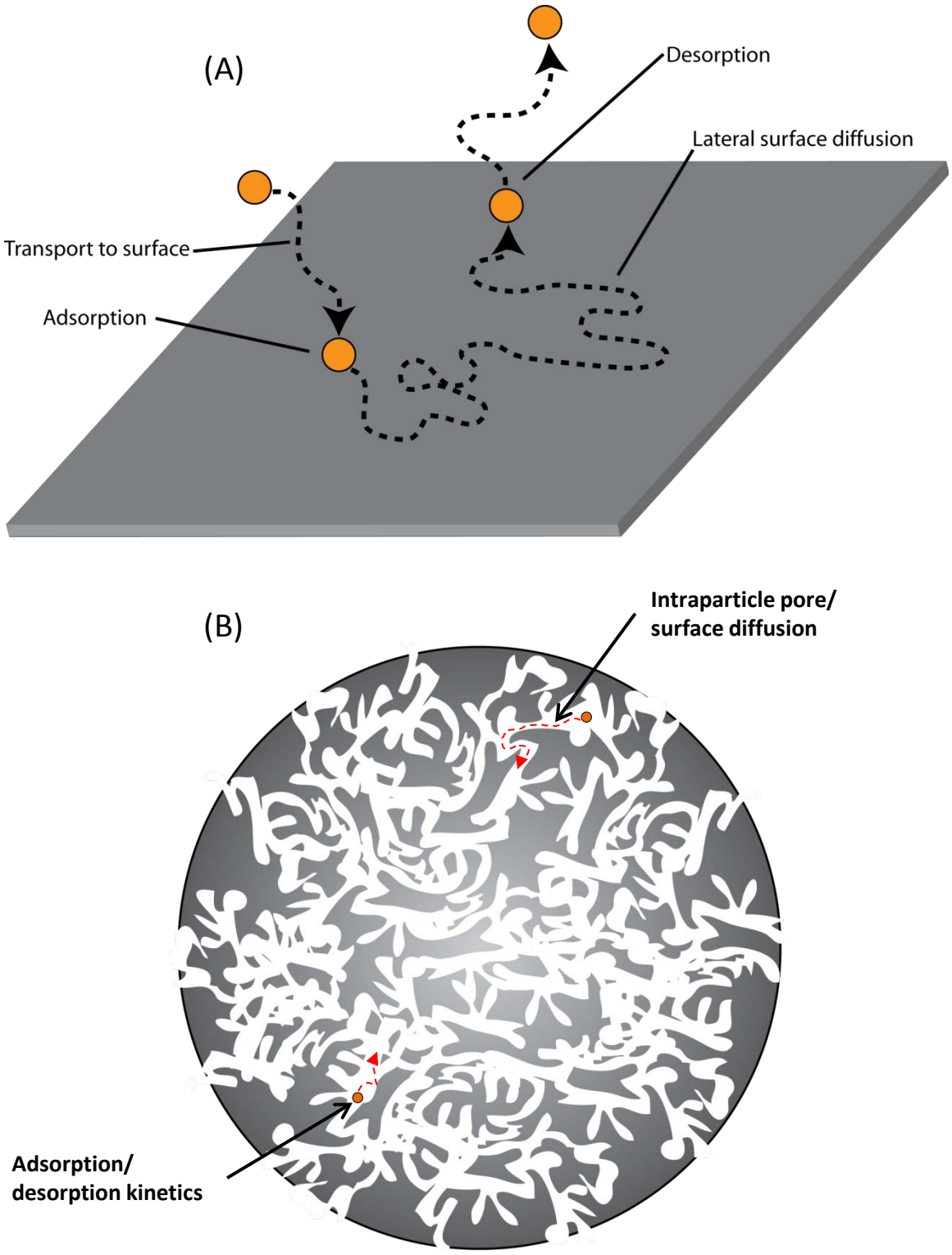

Figure 1.1. Interfacial processes of adsorption, desorption, and lateral surface diffusion at (A) planar interfaces and (B) within porous particles.

small angle neutron scattering, which gives the average distances between the interfaces of differing scattering densities (pores vs. silica). Results indicate that the pore structure permeates the particle in three dimensions with distances between scattering surfaces comparable to pore diameters measured via mercury porosimetry.[12,13] The internal pore structure provides a high specific surface area (~10^2 m^2/g) on which analyte molecules can adsorb and be retained in the stationary phase. In addition to molecular adsorption and desorption, there are intraparticle transport phenomena, surface diffusion of analyte molecules adsorbed to the intraparticle surface, and pore diffusion through the solution phase in the void fraction of the particle (Figure 1.1b). The rates at which each of these processes occur collectively govern the macro scale chromatographic experimental retention time and dispersion of analyte molecules. The heterogeneity of these processes is also important and has an effect on the band shape and, consequently, the separation efficiency and resolution. The development of more efficient chromatographic media necessitates a fundamental understanding of analyte-stationary phase interactions and analyte transport within the chromatographic particles. This requires the development of analytical methodologies capable of measuring phenomena occurring at the solution-stationary phase interface.

1.3 Measuring Sorption and Transport Dynamics at Chromatographic Interfaces

Characterizing the dynamics of molecular interactions at chromatographic interfaces has long represented a measurement challenge due to the buried nature of the interface. First, the interface represents an infinitesimally small region buried between two phases. In liquid chromatography, these phases generally consist of the mobile

solution phase through which the analyte sample is initially introduced and a solid stationary phase, which consists of a chemically modified silica substrate. The population of analyte molecules at the interface is generally small relative to the bulk solution phase[8], thus interfacial probing techniques must be selective toward the surface population over background signals from molecules in the bulk phases. Furthermore, in the case of the use of porous silica particles as the stationary phase support, the majority (>99%) of the surface area and interfacial region is contained *within* the particles. Thus, an effective analytical technique must be able to probe analyte/stationary phase interactions that are taking place deep within the interior of the porous structure.

Traditionally, characterization of interfacial sorption and transport kinetics within porous chromatographic media has employed chromatographic based techniques. The kinetics of adsorption and desorption have been investigated through analysis of chromatographic breakthrough curves.[14–17] Techniques including frontal analysis and the perturbation or pulse-response method[18–20] have been pioneered by Guiochon and coworkers for measuring both adsorption/desorption kinetics and intraparticle transport. Intraparticle sorption kinetics and transport have typically been treated as contributing to resistance-to-mass-transfer in expressions for the height-equivalent-of-a-theoretical-plate.[21–23] Recently, particular attention has been directed toward determining the contribution of surface diffusion to transport efficiency within porous particles and its effect on chromatographic peak shapes.[24–26] These techniques rely on analysis of elution profiles to infer the kinetic parameters governing the contributions of adsorption/desorption kinetics and intraparticle transport to overall retention times and separation efficiency.

Spectroscopic techniques have also been employed in kinetic studies at chromatographic interfaces. Pioneering fluorescence work was done by Bogar et al. and Staahlberg et al. on the fluid nature of the C_{18} alkyl chains at the surface of reversed-phase liquid chromatographic (RPLC) packings, where fluorescence detection of excimer formation was indicative of mobile solute molecules at a fluid like RPLC interface.[27,28] Fluorescence-recovery after photobleaching (FRAP) has also been used to measure surface diffusion coefficients of aromatic molecules at C_{18}-modified, planar fused silica surfaces along with the effect of varying solvent composition on diffusion rates.[29–31] Ludes et al. used wide-field fluorescence microscopy to measure the desorption kinetics of organic bases from RP-modifed planar fused silica and silica gel.[32,33] Mixed-mode desorption kinetics were observed and attributed to the heterogeneity of surface sites toward analyte adsorption, where weak adsorption occurs at the organic monolayer, while strong adsorption occurs at residual surface silanols on the silica surface. These strong adsorption interactions are thought to be the source of peak-tailing in chromatography (Figure 1.2).[34]

1.4 Single-Molecule Microscopy at Chromatographic Interfaces

Spectroscopic methods of instrumentation and techniques geared toward the analysis of interfaces have advanced considerably in recent years, in many cases reaching single molecule detection limits.[35,36] While the earliest single-molecule studies were directed at doped in cryogenic crystals at low temperatures,[37] single-molecule techniques have seen widespread use in a variety of applications, such as measuring binding kinetics in biorecognition,[38] high-resolution intracellular imaging,[39] and probing local electric-field environment on plasmonic nanoparticles.[40] Single-molecule methods allow one to

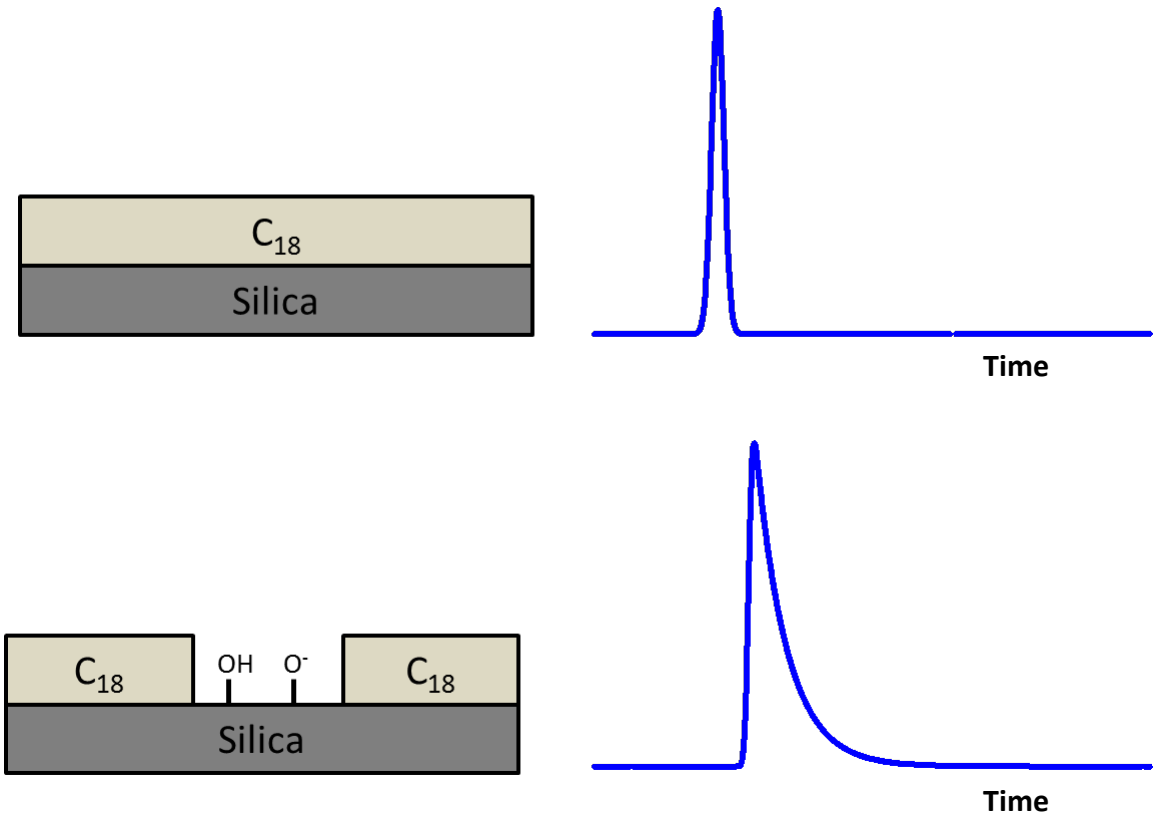

Figure 1.2. Incomplete surface modification leads to strong adsorption sites at free *active* silanols. The heterogeneous adsorption behavior caused by these sites has been linked to peak-tailing in chromatographic experiments.

probe the distribution of chemical behavior of individual molecular events that lead to traditionally measured ensemble properties. This ability has been exploited to measure the heterogeneity of interfacial processes occurring at chromatographic surfaces. Wirth et al. used fluorescence bursts of single 1,1‘-dioctadecyl-3,3,3‘,3‘-tetramethylindocarbocyanine perchlorate (DiI) molecules detected with confocal microcopy to probe mixed-mode adsorption at a water/C_{18}-modifed silica interface. The duration of fluorescence bursts were analyzed, and short bursts were attributed to weakly adsorbed molecules undergoing rapid surface diffusion and quickly traversing the focused laser beam, while longer lived fluorescence bursts were attributed to strongly adsorbed molecules “stuck” in strong adsorption sites. Recently, the surface selectivity and low background afforded by techniques such as confocal and total-internal-reflection-fluorescence microscopy (TIRF) combined with the spatial information gained from single-molecule imaging and the high time resolution of fluorescence correlation spectroscopy (FCS) have pushed these single-molecule methods to the forefront of spectroscopic analysis of chromatographic interfaces.[34]

1.5 Fluorescence Imaging of Single-Molecule Retention Trajectories in Reversed Phase Chromatographic Particles

In Chapter 2, single-molecule fluorescence imaging, in an epi-illumination/collection geometry, is used to observe transport of individual hydrophobic dye molecules of octadecyl rhodamine B (R18) within RPLC porous silica particles, as is shown in Figure 1.3. This technique allows direct measurement of intraparticle molecular residence times, intraparticle diffusion rates, and the spatial distribution of molecules within the particle.[41] Fluorescence imaging of molecular trajectories is a

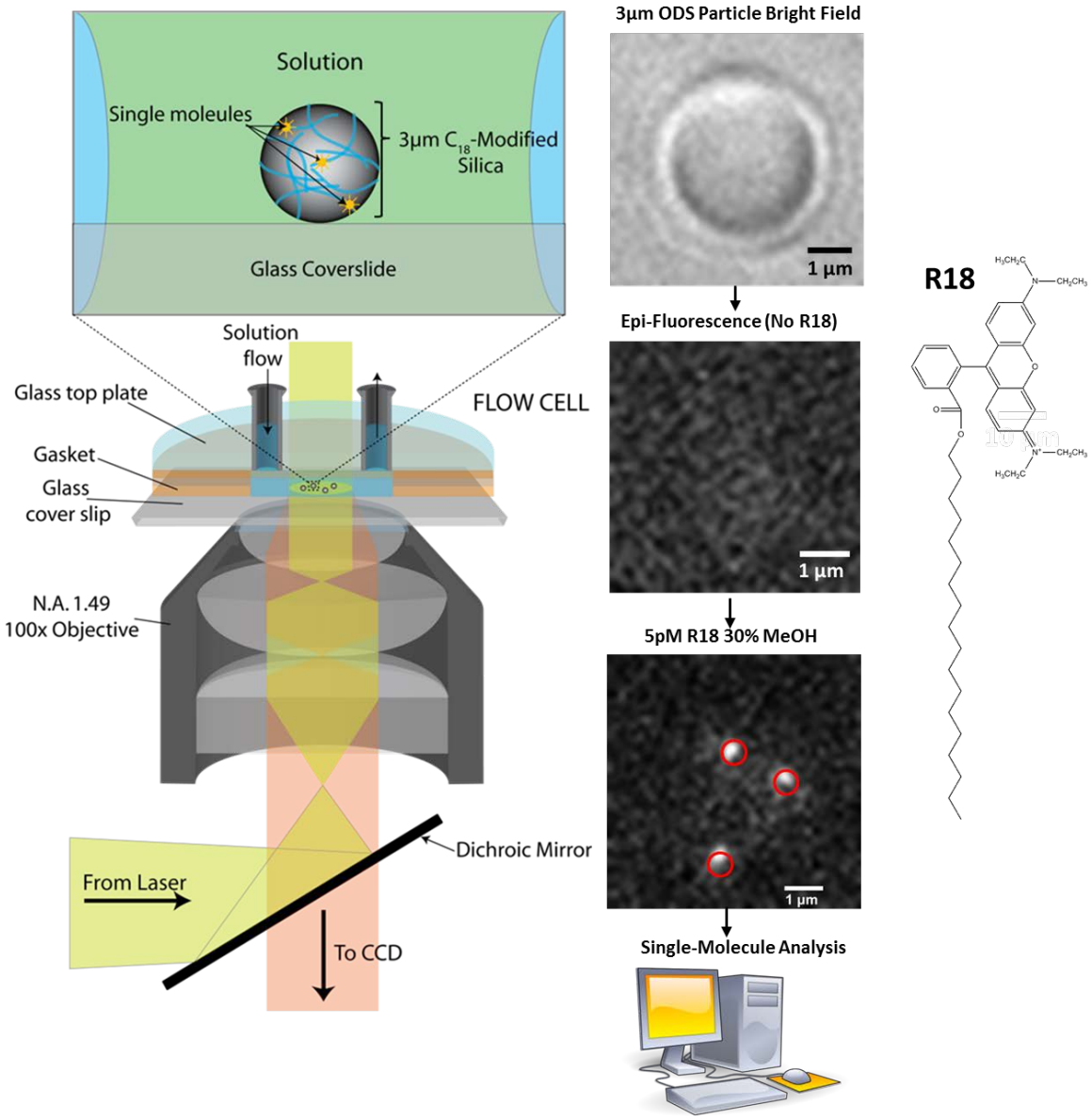

Figure 1.3. Epi-fluorescence illumination/collection instrumental setup for single-molecule fluorescence imaging within chromatographic silica particles.

particular example of single-molecule spectroscopic methods in which the fluorescence emission of probe molecules is collected and focused onto an array detector such as an electron-multiplied-charged-coupled-device (EMCCD) camera. Contrary to observation at a fixed illuminated spot, this method allows the simultaneous detection of many single-molecule events over a large area. A sequence of images is taken, which allows for the kinetics of single-molecule events to be extracted. For information to be gathered, molecules must first be identified and localized. Single-molecule localization has been the subject of great interest in recent years with attention being given to localization with subdiffraction spatial resolution. One approach is to fit single-molecule fluorescence images to a 2D-Gaussian function, which closely approximates the theoretical diffraction limited point-spread-function (PSF).[42–44]

In this work, we employ a single-molecule localization algorithm based on intensity thresholding, where molecules are identified by locating 3 adjacent pixels above a threshold value ($\mu_{bkg}+2.5\sigma_{bkg}$) determined from the single pixel distribution of background noise.[45] The false positive probability for detecting a single pixel above threshold that is actually from background noise (α) can be calculated from the single pixel distribution of background noise (~2%). Including the spatial criterion of 3 adjacent pixels above threshold for molecular identification lowers the false positive rate through combinatorial statistics ($\sim\alpha^3$).[45] The precise location of each molecule is then obtained by calculation of the intensity center of mass. Quantifying the number of molecules within the porous particles yields the equilibrium constant for partition between the mobile phase and stationary phase, which in turn can be related to the chromatographic retention parameter, *k'*, defined as the ratio of the number of molecules

in the stationary phase to those in the mobile phase, N_s/N_m.

For time-dependent information to be extracted, identified molecules in each frame must be correlated in space and time in order to track their motions. This method has been used for measuring transport of proteins in lipid bilayers;[46,47] characterizing the behavior of amphiphilic dyes interacting with stimulus-responsive thin films;[48,49] measuring the diffusion of labeled alkanoic acids of various chain lengths at a methylated silica-water interface;[50] and to investigate the influence of pore structure and chemical interactions on molecular transport within the porous thin silica sol-gel films.[51–55] The location of an identified molecule in one frame, *i*, is compared with locations of molecules in a subsequent frame, *j*, by calculating the root-mean-squared displacment, r_{ij}:

$$r_{ij} = \sqrt{(x_j - x_i)^2 + (y_j - y_i)^2} \qquad [1.1]$$

Displacements that are within a maximum displacement criterion, r_{max}, which establishes the 99% confidence bounds for the root-mean-squared displacement, are identified as a displacement of the same molecule between frames and are stitched together to form a trajectory, as is shown in Figure 1.4, while displacements larger than r_{max} are treated as distinct molecules. The trajectories of R18 molecules within the porous particles can then be analyzed for kinetic information such as the intraparticle molecular residence times, where the residence time is equal to the duration of the trajectory in frames multiplied by the acquisition rate (0.03 ms/frame). The diffusion coefficient is calculated from a mean-squared-displacement versus time analysis, where the displacements of molecules between frames are measured. The heterogeneity in the transport behavior

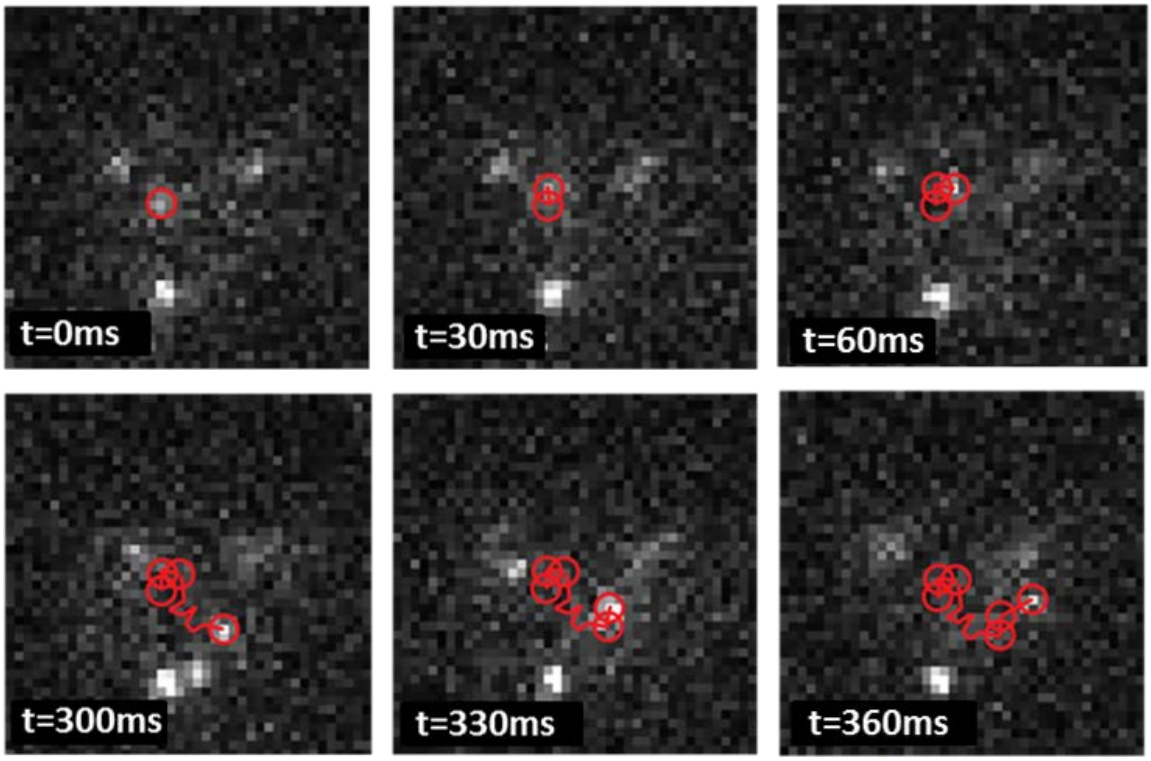

Figure 1.4. Example of single-molecule location tracking over several frames.

within the porous particles can also be investigated. This is accomplished by developing statistical criterion based on the localization uncertainty and characteristic measured diffusion rates to resolve the frame-to-frame behavior of molecules into moving and "stuck" events, where stuck events are when the motion of the molecule is arrested and the molecule remains stationary for a period of time. Moving events are attributed molecules interacting weakly with the stationary phase, while stuck events represent molecules strongly adsorbed to the stationary phase surface. Imaging data can also be used to characterize the stuck events in terms of their spatial distribution within the particle to identify problematic defect sites in the stationary phase surface where free, isolated silanols to which R18 molecules have strong affinity.[2,32,34]

While single-molecule imaging and tracking has yielded a great deal of information regarding transport and heterogeneity within actual reversed-phase chromatographic material, the technique is limited by its inherent time resolution to measuring dynamics at slower timescales. This limitation comes from the exposure time needed to acquire enough photons to achieve a signal-to-noise ratio sufficiently high to identify and track molecules.[44,46,56,57] When molecular motion is fast compared to the exposure time or detector readout time, the single-molecule fluorescence is spread over the pixel area traversed by the molecule during the acquisition which lowers the signal-to-noise ratio, making it difficult to identify and track molecules. This has limited single-molecule imaging experiments to high retention conditions ($k' > 400$) where surface diffusion is slow compared to the minimum CCD readout time, and the PSF of molecules are well resolved. To measure interfacial dynamics occurring at faster timescales, other techniques with higher temporal resolution must be employed, such as fluorescence

correlation spectroscopy.

1.6 Imaging-Fluorescence-Correlation Spectroscopy for Measuring Fast Surface Diffusion at Liquid/Solid Interfaces

Fluorescence correlation spectroscopy (FCS) has been used for decades for time-dependent phenomena in solution and at interfaces.[58] Since its introduction, FCS has been used for measuring translational diffusional coefficients,[58–60] kinetic rate constants,[61–63] rotational diffusion,[64,65] and photophysics of chromophores.[66–68] Fluorescence correlation spectroscopy involves the measurement of fluctuations in fluorescence intensity that arise from the spontaneous concentration fluctuations of a system about its equilibrium value due to the small number of molecules being observed. In many ways this is analogous to traditional perturbation-relaxation methods, where rapid perturbation of the equilibrium is induced by stepping the temperature, pressure, or electric field strength, and the subsequent relaxation to the new equilibrium is measured.[69] However, in FCS the equilibrium is not externally perturbed but instead arises from *natural* fluctuations and relaxations about the equilibrium from a small number of molecules, the measurement of which yields the same kinetic information.[61] For the case of diffusion, for example, the average number of molecules within a volume, *V*, within a system with a fixed concentration, *C*, is given by $\langle N \rangle = V * C$, as is shown in Figure 1.5A. However, at any given time the actual number of molecules in *V* fluctuates about $\langle N \rangle$ by a standard deviation given by Poisson statistics, where $\sigma_N = \langle N \rangle^{1/2}$. The rate at which the fluctuation occurs is governed by the rate at which molecules diffuse through *V*. The timescale at which this fluctuation occurs can be extracted via autocorrelation of the fluorescence intensity time trace, *F(t)*, which calculates the self-

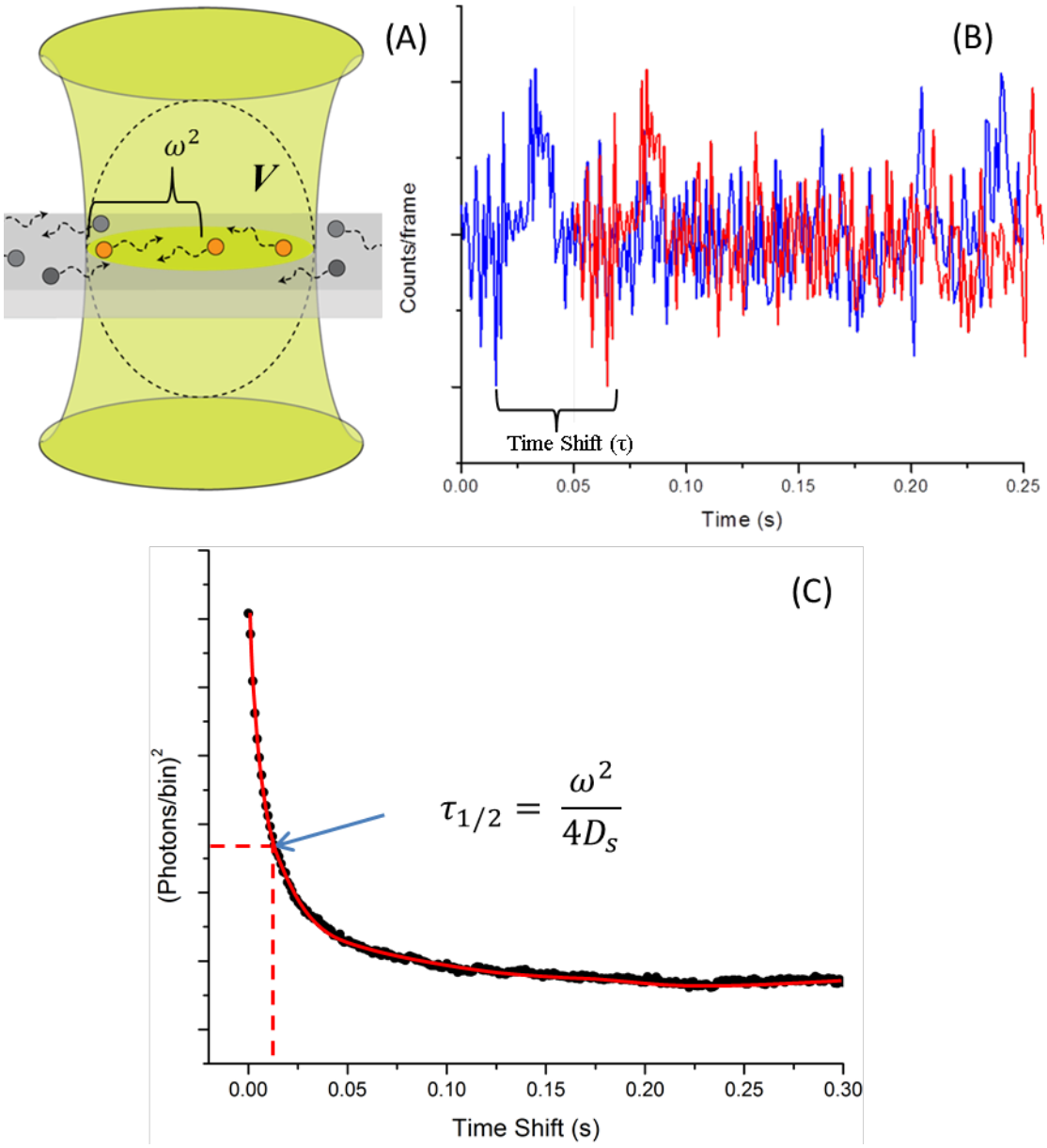

Figure 1.5. Surface diffusion measurement by FCS. (A) Probed volume of confocal FCS at an interface. (B) Fluorescence time trace is autocorrelated. (C) Autocorrelation function is fit to a transport model with the decay time ($\tau_{1/2}$) related to the diffusion coefficient (D_s) via the Einstein relation.

similarity of the fluorescence signal at varying time shift (τ):

$$G(\tau) = \lim_{T\to\infty} \frac{1}{T} \int_{-T/2}^{T/2} F(t)F(t+\tau)dt \qquad [1.2]$$

as is shown in Figure 1.5B. The calculated autocorrelation function decays with a characteristic time that is related to the time scale of the dynamic processes being probed (diffusion, chemical reaction, etc.) and can then be fit to an appropriate physical model, which includes these rates as parameters, as is shown in Figure 1.5C. For the small concentration fluctuations to be detected, the probing region is generally limited to only a small volume (<1 fl) containing only a few molecules. This is typically accomplished by confocal microscopy.[70] However, for the case of interfacial analysis, the depth resolution of the focused laser beam passing through the interface is relatively small (~1 um).[71] Total-internal-reflection fluorescence correlation spectroscopy (TIR-FCS) was developed by Thompson and coworkers to measure the lateral diffusion and adsorption/desorption kinetics of molecules at surfaces.[62] Total-internal-reflection-fluorescence microscopy is accomplished by impinging a laser beam from a high refractive index (n_1) material (glass or fused silica) to a lower refractive index (n_2) material (aqueous solution) at an angle greater than the critical angle, θ_c, where $\theta_c \geq \sin(n_1/n_2)^{-1}$, generating an evanescent electric field that decays exponentially into the lower refractive index medium. This limits the excitation region to ~100 nm into the lower refractive index aqueous solution.[72] Detectors used in FCS have typically been single channel detectors, such as photomultiplier tubes or avalanche photodiodes, which have MHz read out capabilities.[73]

Over the last 2 decades, both confocal- and TIR-FCS have yielded a wealth of

information regarding adsorption/desorption kinetics,[63,74] surface diffusion coefficients,[2,75,76] and strong adsorption behavior[77,78] at chromatographic interfaces. While FCS allows the interrogation of surface dynamics with fast temporal resolution, it lacks the ability to resolve mixed dynamic processes exhibiting similar time scale behavior. Unlike single-molecule imaging, which tracks the time evolution of molecular events individually, autocorrelation analysis combines the rates of all the dynamic processes into a continuous decay in the autocorrelation function, thus requiring the time scales of each distinct process to be well separated in order to be resolved.[73] An example of this is distinguishing autocorrelation decay arising from surface diffusion and strong adsorption at heterogeneous interfaces.[79] Long-lived strong adsorption events occurring during and FCS acquisition intended to measure the shorter-lived surface diffusion time are manifested in the autocorrelation function as a long-lived tail, which then biases the calculation of the diffusion coefficient for the moving population. Distinguishing diffusion from adsorption processes can be accomplished by investigating the dependence of the autocorrelation decay on the size of the probing region, where varying the probing region size only changes the time over which diffusional relaxation occurs, while adsorption and desorption kinetics would be independent of changes in the size of the probing region. Varying the probing region size, however, is challenging with typical confocal- or TIR-FCS instrumentation because it involves modification of the optics used for fluorescence excitation and emission collection.

In Chapter 3, we employ a recently developed technique that combines single-molecule imaging instrumentation with FCS analysis, dubbed camera- or imaging-FCS, to measure fast transport and adsorption/desorption kinetics at model (planar)

chromatographic interfaces. This technique has been developed as an alternative to traditional confocal- or TIR-FCS and used to measure solution diffusion of fluorescent quantum dots,[80] fluorescently labeled polystyrene beads, small molecule fluorescent probes in high-viscosity media and lateral diffusion of membrane-bound proteins on cell surfaces,[81] and lateral diffusion of labeled lipids in supported lipid bilayers.[82,83] The probed region comprises of the evanescent excitation region in the axial dimension and a small pixel region in the lateral dimension. Because the readout rate of the camera is directly proportional to the number of pixel rows being read, by limiting the acquisition region of the camera a small subset of pixels greater than 1 kHz, temporal resolution can be achieved. An image sequence is taken at a high frame rate, and the total intensity from each frame is summed, autocorrelated, and analyzed identically to traditional FCS. As the raw data are an image sequence, the size of the probed region is easily modified in postprocessing by selecting subregions of the image. Through this method, the dependence of the autocorrelation decay on the probing region size is easily explored on the same set of data. Furthermore, the location of the probed region can also be electronically controlled and placed in any location within the field of view of the full frame. Because the instrumentation is identical to single-molecule imaging, long-lived strong adsorption sites can be located and characterized in imaging mode and subsequently avoided during the collection of FCS diffusion data.

Using this technique, the diffusion coefficients and adsorption desorption kinetics of DiI molecules are compared at C_{18}- and C_1-modified model chromatographic interfaces. Diffusion is found to be significantly faster at the C_1 interface and beyond the temporal resolution of measurement with single-molecule imaging and tracking and

within an order-of-magnitude of free solution diffusion. Furthermore, interfacial populations are also measured using the magnitude of the fluctuations and Poisson statistics that govern their deviations from equilibrium.[74] From these results, equilibrium constants for partition between solution and the model chromatographic interfaces are calculated and free energies for adsorption are compared for both the C_{18} and C_1 surfaces.

1.7 Fluorescence Correlation Spectroscopy Study of Molecular Transport within Reversed-phase Chromatographic Particles Compared to Planar Model Surfaces

Spectroscopic techniques have provided a wealth of information regarding the dynamics at reversed-phase chromatographic interfaces as well as direct evidence of the heterogeneity of transport and adsorption behavior at these surfaces. However, spectroscopic studies of chromatographic interfaces have generally been conducted at planar analogs of porous silica particles.[2,30,32,63,74–76] These planar analogs generally consist of fused-silica or glass substrates that have been chemically modified with an alkyl ligand to resemble the interior surface of modified porous silica gel particles used in reversed-phase chromatography. While the interfacial chemistry on the planar fused-silica or glass substrates may represent an adequate analog of the interfacial chemistry reversed-phase media, planar substrates exhibit a much simpler transport geometry to that occurring with porous silica particles. Specifically, the surface area to volume ratio within a porous particle is on the order of 100 times larger than in planar models probed in a TIRF geometry, which would influence the relative populations of surface-associated versus solution-phase molecules. Furthermore, the intraparticle surface is not flat, but a porous network extending in three dimensions as opposed to strictly two dimensions on

planar models (Figure 1.6). These differences in transport geometry have potential to influence the transport behavior of molecules between porous chromatographic media and planar models, making comparison of transport parameters measured at planar models more difficult. Work on more complex silica structures, such as porous sol-gel silica thin films, has shed some light on the effect that structural heterogeneities in porous structures have on local transport behavior.[51] However, thin silica sol-gel films still differ from porous silica particles used in chromatographic media in both their pore structure and surface chemistry due to the hydrothermal treatment undergone by chromatographic media during its synthesis.[84] Recently, spectroscopic interrogation of actual reversed-phase chromatographic particles has been accomplished using Raman spectroscopy,[85–87] FCS,[78,88] and single-molecule imaging.[41] Despite the existence spectroscopic studies of both planar models and within actual chromatographic particles, few comparisons have been made between these two systems.[33]

In Chapter 4, we employ imaging-FCS to compare transport rates and surface concentrations measured at model planar chromatographic interfaces with those in actual reversed-phase chromatographic porous silica particles. The apparent diffusion coefficients within the particles are found to be much slower than those measured at planar chromatographic interfaces. Furthermore, the measured numbers of probe molecules within the particles are more than two orders-of-magnitude greater than on planar interfaces with the same field of view. These large discrepancies between measured parameters are due to the large difference in the probed surface area between the two systems. In the case of planar chromatographic interfaces, the probed surface area is straightforward and can be calculated from the dimensions of the probed region

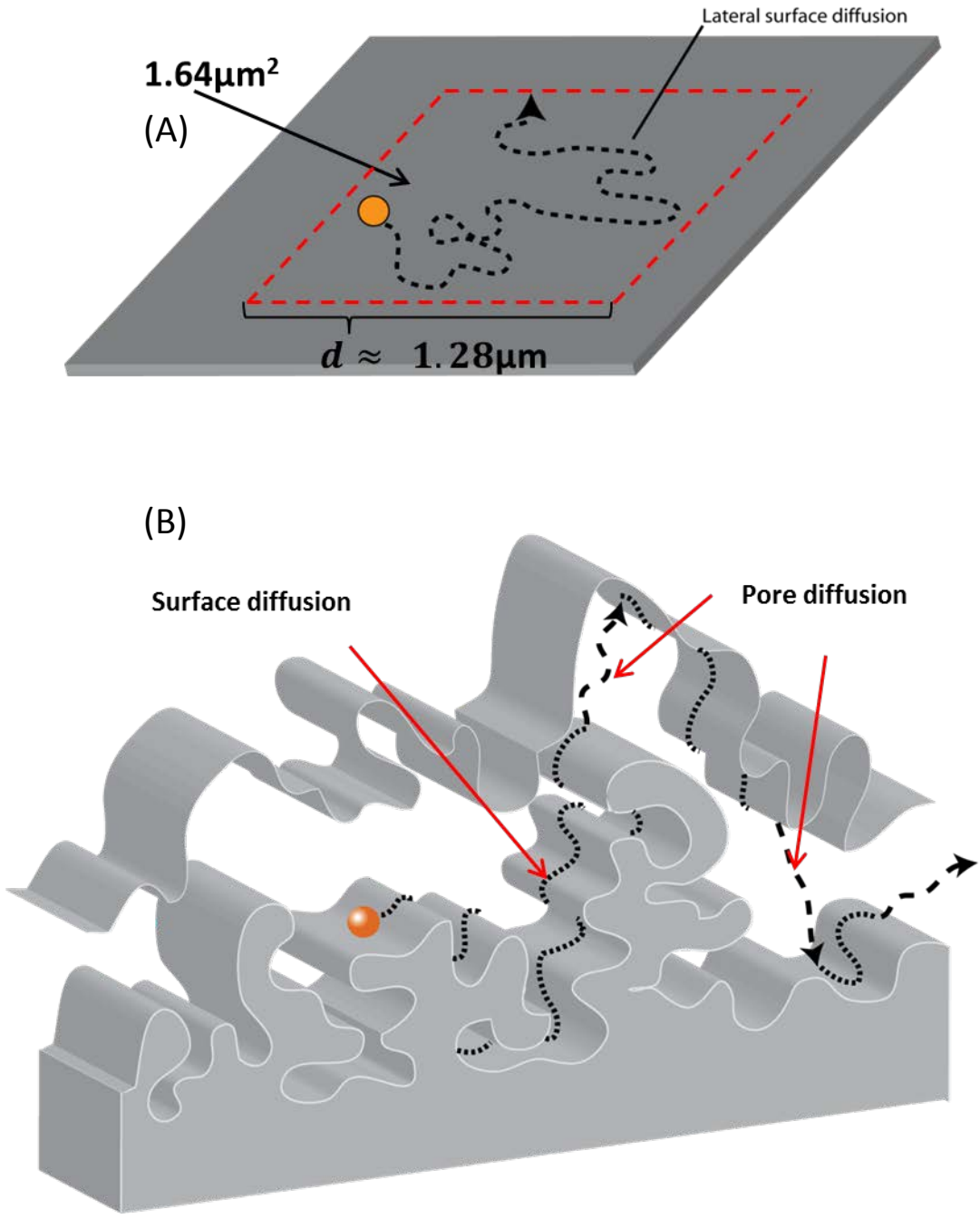

Figure 1.6. Illustration of surface diffusion over planar surface in two dimensions (A) versus surface diffusion within a porous particle over a tortuous surface in three dimensions (B). This three-dimensional surface diffusion is projected onto a 2-D detector, resulting in a loss of depth information.

selected on the CCD camera and the magnification of the image. In contrast, the probed surface area within the particle is much larger than its projected area onto the camera due to the tortuous three-dimensional porous structure. The probed surface area can be calculated from the average particle density (including porous volume), the specific surface area from BET analysis, and the volume of the probed region. When the difference in the probed surface is taken into account, it is found that measured diffusion coefficients and molecule surface densities at planar model chromatographic interfaces are in much closer agreement to those measured within actual chromatographic media. This finding suggests that planar reversed-phase modified glass surfaces are indeed reasonable models for actual chromatographic media, with the caveat that measured parameters must be scaled appropriately by the particle geometry for comparison.[79]

1.8 References

(1) Clark, A. *The Theory of Adsorption and Catalysis*; Academic Press: New York, 1970.

(2) Wirth, M. J.; Swinton, D. J.; Ludes, M. D. *J. Phys. Chem. B* **2003**, *107*, 6258.

(3) Washe, A. P.; Macho, S.; Crespo, G. n. A.; Rius, F. X. *Anal. Chem.* **2010**, *82*, 8106.

(4) Hashimoto, F.; Tsukahara, S.; Watarai, H. *Langmuir* **2003**, *19*, 4197.

(5) Donsmark, J.; Jorgensen, L.; Mollmann, S.; Frokjaer, S.; Rischel, C. *Pharm. Res.* **2006**, *23*, 148.

(6) Axelrod, D. *J. Cell Biol.* **1981**, *89*, 141.

(7) Bircumshaw, L. L.; Riddiford, A. C. *Q. Rev., Chem. Soc.* **1952**, *6*, 157.

(8) Butt, H.-J. G., Karlheinz; Kappl, M. *Physics and Chemistry of Interfaces*; Wiley-VCH: Weinheim, Germany, 2003.

(9) Wang, D.; Gou, S.-Y.; Axelrod, D. *Biophys. Chem.* **1992**, *43*, 117.

(10) Unger, K. K. *Porous Silica: Its Properties and Use as Support in Column Liquid Chromatography*; Elsevier Science: Amsterdam, 1979.

(11) Iler, R. K. *The Chemistry of Silica: Solubility, Polymerization, Colloid and Surface Properties and Biochemistry of Silica*; Wiley: New York, 1979.

(12) Glinka, C. J.; Sander, L. C.; Wise, S. A.; Hunnicutt, M. L.; Lochmuller, C. H. *Anal. Chem.* **1985**, *57*, 2079.

(13) Longman, G. W.; Wignall, G. D.; Hemming, M.; Dawkins, J. V. *Colloid Polym. Sci.* **1974**, *252*, 298.

(14) Ruthven, D. M. *Principles of Adsorption and Adsorption Processes*; Wiley: New York, NY, 1984.

(15) Renard, J.; Vidal-Madjar, C.; Lapresle, C. *J. Colloid Interface Sci.* **1995**, *174*, 61.

(16) Vidal-Madjar, C.; Jaulmes, A.; Renard, J.; Peter, D.; Lafaye, P. *Chromatographia* **1997**, *45*, 18.

(17) Gritti, F.; Piatkowski, W.; Guiochon, G. *J. Chromatogr. A* **2002**, *978*, 81.

(18) Seidel-Morgenstern, A.; Jacobson, S. C.; Guiochon, G. *J. Chromatogr. A* **1993**, *637*, 19.

(19) Guiochon, G.; Golshan-Shirazi, S.; Katti, A. M. *Fundamentals of Preparative and Nonlinear Chromatograph*; Academic Press: Boston, 1994.

(20) Miyabe, K.; Guiochon, G. *J. Chromatogr. A* **2000**, *890*, 211.

(21) van Deemter, J. J.; Zuiderweg, F. J.; Klinkenberg, A. *Chem. Eng. Sci.* **1956**, *5*, 271.

(22) Giddings, J. C. *Dynamics of Chromatography*; Marcel Dekker: New York, 1965.

(23) Giddings, J. C. *Unified Separation Science*; Wiley: New York, 1991.

(24) Miyabe, K.; Guiochon, G. *J. Phys. Chem. B* **1999**, *103*, 11086.

(25) Miyabe, K.; Guiochon, G. *J. Chromatogr. A* **2002**, *961*, 23.

(26) Gritti, F.; Guiochon, G. *Anal. Chem.* **2006**, *78*, 5329.

(27) Bogar, R. G.; Thomas, J. C.; Callis, J. B. *Anal. Chem.* **1984**, *56*, 1080.

(28) Staahlberg, J.; Almgren, M.; Alsins, J. *Anal. Chem.* **1988**, *60*, 2487.

(29) Zulli, S. L.; Kovaleski, J. M.; Zhu, X. R.; Harris, J. M.; Wirth, M. J. *Anal. Chem.* **1994**, *66*, 1708.

(30) Hansen, R. L.; Harris, J. M. *Anal. Chem.* **1995**, *67*, 492.

(31) Hansen, R. L.; Harris, J. M. *Anal. Chem.* **1996**, *68*, 2879.

(32) Wirth, M. J.; Ludes, M. D.; Swinton, D. J. *Anal. Chem.* **1999**, *71*, 3911.

(33) Ludes, M. D.; Anthony, S. R.; Wirth, M. J. *Anal. Chem.* **2003**, *75*, 3073.

(34) Wirth, M. J.; Legg, M. A. *Annu. Rev. Phys. Chem.* **2007**, *58*, 489.

(35) Xu, X.-H.; Yeung, E. S. 1997; Vol. 275, p 1106.

(36) Bard, A. J.; Fan, F.-R. F. *Acc. Chem. Res.* **1996**, *29*, 572.

(37) Ambrose, W. P.; Basché, T.; Moerner, W. E. *J. Chem. Phys.* **1991**, *95*, 7150.

(38) Fox, C. B.; Wayment, J. R.; Myers, G. A.; Endicott, S. K.; Harris, J. M. *Anal. Chem.* **2009**, *81*, 5130.

(39) Betzig, E.; Patterson, G. H.; Sougrat, R.; Lindwasser, O. W.; Olenych, S.; Bonifacino, J. S.; Davidson, M. W.; Lippincott-Schwartz, J.; Hess, H. F. *Science* **2006**, *313*, 1642.

(40) Stranahan, S. M.; Willets, K. A. *Nano Lett.* **2010**, *10*, 3777.

(41) Cooper, J. T.; Peterson, E. M.; Harris, J. M. *Anal. Chem.* **2013**, *85*, 9363.

(42) Michael, J. R.; Mark, B.; Xiaowei, Z. *Nat. Methods* **2006**, *3*, 793.

(43) Hess, S. T.; Girirajan, T. P. K.; Mason, M. D. *Biophys. J.* **2006**, *91*, 4258.

(44) Thompson, R. E.; Larson, D. R.; Webb, W. W. *Biophys. J.* **2002**, *82*, 2775.

(45) Peterson, E. M.; Harris, J. M. *Anal. Chem.* **2010**, *82*, 189.

(46) Ghosh, R. N.; Webb, W. W. *Biophys. J.* **1994**, *66*, 1301.

(47) Saxton, M. J.; Jacobson, K. *Annu. Rev. Biophys. Biomol. Struct.* **1997**, *26*, 373.

(48) Elliott, L. C. C.; Barhoum, M.; Harris, J. M.; Bohn, P. W. *Phys. Chem. Chem. Phys.* **2011**, *13*, 4326.

(49) Elliott, L. C. C.; Barhoum, M.; Harris, J. M.; Bohn, P. W. *Langmuir* **2011**, *27*, 11037.

(50) Honciuc, A.; Schwartz, D. K. *J. Am. Chem. Soc.* **2009**, *131*, 5973.

(51) McCain, K. S.; Harris, J. M. *Anal. Chem.* **2003**, *75*, 3616.

(52) McCain, K. S.; Hanley, D. C.; Harris, J. M. *Anal. Chem.* **2003**, *75*, 4351.

(53) Fu, Y.; Ye, F.; Sanders, W. G.; Collinson, M. M.; Higgins, D. A. *J. Phys. Chem. B* **2006**, *110*, 9164.

(54) Ye, F.; Higgins, D. A.; Collinson, M. M. *J. Phys. Chem. C* **2007**, *111*, 6772.

(55) Ye, F.; Collinson, M. M.; Higgins, D. A. *Phys. Chem. Chem. Phys.* **2009**, *11*, 66.

(56) Michalet, X.; Berglund, A. J. *Phys. Rev. E: Stat., Nonlinear, Soft Matter Phys.* **2012**, *85*, 061916.

(57) Michalet, X. *Phys. Rev. E: Stat., Nonlinear, Soft Matter Phys.* **2010**, *82*, 041914.

(58) Elson, E. L.; Magde, D. *Biopolymers* **1974**, *13*, 1.

(59) Elson, E. L.; Schlessinger, J.; Koppel, D. E.; Axelrod, D.; Webb, W. W. *Prog. Clin. Biol. Res.* **1976**, *9*, 137.

(60) Hansen, R. L.; Zhu, X. R.; Harris, J. M. *Anal. Chem.* **1998**, *70*, 1281.

(61) Magde, D.; Elson, E. L.; Webb, W. W. *Biopolymers* **1974**, *13*, 29.

(62) Thompson, N. L.; Burghardt, T. P.; Axelrod, D. *Biophys. J.* **1981**, *33*, 435.

(63) Hansen, R. L.; Harris, J. M. *Anal. Chem.* **1998**, *70*, 4247.

(64) Kask, P.; Piksarv, P.; Mets, Ü.; Pooga, M.; Lippmaa, E. *Eur. Biophys. J.* **1987**, *14*, 257.

(65) Widengren, J.; Mets, Ü.; Rigler, R. *Chem. Phys.* **1999**, *250*, 171.

(66) Thiel, E.; Drexhage, K. H. *Chem. Phys. Lett.* **1992**, *199*, 329.

(67) Widengren, J.; Rigler, R.; Mets, Ü. *J. Fluoresc.* **1994**, *4*, 255.

(68) Widengren, J.; Mets, U.; Rigler, R. *J. Phys. Chem.* **1995**, *99*, 13368.

(69) Bernasconi, C. F. *Relaxation Kinetics*; Academic Press, Inc.: New York, 1976.

(70) Rigler, R.; Pramanik, A.; Jonasson, P.; Kratz, G.; Jansson, O. T.; Nygren, P.-Å.; Ståhl, S.; Ekberg, K.; Johansson, B.-L.; Uhlén, S.; Uhlén, M.; Jörnvall, H.; Wahren, J. *Proc. Natl. Acad. Sci. U. S. A.* **1999**, *96*, 13318.

(71) Wilson, T. *Confocal microscopy*; Academic Press: London 1990.

(72) Axelrod, D. In *Methods in Cell Biology*; Taylor, D. L., Yu-Li, W., Eds.; Academic Press: 1989; Vol. 30, p 245.

(73) Schwille, P.; Haustein, E. In *An Introduction to its Concepts and Applications* Biophysical Society: Bethesda, 2004.

(74) Hansen, R. L.; Harris, J. M. *Anal. Chem.* **1998**, *70*, 2565.

(75) Swinton, D. J.; Wirth, M. J. *Anal. Chem.* **2000**, *72*, 3725.

(76) Wirth, M. J.; Swinton, D. J. *Anal. Chem.* **1998**, *70*, 5264.

(77) Ludes, M. D.; Wirth, M. J. *Anal. Chem.* **2001**, *74*, 386.

(78) Zhong, Z.; Lowry, M.; Wang, G.; Geng, L. *Anal. Chem.* **2005**, *77*, 2303.

(79) Cooper, J. T.; Harris, J. M. *Anal. Chem.* **2014**, *86*, 7618.

(80) Burkhardt, M.; Schwille, P. *Optics Express* **2006**, *14*, 5013.

(81) Kannan, B.; Har, J. Y.; Liu, P.; Maruyama, I.; Ding, J. L.; Wohland, T. *Anal. Chem.* **2006**, *78*, 3444.

(82) Guo, L.; Har, J. Y.; Sankaran, J.; Hong, Y.; Kannan, B.; Wohland, T. *Chem. Phys. Chem.* **2008**, *9*, 721.

(83) Kannan, B.; Guo, L.; Sudhaharan, T.; Ahmed, S.; Maruyama, I.; Wohland, T. *Anal. Chem.* **2007**, *79*, 4463.

(84) Brinker, C. J.; Scherer, G. W. *Sol-Gel Science: The Physics and Chemistry of Sol-Gel Processing*; Academic Press: Boston, 1990.

(85) Gasser-Ramirez, J. L.; Harris, J. M. *Anal. Chem.* **2009**, *81*, 2869.

(86) Gasser-Ramirez, J. L.; Harris, J. M. *Anal. Chem.* **2009**, *81*, 7632.

(87) Gasser-Ramirez, J. L.; Harris, J. M. *Anal. Chem.* **2010**, *82*, 5743.

(88) Zhong, Z.; Geng, M. L. *Anal. Chem.* **2007**, *79*, 6709.

CHAPTER 2

FLUORESCENCE IMAGING OF SINGLE-MOLECULE RETENTION TRAJECTORIES IN REVERSED-PHASE CHROMATOGRAPHIC PARTICLES

2.1 Introduction

Due to its high surface area, mechanical stability, and well characterized surface chemistry, mesoporous silica is used for a number of important applications including catalysis,[1] biomolecule immobilization and separations,[2–4] drug encapsulation and delivery,[5] sensing,[6,7] and chromatographic separations.[8–10] The development and optimization of porous silica for these applications depends on understanding the transport of molecules through the pore network[11] for efficient heterogeneous reactions, sensing, and separations. Separation techniques, in particular, have employed porous silica particles as stationary-phase supports for decades, exploiting their high specific surface area to maximize analyte interactions with the stationary phase, thus improving separation efficiency.[12] Development of chromatographic materials and techniques with better separation efficiency and higher resolution requires an understanding of fundamental processes that govern retention of analytes in the column and the timescales at which they occur.

The dynamics of molecular transport within porous chromatographic media have been studied previously using chromatographic techniques. Intraparticle transport has

typically been treated as contributing to resistance to mass transfer in expressions for the height equivalent of a theoretical plate.[13–15] Several techniques including frontal analysis of solute breakthrough curves and the perturbation or pulse-response method[16–18] have been pioneered by Guiochon and coworkers. These methods have been used to determine mass transfer rate coefficients in various chromatographic media, with recent attention directed toward determining the contribution of surface diffusion to transport efficiency within porous particles.[19–21] The techniques rely on careful analysis of elution profiles to infer the kinetic parameters governing the contributions of intraparticle transport to chromatographic band broadening.

Spectroscopic techniques have also been employed to investigate the dynamics of molecules at models of reversed-phase chromatographic interfaces on planar substrates. Fluorescence depolarization measurements provided information on the rapid rotational mobility of molecules at interfaces between C18 chains and water.[22] These results could be contrasted with much slower long-range surface diffusion of molecules observed by fluorescence recovery after photobleaching,[23–25] especially for uncharged aromatic molecules that likely partition into the C_{18} chains.[24,25] Fluorescence correlation spectroscopy (FCS) has been used to study adsorption/desorption kinetics from model (planar) stationary phase surfaces.[26,27] In addition, rates of surface diffusion and their dependence on the overlaying solvent composition could be measured,[28,29] where topological defects were correlated with long-lived desorption events observed as persistent single-molecule residence times within a tightly-focused excitation spot.[29,30]

Tracking motions of single fluorescent molecules over larger areas can provide important insight into the heterogeneity of their diffusional trajectories and its

relationship to the chemistry of the underlying surface. This concept was demonstrated for multimode diffusion of fluorescently labeled alkanoic acids of various chain lengths at a methylated silica-water interface[31] and of amphiphilic dyes interacting with stimulus-responsive, thin films of poly(N-isopropylacrylamide) below and above their critical transition temperature.[32,33] Fluorescence correlation spectroscopy and single-molecule imaging microscopy have also been adapted to thin silica sol-gel films to investigate the influence of pore structure and chemical interactions on molecular transport within the porous film.[34–38] These measurements reveal spatial heterogeneities in thin-film structure that lead to localized variations in molecular diffusivities, where molecular motions depend on the chemistry of the fluorescent probe molecule, the ordering of the film during deposition, and treatment of the sol-gel pore surface.

Despite valuable information about molecular transport in thin silica sol-gel films that FCS and single-molecule tracking can provide, these films[39] do not share the same pore structure or surface chemistry with silica-gel particles prepared as chromatographic stationary-phase supports. Chromatographic silica gels are generally sintered at high temperature to collapse micropores and then subjected to hydrothermal treatment[8,9] to increase their average pore diameter, tighten the pore-size distribution, and hydrolyze surface siloxane bonds.[8] The resulting hydrophilic, open-pore silica particles can then be surface-modified with n-alkylsilane or related ligands to produce chromatographic packing materials capable of efficient reversed-phase chromatographic separations.[8,10,12] Spectroscopic probing of the interior of chromatographic silica particles would appear to be challenging, where light scattering from refractive index boundaries of the pores could degrade spatial resolution and efficiency of collecting emission. The interior of individual

chromatographic silica particles has, however, been successfully imaged with confocal fluorescence microscopy (including FCS measurements)[40,41] and Raman microscopy,[42–44] where the spatial resolution is not significantly degraded from the diffraction limit, even when collecting radiation from the center of a 10-μm reversed-phase silica particle.[42] This is not surprising, however, because the 10-nm diameter pores are much smaller than ($<1/50^{th}$) the wavelength of the excitation light, and the refractive index difference between silica pore walls and mobile phase within pores is also small, <10%. As a result, fluorescence or Raman scattering can be imaged with high fidelity within the interior of authentic chromatographic particles, and interference from molecules in solution surrounding the particle is minimized due to the small depth of field of a high numerical-aperture microscope objective.

In the present work, single-molecule fluorescence microscopy is adapted to imaging individual molecules visiting reversed-phase chromatographic silica particles to characterize intraparticle molecular transport as single-molecule observations. In a previous and pioneering FCS approach to this experiment,[40] the time dependence of fluorescence intensity from molecules traversing a small local spot within the particle defined by confocal optics was characterized by time-sequence and autocorrelation analysis. Here, we image individual molecules in movies and follow their motion in space over time to determine their diffusional behavior within the particle. By tracking molecules from when they first appear to when they leave the sampled depth of field within the particle, intraparticle residence times of molecules can be determined within the sampled volume and plotted as residence-time histograms of hundreds of molecular events. The intraparticle diffusion coefficient is determined from mean squared

displacements of molecules versus time; this measured result is then used as a fixed parameter in a random-walk simulation, which predicts the observed residence-time histograms. Spatial distributions (locations) of molecules within the silica particle are also determined, and the results compared to a random-walk simulation within a spherical geometry truncated by the optical depth of field. A small fraction of stuck-molecule events are also observed and characterized; similar results have previously been reported in FCS measurements of planar model interfaces[29–30] and in authentic C_{18} chromatographic particles.[40] With the exception of these events, which significantly influence residence times, the observed trajectories of moving molecules within the particle are consistent with diffusion in a continuous three-dimensional pore network throughout the particle.

2.2 Experimental Section

2.2.1 Chemicals and materials

Zorbax ODS chromatographic silica (3-μm diameter) was acquired from Agilent Technologies (Santa Clara, CA). The particles were characterized via nitrogen BET (see Supporting Information) by Porous Materials, Inc. (Ithaca, NY). Octadecylrhodamine B (R18) fluorescent dye was purchased from Invitrogen (Carlsbad, CA). Serial dilutions of R18 were made into Omnisolv spectroscopy grade methanol from EMD chemicals (Darmstadt, Germany). Custom flow cells were constructed using luer-lock adapters and tubing from Value Plastics Inc. (Fort Collins, CO) and 22x22 mm No. 1.5 glass coverslips from VWR International (Radnor, PA). All aqueous solutions were prepared using 18 MΩ-cm water, purified with a Barnstead NANOpure II system (Boston, MA). ACS grade sodium chloride (Mallinckrodt) was included as a supporting electrolyte at

10-mM in all solutions.

2.2.2 Preparation of chromatographic silica particles for imaging

Approximately 20 mg of Zorbax 3-μm ODS silica was suspended in 10 mL of methanol. A 10–20 μL aliquot of this suspension was added to 10 mL of a 30:70 by volume methanol:water solution and left overnight to equilibrate the interior pore volume. Approximately 1 mL of the methanol/water silica suspension was injected to a custom-built flow cell consisting of a C_{18}-silane modified glass coverslip, gasket, glass top plate and ports for solution flow and drain. The coverslips were functionalized with C_{18}-silane by a self-assembly approach.[45,46] Briefly, glass coverslips were immersed in a solution of 1-mM octadecyltrichlorosilane (Sigma Aldrich, St. Louis, MO) in dry n-heptane, and the silane was allowed to physisorb to the glass surfaces for 24 h. The coverslips were then rinsed with n-heptane and baked at 120˚ for 1 h to cross-link the monolayer and bind it to the surface. Hydrophobic interactions between the ODS particles and the C_{18}-modified glass coverslip fix the particles to the surface and allow for solution flow without detaching the particles from the surface. During fluorescence microscopy measurements, a 5 pM solution of R18 in a 30% methanol/water mixture was flowed continuously through the cell at 0.25 mL/min with a syringe pump (Harvard Apparatus PHD 2000).

2.2.3 Single-molecule fluorescence microscopy

Silica particles were imaged in an epi-illumination geometry using an Eclipse TE200 inverted microscope (Nikon Corporation), equipped with a 100x 1.49 NA Apo-TIRF oil immersion objective, Lexel argon-ion laser (514.5nm, 11mW into the

objective), and Andor iXon^{EM}+ 897 EMCCD camera (see Supporting Information). Image sequences of single R18 molecules diffusing inside the porous silica particles were captured continuously for 4000 frames at 30-ms integration times (33.3 fps) and ~100x electron multiplication gain. Single-molecule movies were analyzed using custom analysis algorithms written in the Matlab (Mathworks) numerical computing environment. The center-of-intensity-mass coordinates for each identified molecular spot were recorded in each frame for tracking molecular locations in two dimensions. The tracking algorithm establishes an upper bound to displacement to avoid the trajectory of one molecule being transferred to another and also bridges single-frame photoblinking events (see Supporting Information for algorithm details).

2.3 Results and Discussion

2.3.1 Imaging and tracking individual R18 molecules within RPLC porous silica particles

The capability of imaging individual octadecylrhodamine B (R18) molecules *within* a RPLC silica particle is illustrated in Figure 2.1. With the focus at the bottom of the particle on the C_{18}-coated coverslip, individual R18 molecules adsorbed to the hydrophobic coverslip surface are detected in sharp focus; moving the focus up 1.5 μm into the center of the 3-μm particle causes those molecules to disappear because of the short depth of field (~0.6 μm) of the high NA objective, while a molecule within the C18-silica particle comes into sharp focus. The threshold intensity for detecting single molecules was established by measuring background intensity of a blank particle with no R18 molecules. The mean and standard deviation of the background were determined, and the intensity threshold was set at $\mu_{bkg}+2.5\sigma_{bkg}$, corresponding to a ~2% probability of

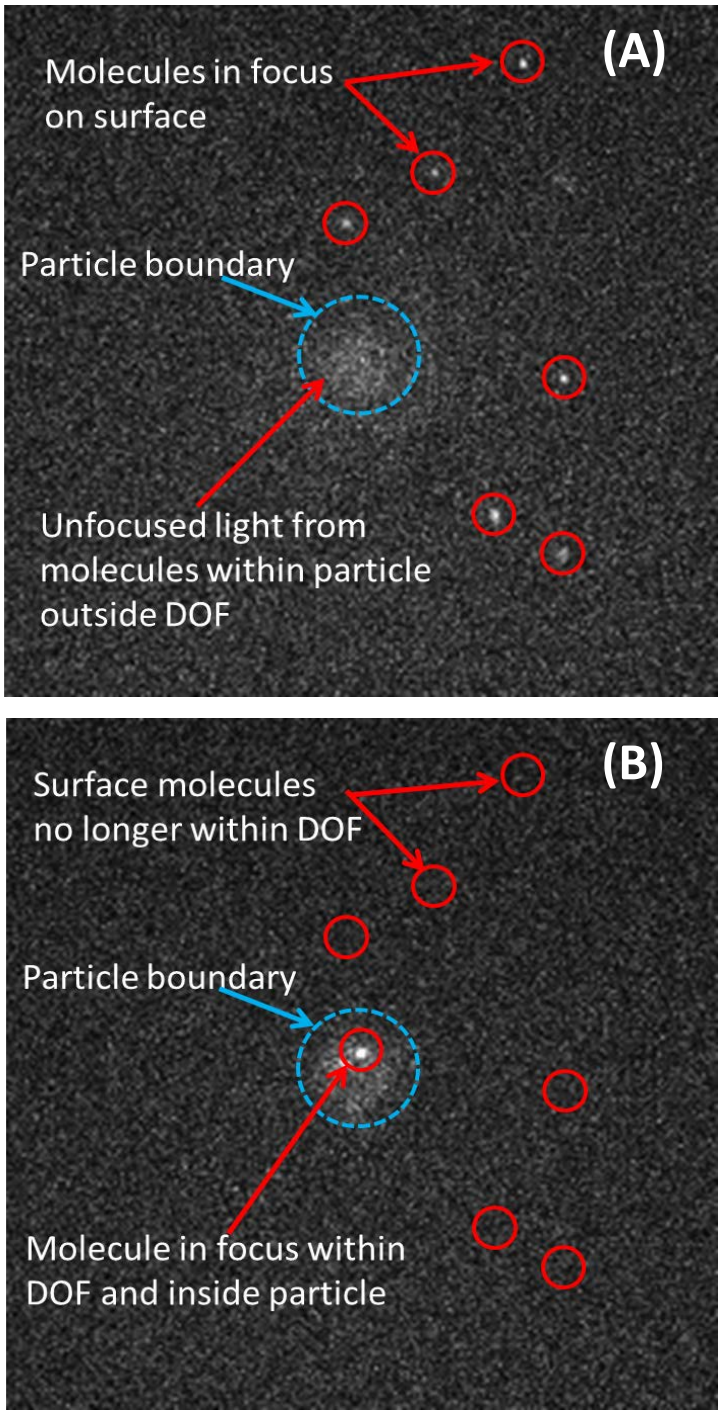

Figure 2.1. Fluorescence image (30-ms exposure) with (A) the focal plane located at the C_{18}-coated coverslip and (B) the focal plane translated 1.5 μm up to the center of the particle.

a background pixel intensity being higher than the threshold (see Supporting Information), as is pictured in Figure 2.2a. For a molecule to be identified, however, we apply spatial criteria to the diffraction-limited fluorescent spot,[47] requiring three adjacent pixels to be above threshold. Including spatial information lowers the false positive probability within the particle to $\alpha = 0.015$ molecules per frame based on combinatorial statistics.[47] The false-negative probability was determined by fitting a histogram of the third most intense pixel intensity for all detected molecular spots to an exponentially modified Gaussian function and integrating from zero to the intensity threshold, as is shown in Figure 2.2b; the false negative probability thus estimated is $\beta = 2.4\%$.

Movies of R18 molecules diffusing within RPLC porous silica particles were acquired at 30 fps. The motions of molecules in the optical depth of field within the particle were analyzed by identifying the molecular spots as above and then tracking their locations in each frame. To construct a trajectory, the root-mean-squared displacement of spots between frames i and j, $r_{ij} = \sqrt{(x_j - x_i)^2 + (y_j - y_i)^2}$, were determined and compared to a maximum displacement, r_{max}, that includes 99% of the radial probability distribution for the diffusion of moving molecules in the particle (see Supporting Information). This maximum displacement (r_{max}) criterion limits the probability of two distant molecules being logged as a displacement of the same molecule, where displacements smaller than the criterion are stitched together to form a molecular trajectory. A sample of several frames with a molecule being tracked is shown in Figure 2.3.

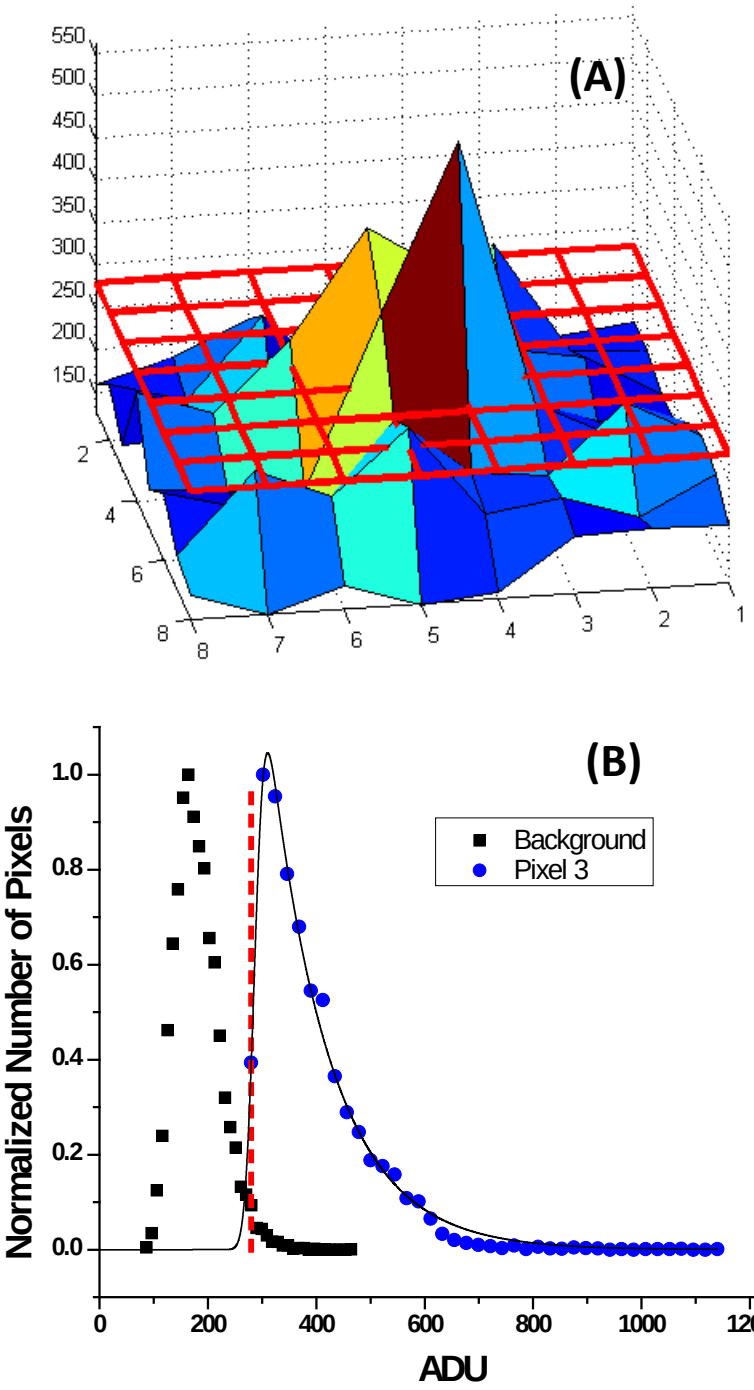

Figure 2.2. Intensity threshold analysis for single-molecule identification. (A) Intensity plot of an 8x8 pixel region containing a located molecule surrounded by background noise. The red mesh is located at the threshold intensity value. Intensities are in detector analog-to-digital units. (B) Histograms of background pixel intensities (black squares) and 3rd most intense pixel for identified molecules (blue circles). Threshold intensity is shown as red dashed line.

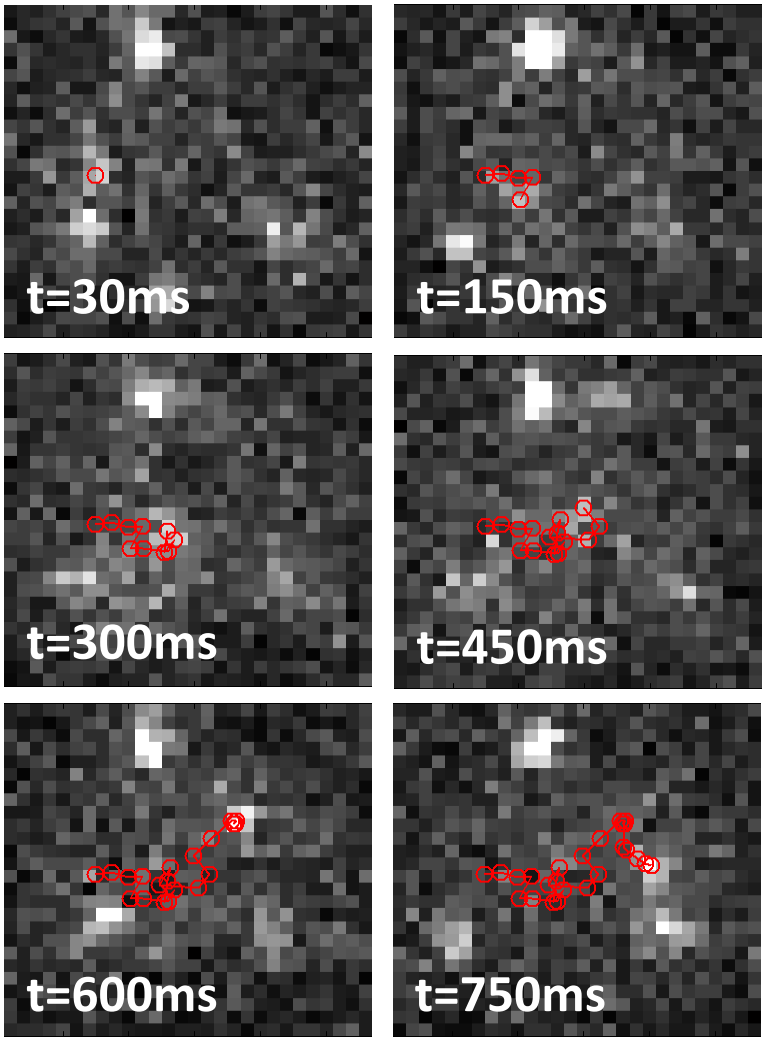

Figure 2.3. Example frames for tracking an R18 molecule within a C_{18} particle. Six frames (30 ms per frame) of a 25-frame trajectory are shown. Red circles indicate previously identified locations throughout the trajectory, ending at the current location of the molecule at the indicated time.

2.3.2 Characterizing intraparticle molecular transport.

It is evident from the movies of R18 motion within RPLC particles that the transport is not homogenous. There are times when molecules diffuse continuously, and also some points in the trajectories where motion is arrested and the molecules remain stuck for a period of time. A possible explanation of this behavior would be that free diffusion is in the mobile phase while arrested motion occurs on the C_{18} surface. This view is, however, incorrect because the R18 retention on the C_{18} stationary phase is set very high in this experiment so that molecules spend sufficient time within a particle to track their motions and measure their residence times. We can estimate the intraparticle capacity factor from the average number of R18 molecules detected within the 0.6-μm depth of field in the particle, $N_T=N_S + N_m = 2.02$, compared with the number in the intraparticle mobile phase, $N_m = 0.004$, estimated from the R18 concentration in mobile-phase and pore volume within the depth of field. The resulting intraparticle capacity factor, $k' = N_S/N_m \sim 490$, indicates that R18 molecules within the particle spend only 0.2% of their time in the mobile phase, so 99.8% of the transport is occurring as diffusion on the C_{18}-surface, which dominates at high retention conditions.[19–21]

Therefore, the heterogeneous intraparticle molecular transport is occurring on the C_{18} surface and reflects inhomogeneity in stationary-phase structure. Evidence of diffusional heterogeneity has been previously reported for strongly retained probe molecules on planar model reversed-phase surfaces[27,29,30] as well as within chromatographic media[40,41,48] from FCS and single-molecule fluorescence intensity trajectories. These stuck events were attributed to unmodified *active* silanols that exhibit strong adsorption either from ion exchange with deprotonated silanols[30,49,50] or structural

defects in the silica surface.[29,51,52] While the fraction of trajectories that include one or more stuck events in the present results is small (<12%, see below), the stuck event times can be quite long and can thus significantly impact the kinetics of tracked molecules. For this reason, statistical criteria, based on displacement probabilities for both moving and stationary molecules, were developed to divide the steps in the molecular trajectories into moving and stuck events.

In order to identify molecules that are moving, the fluctuations in the apparent position of stationary molecules arising from fluorescence noise must be characterized to determine when displacements exceed this position uncertainty. These *apparent* displacements of several stationary molecules were characterized, and an example histogram of step sizes is shown in Figure 2.4a. The probability density of apparent step sizes for a large ensemble approaches a Gaussian distribution based on the central limit theorem[53] and thus resembles a step-size distribution of a random walk.[54] The histogram in Figure 2.4a was fit to a radial displacement probability density of a random walk in two dimensions[35,55,56,54]

$$P(r) = \frac{1}{\pi\langle r^2\rangle} e^{\left(\frac{-r^2}{\langle r^2\rangle}\right)} 2\pi r \qquad [2.1]$$

yielding an apparent root-mean-squared displacement, $\sqrt{\langle r_{stuck}^2\rangle}$, of 0.037 ± 0.008 μm, which is the uncertainty in localizing a stationary molecule in an image. A critical displacement value, r_{crit}, = 0.064μm was determined by integrating the radial distribution so that the total probability from $r = 0$ to r_{crit} is 95%. Because this distribution describes the step-size probability for *stationary* molecules, $r > r_{crit} =$ 0.064 μm (dashed-vertical lines in Figure 2.4) provides 95% confidence for identifying

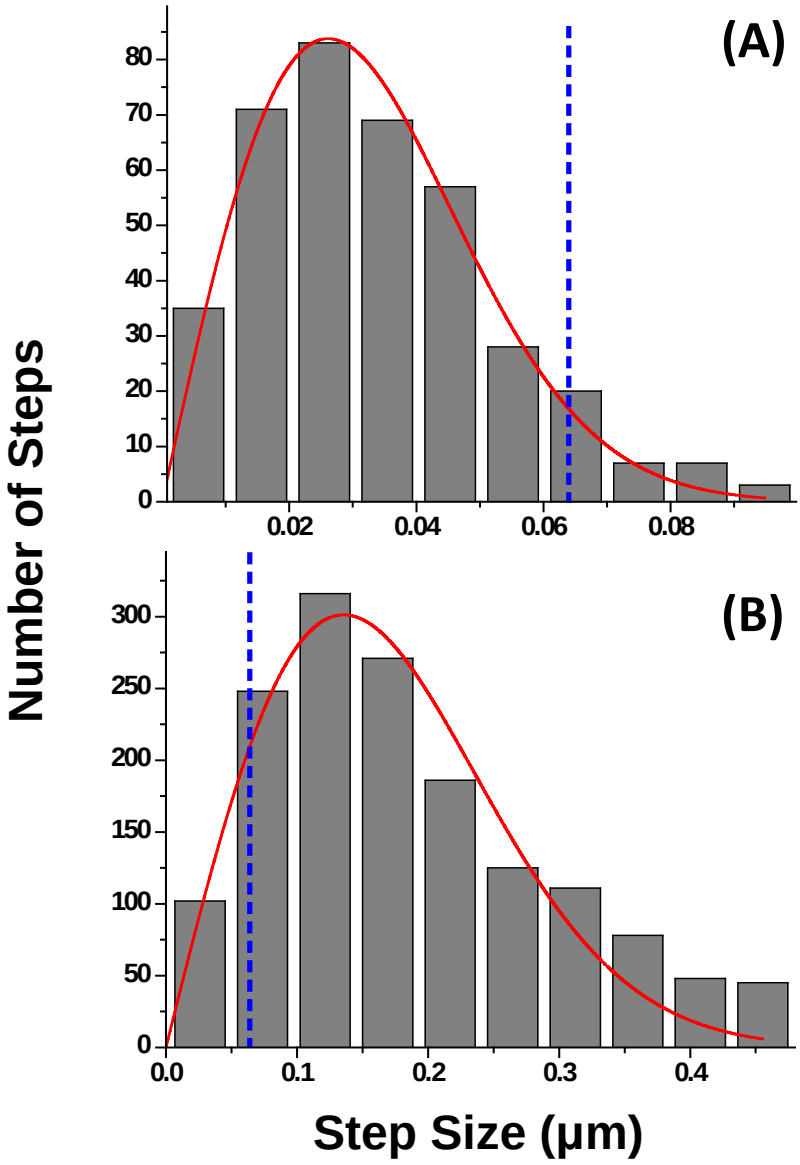

Figure 2.4. Histograms of apparent step sizes and real step sizes of stationary (A) and moving (B) molecules, respectively. The solid curve is the fit to a 2-D random walk displacement probability density (Equation 1.1). The vertical dashed line indicates the critical displacement of 0.064 μm.

displacements of molecules that are moving. Stationary molecules only have a 5% chance of exhibiting an apparent displacement greater than 0.064 μm, thus the false-positive probability that a molecule identified as moving is actually stationary is 5%.

Having established a criterion for identifying moving molecules, the step-size distribution of *moving* molecules could be determined by applying this criterion to molecular trajectories and considering only displacements larger than r_{crit}. The resulting histogram of the single-frame displacements for moving molecules (Figure 2.4b) fits a radial probability distribution in two dimensions (Equation 2.1), where the root-mean-square displacement between frames of $\langle r_{mov}^2 \rangle^{1/2}$ = 0.19 ± 0.01 μm. To further test whether the moving molecule population diffuses according to a random walk within the particles, the evolution of the mean-squared displacement can be measured as a function of time. According to the Einstein equation,[54] the mean-squared displacement of a random walk in two dimensions increases linearly with time,

$$\langle r_{mov}^2 \rangle = 4D_i t \qquad [2.2]$$

where D_i is the intraparticle diffusion coefficient and t is the time interval between observations. A plot of the mean-squared displacement versus time for moving molecules is shown in Figure 2.5; the data are linear as predicted by Equation 2.2, and the intraparticle diffusion coefficient is D_i = 3.1 (± 0.1) x 10^{-9} cm^2/s. This slope predicts a root-mean-square displacement between 30-ms frames of $\langle r_{mov}^2 \rangle^{1/2}$ = 0.192 ± 0.003 μm, which is indistinguishable from the value determined from the distribution of single-frame displacements (Figure 2.4b). The square root of the small intercept of Figure 2.5, $\langle r_{mov}^2 \rangle^{1/2}$ = 0.07 (± .05) μm, is within error bounds of the localization error of stationary

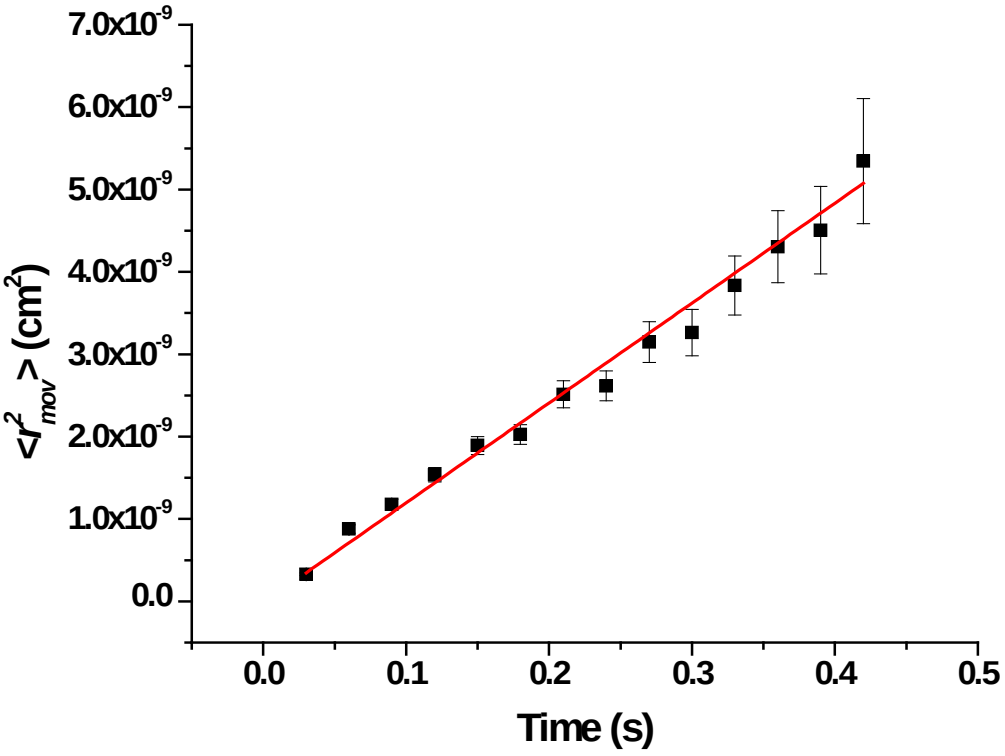

Figure 2.5. Mean squared displacement versus time for moving molecules (black squares) and fit to Equation 1.2 (red line).

molecules (see above);[57] this intercept would contribute to apparent motion of molecules that do not move very far at short time delays.

In order to identify stationary molecules with confidence, a statistical criterion is based on the step-size distribution of *moving molecules*. The distribution in Figure 2.4b for moving molecules indicates that displacements smaller than r_{crit} = 0.064μm represent only 10% of the area, thus one can be 90% confident identifying them as stationary. To increase the confidence in identifying a molecule as stuck, without compromising the 95% confidence for identifying moving molecules, an additional requirement was added that the molecule exhibit two successive steps of less than 0.064 μm to be considered stationary (stuck). For randomly moving molecules, this lowers the false positive probability to $(0.1)^2$ or 1% and thus raises the confidence for identifying stuck molecules to 99%.

2.3.3 Characterizing strong-adsorption events

Using these statistical criteria, molecular displacement trajectories were divided into time intervals during which molecules were identified as moving or stationary (stuck events). From the analysis of 1489 trajectories, 345 stationary-molecule events were identified, whose durations varied over a wide range from 60 ms to 4.5 s, with an average of 0.21 s; a histogram of stuck times, excluding one 'site' that exhibited anomalously long residence times (see below), is plotted in Figure 2.6. The distribution fits a biexponential with lifetimes of 0.054 ± 0.003 and 0.27 ± 0.05 s, indicative of a distribution of strong-site absorption energies. Unlike moving molecules, which represent free diffusion on the stationary-phase surface[27,40] (see above), the stuck events represent R18 molecules encountering strong adsorption sites on the stationary phase that

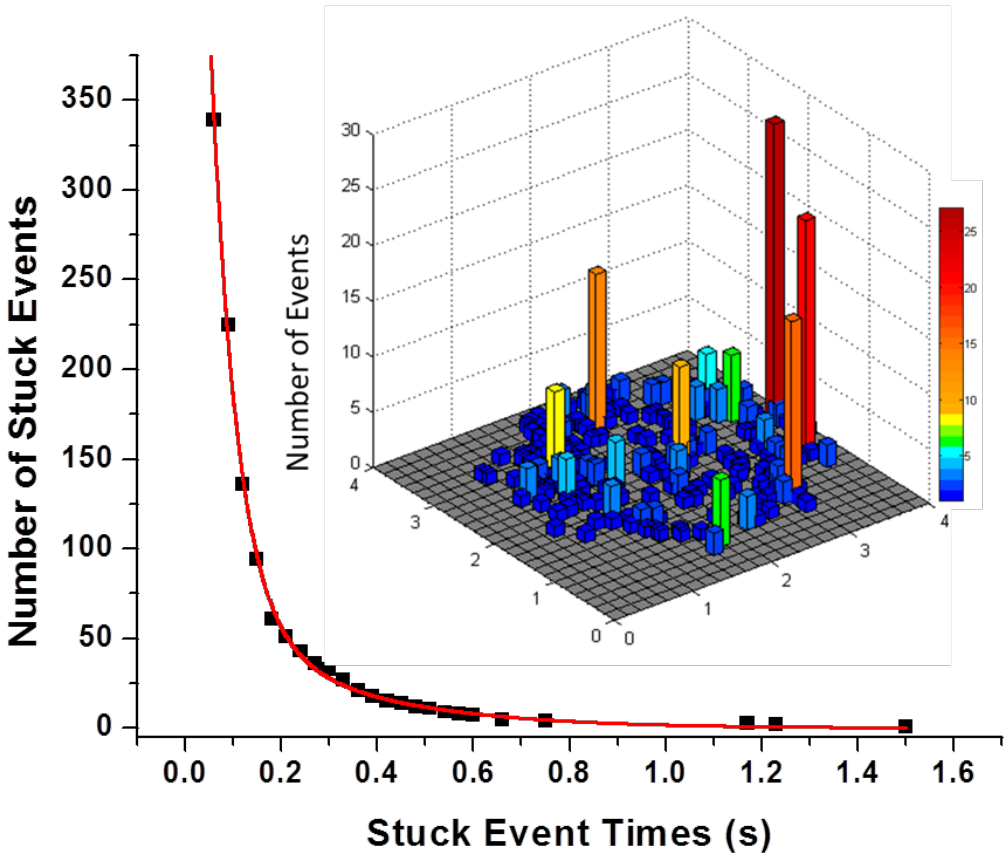

Figure 2.6. Cumulative histogram of molecular stuck times, fit to a biexponential function indicating characteristic adsorption lifetimes of 80 ms and 0.83 s. Inset is a 2-D map of stuck events at resolved sites (x, y axes are in μm); anomalous site with 2.2 ± 0.6 s average lifetime is noted with an arrow and not included in the event-time histogram.

arrest their motion.[30,40] These sites can contribute to peak tailing in chromatographic retention that degrades resolution.[14,58,59]

Because strong adsorption sites are likely to occur at defects in the stationary phase, the spatial distribution of locations where R18 molecules strongly adsorbed was examined. Strong-adsorption sites were mapped by determining the 2-D coordinates of every molecule during a stuck event, and event locations that fall within the lateral resolution limit, r_{crit} = 0.064μm, are collected into a 2-D map of stuck-molecule *sites* (Figure 2.6 inset), along with a histogram of how many sites experience a given number of events (Figure 2.7). Most of the 345 stuck events occur at 137 isolated locations that are visited only once, and the probability for multiple events initially falls off according to a Poisson probability distribution, which has been used to account for random peak overlap in chromatography,[60] molecular counting in electrophoresis,[61] and the spot capacity of single-molecule images.[47,62] For sites visited between one and five times (i = 1–5), a Poisson distribution: $P(i,\mu) = (\mu^i \mathrm{e}^{-\mu}/i!)$ with a mean $\mu = 0.45$ fits the results, suggesting a random distribution of many strong sites. The behavior of eight sites, however, visited from six to 27 times, accounts for *107 stuck events* and is clearly *anomalous*. The Poisson distribution predicts *less than 1% chance* of random overlap producing *a single site with more than five events*. One of these sites, visited six times and noted in Figure 2.6 inset, exhibited very long residence times, averaging 2.2 ± 0.6 s, well outside the lifetime distribution (Figure 2.6). The residence times of the remaining sites were analyzed in two groups based on the above Poisson analysis, those visited five times or less, compared with those visited six times or more (Figure 2.8). The stuck lifetimes of the two groups of sites were indistinguishable from results in Figure 2.6;

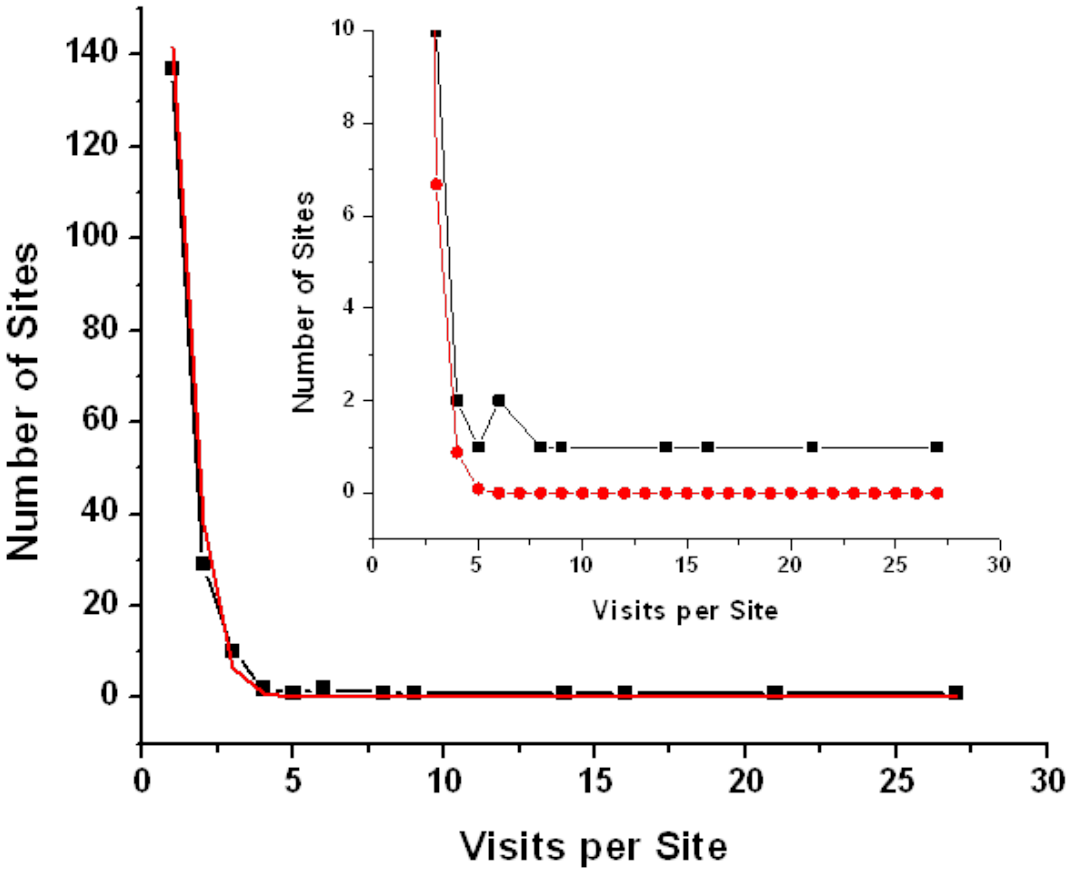

Figure 2.7. Histogram of number of strong sites versus number of molecular visits at each site. The full histogram is plotted lower-left, while the inset expands the region of 3 to 27 visits.

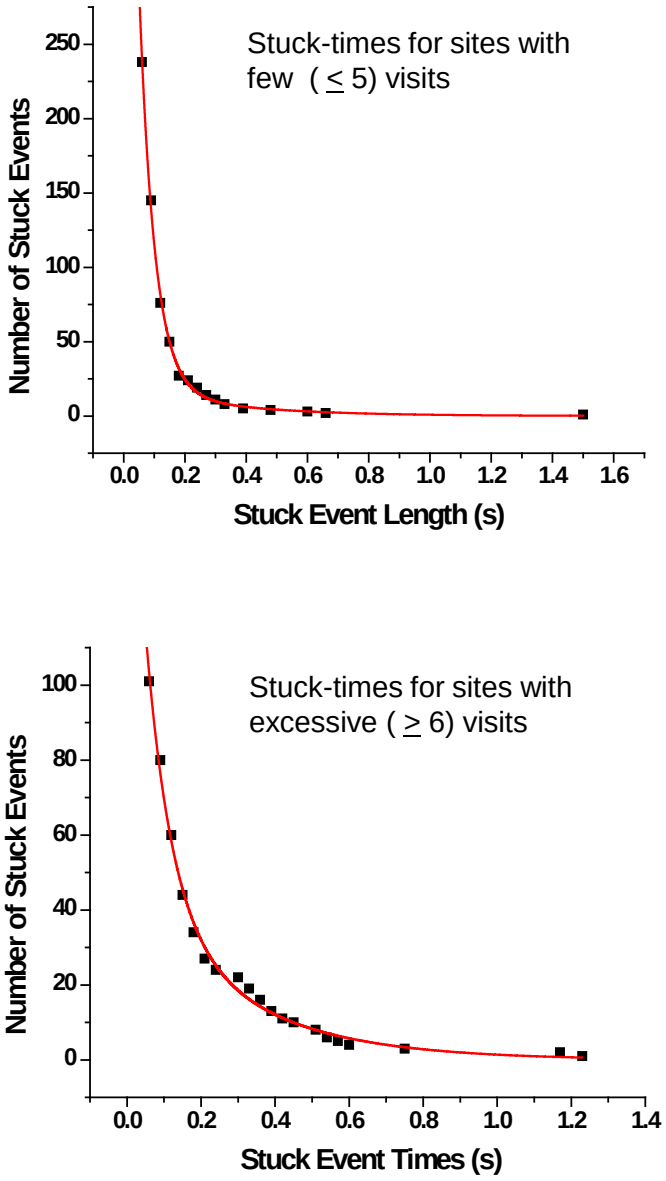

Figure 2.8. Histograms of stuck times for sites visited five or less times (top) compared to sites visited six or more times (below). The lifetimes of the biexponential fits were indistinguishable within their uncertainties from the average population (0.054 ± 0.003 and 0.27 ± 0.05 s), while the fraction of longer-lived population was different, 3% in the case of sites visited five or fewer times versus 24% for sites visited six or more times.

however, the fraction of visits that were long-lived (0.27s) was *much higher* for those sites visited often (24%) compared to only 3% long lived events at sites visited five or fewer times. Thus, there appears to be a correlation between the probability of a molecule visiting a particular site and its probability of falling into an energetically deeper trap. These long-lived visits to anomalous, deep-trap sites have a significant impact on molecular residence times, as discussed in following section.

2.3.4 Intraparticle molecular residence times and spatial distribution

Molecular residence times within a chromatographic particle represent the time that the analyte is removed from the flowing mobile phase, and the distribution of times required for transport into and out of the particle contributes to chromatographic band broadening.[13–15] The residence times of molecules within the observation depth of field in the particle were measured to determine the relationship between the intraparticle residence times, the diffusion coefficient, and stuck times of molecules. Residence times were determined from the durations of the identified molecular trajectories and were compiled into a histogram for analysis. Residence times were also classified according to whether the trajectory included a strong adsorption event. Of the 1489 analyzed molecular trajectories, only a small fraction, 172 or 12%, exhibited one or more stuck events. Figure 2.9 shows normalized residence-times histograms for all of recorded trajectories along with filtered results from trajectories that contain strong-adsorption events and those that do not. From the results, it is evident that strong-adsorption events significantly impact intraparticle residence times. Trajectories exhibiting one or more stuck events have average residence times, τ_{res}=0.84 ±0.12 s, more than a factor of 10 greater than trajectories lacking any strong adsorption, τ_{res}=0.081 ±0.003 s. While

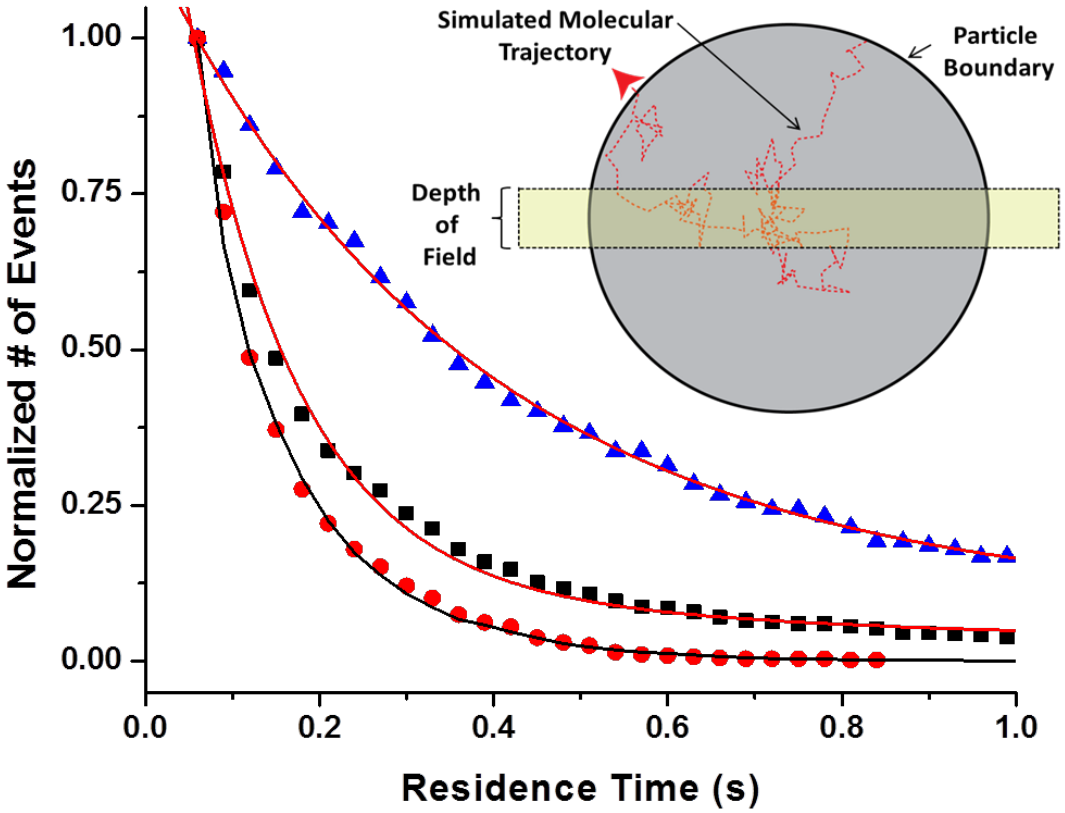

Figure 2.9**.** Residence-time histograms for all trajectories (black squares), trajectories that contained stuck events (blue triangles), and trajectories with no stuck events (red circles). The first two histograms are fit to biexponential decay functions (red lines), while the residence times of moving molecules are plotted with a 3-D random-walk simulation (black line) based on the measured diffusion coefficient and *no adjustable parameters* (see inset diagram).

molecular visits that include strong adsorption make up only a small (12%) fraction of the total visits into the field of view within the particle, their presence increases the residence times for *all* molecules (τ_{res} = 0.19 ±0.02 s) by a factor of nearly 2.5.

Because the molecular displacement distribution of *moving molecules* appears to be governed by a simple random walk (Figures 2.4b and 2.5), a Monte Carlo simulation based on a three-dimensional random walk within a depth-of-field-limited spherical geometry was developed to simulate residence times of freely diffusing molecules within a particle. Molecular trajectories were seeded at a random location on the outer surface of a 3-μm diameter sphere, the average size of the chromatographic media used in these experiments. Molecules would then step at a random angle, with displacements drawn randomly from the probability distribution of moving molecules (Figure 2.4b) until the molecule returned to the outer boundary of the sphere. The depth of field of the microscope was incorporated into the simulation by reporting the residence times of molecules while they were within the 0.6-μm depth of field in the z-dimension (see Figure 2.9 inset). The histogram of the residence times of molecules within the particle from the simulation is plotted in Figure 2.9, along with the experimental histogram of residence times of moving molecule trajectories that did not exhibit any strong-adsorption events. The simulation has *no adjustable parameters* and shows remarkable agreement with the residence-time data for moving molecules. Because the simulated residence times are based on a homogeneous random walk, the agreement between simulated and moving-molecule residence times further shows that, with the exception of strong-adsorption events that arrest molecular motion, intraparticle transport is homogenous throughout the interior of the particle, well modeled by a random walk at

the measured diffusion coefficient of single molecules.

As a second test of whether molecular transport is homogeneous throughout the particle, the spatial distribution of molecules within the silica particles was characterized. This was done by generating a histogram of radial positions relative to the center of the particle for each identified molecule in every frame and normalizing the histogram to the total number of molecules. The same analysis was carried out on the simulated random-walk trajectories, and the results are compared in Figure 2.10. The measured radial distribution of molecular locations is again consistent with the predictions of a homogeneous random walk, and supports the idea that the molecules in the silica particle are randomly distributed in a homogeneous environment. The probability of finding molecules near the center of the particle is small simply because of its small relative volume and increases linearly as the radial distance from the center increases. This linear dependence on distance is a consequence of the depth of field of observation, h, where the volume of the slab increases in proportion to $\sim 2\pi rh$ (see Figure 2.10), while for the entire spherical particle, one would expect the radial probability density to increase quadratically with r by the area of a spherical shell, $4\pi r^2$ (see below).

2.3.5 Summary and perspective

This study presents the adaptation of single-molecule fluorescence imaging microscopy for direct observation of molecular transport within reversed-phase chromatographic silica particles. Octadecyl-rhodamine B molecules were imaged within C_{18}-modified porous silica particles to generate movies at video-framing rates of molecular visits to the stationary phase. Single-molecule detection and tracking were used to follow the trajectories of individual molecules throughout their visit to the field of

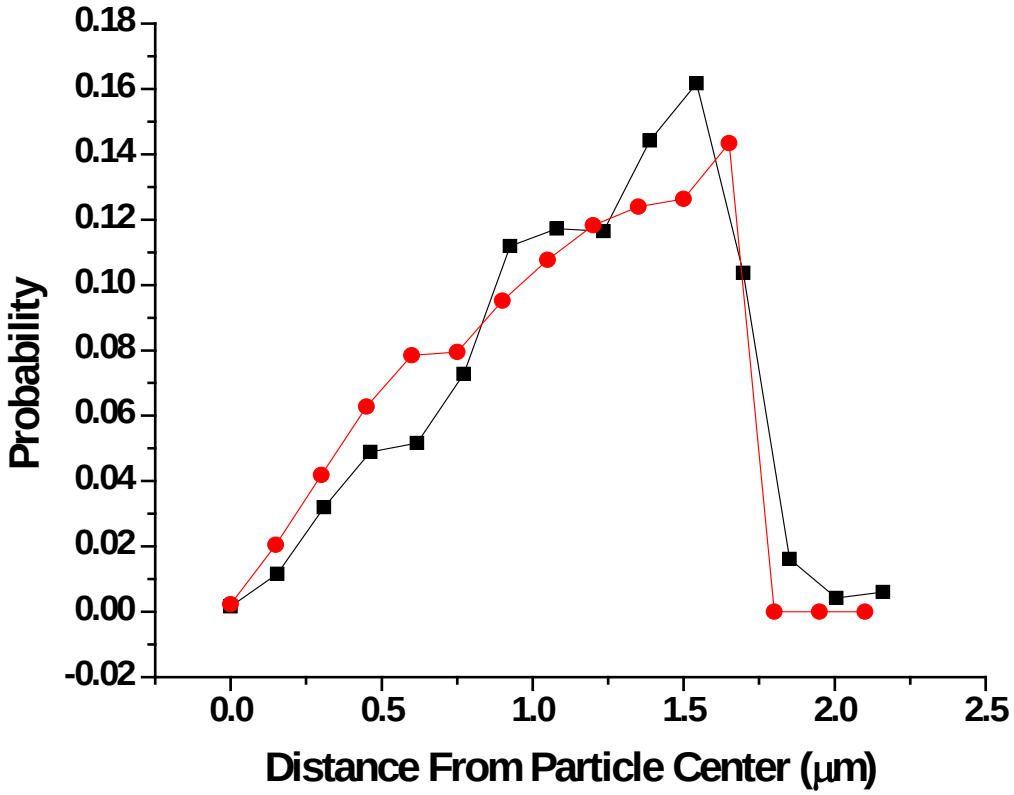

Figure 2.10. Radial probability distribution of molecules within RPLC particles, experimental data (blacks squares) and Monte Carlo simulation of random walk (red dots) within the depth of field in the particle.

view within the particle in order to measure residence times and the intraparticle diffusion coefficient. Statistical criteria based on the molecule-localization resolution and random-walk displacement distribution were developed to divide molecular trajectories into moving and stationary (stuck) time segments. These stuck events are direct evidence of the heterogeneity of analyte interactions with the chromatographic media, where the stationary molecules held fixed by strong adsorption would be a contributor to peak tailing in chromatographic elution.[14,58,59] When compared with trajectories with no strong adsorption events, trajectories that included stuck events exhibited 10-times longer residence times. While these trajectories only make up 12% of the molecular visits, they more than double the average residence time of all molecules within the particle.

While single-molecule imaging provides unique insight into the dynamics of molecules visiting chromatographic particles, there are several limitations associated with these experiments. The high-numerical-aperture objective needed to acquire sufficient fluorescence to detect and track signal molecules has a limited depth of field that confines our view to a slab encompassing roughly $1/5^{th}$ of the particle depth and $1/3^{rd}$ of its volume, within which we resolve motion in only two dimensions. In addition, high-retention conditions (k' = 490) are required to retain molecules in the particle for sufficient time to measure trajectories at the framing rate of the CCD camera. At such high-retention conditions, analyte molecules are expected to spend ~99.8% of their time on the stationary phase, and thus their transport through the particle is dominated by surface diffusion, which is significantly slower than diffusion in the mobile phase.[19–21]

Despite these limitations, the displacements of moving molecules could be

distinguished with confidence from stuck molecules. The residence times of moving molecules and the radial distribution of molecules within the particle are well described by a simple three-dimensional random-walk simulation, based on the experimentally measured diffusion coefficient and no fitted parameters. This suggests a pore structure that is homogenous on the distance scales of our spatial (0.064 μm) and time (30 ms) resolution. The radial probability distribution shows that molecules are more likely to be found close to the particle surface, where the probability of penetrating into the center of the particles is limited by its smaller relative volume. Given the success of modeling moving-molecule residence times within the measurement depth of field (Figure 2.10), a random-walk Monte Carlo simulation was applied to predicting residence times within the entire 3-μm particle and is shown in Figure 2.11. Average residence times are three-times longer compared to a depth-of-field-limited slab, and there is an even greater impact on the dispersion in residence times. A large fraction of very short residence times is observed due to the increased outer surface of the particle through which molecules can diffuse compared to the boundaries of the depth of field. The long-residence-time molecules are a smaller fraction (the relative volume of the interior is smaller in a sphere than in a cylindrical slab) but the characteristic residence times are greater by an *order of magnitude* because they must diffuse over a three-fold greater distance than the thickness of the slab, in order to escape the particle. In future work, depth resolution of the motions of molecules within a particle could be possible through the use of astigmatic optics in the image path and autofocus control[63] to track the z-axis motion of the molecules within the particle, even to the outer bounds of the particle surface.

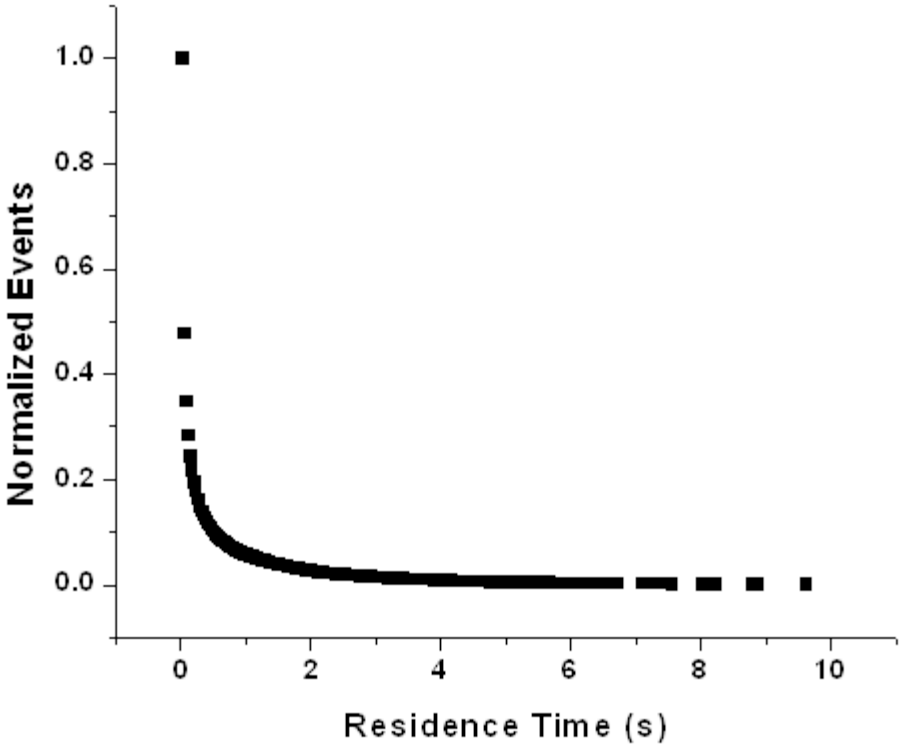

Figure 2.11. Histogram of predicted intraparticle residence times. Residence times of R18 molecules diffusing within a 3μm RPLC particle are predicted by a Monte Carlo simulation based on the measured intraparticle, R18 diffusion coefficient. Compared to the slab geometry of the present experiment (Figure 2.9, red symbols), average molecular residence times in the entire particle are greater by a factor of three, and the tail of the residence-time distribution extends nearly an order of magnitude to longer times. See manuscript text for details.

Intraparticle molecular transport plays a significant role in the resolution and separation efficiency of reversed-phase chromatographic techniques. This research provides a unique view of the transport of individual molecules within porous silica particles and insight into the timescales of fundamental processes that govern chromatographic separations. Agreement between experimental data and simulation demonstrates the potential of this technique to be used to model molecular transport within porous structures whose geometries are not amenable to direct, single-molecule observation.

2.4 Acknowledgments

This research was supported in part by the U.S. Department of Energy under Grant DE-FG03-93ER14333. Additional support from Agilent Technologies in the form of a University Relations Grant is gratefully acknowledged.

2.5 References

(1) McKittrick, M. W.; Jones, C. W. *J. Am. Chem. Soc.* **2004**, *126*, 3052.

(2) Foote, R. S.; Khandurina, J.; Jacobson, S. C.; Ramsey, J. M. *Anal. Chem.* **2004**, *77*, 57.

(3) Wang, Y.; Caruso, F. *Chem. Mater.* **2005**, *17*, 953.

(4) Kim, J.; Grate, J. W.; Wang, P. *Chem. Eng. Sci.* **2006**, *61*, 1017.

(5) Charnay, C.; Bégu, S.; Tourné-Péteilh, C.; Nicole, L.; Lerner, D. A.; Devoisselle, J. M. *Eur. J. Pharm. Biopharm.* **2004**, *57*, 533.

(6) Holthoff, E. L.; Bright, F. V. *Acc. Chem. Res.* **2007**, *40*, 756.

(7) Patel, A. C.; Li, S.; Yuan, J.-M.; Wei, Y. *Nano Lett.* **2006**, *6*, 1042.

(8) Unger, K. K. *Porous Silica: Its Properties and Use as Support in Column Liquid Chromatography*; Elsevier Science: Amsterdam, 1979.

(9) Iler, R. K. *The Chemistry of Silica: Solubility, Polymerization, Colloid and Surface Properties and Biochemistry of Silica*; Wiley: New York, 1979.

(10) Dorsey, J. G.; Dill, K. A. *Chem. Rev.* **1989**, *89*, 331.

(11) Rouquerol, D.; Avnir, C. W. F.; D. H. Everett; J. M. Haynes; N. Pernicone; J. D. F. Ramsay; Sing, K. S. W.; Unger, K. K. *Pure Appl. Chem.* **1994**, *66*, 1739.

(12) Snyder, L. R.; Kirkland, J. J.; Dolan, J. W. *Introduction to Modern Liquid Chromatography*; 3rd ed.; John Wiley & Sons: Hoboken, 2010.

(13) van Deemter, J. J.; Zuiderweg, F. J.; Klinkenberg, A. *Chem. Eng. Sci.* **1956**, *5*, 271.

(14) Giddings, J. C. *Dynamics of Chromatography*; Marcel Dekker: New York, 1965.

(15) Giddings, J. C. *Unified Separation Science*; Wiley: New York, 1991.

(16) Seidel-Morgenstern, A.; Jacobson, S. C.; Guiochon, G. *J. Chromatogr. A* **1993**, *637*, 19.

(17) Guiochon, G.; Golshan-Shirazi, S.; Katti, A. M. *Fundamentals of Preparative and Nonlinear Chromatograph*; Academic Press: Boston, 1994.

(18) Miyabe, K.; Guiochon, G. *J. Chromatogr. A* **2000**, *890*, 211.

(19) Miyabe, K.; Guiochon, G. *J. Phys. Chem. B* **1999**, *103*, 11086.

(20) Miyabe, K.; Guiochon, G. *J. Chromatogr. A* **2002**, *961*, 23.

(21) Gritti, F.; Guiochon, G. *Anal. Chem.* **2006**, *78*, 5329.

(22) Burbage, J. D.; Wirth, M. J. *J. Phys. Chem.* **1992**, *96*, 5943.

(23) Zulli, S. L.; Kovaleski, J. M.; Zhu, X. R.; Harris, J. M.; Wirth, M. J. *Anal. Chem.* **1994**, *66*, 1708.

(24) Hansen, R. L.; Harris, J. M. *Anal. Chem.* **1995**, *67*, 492.

(25) Hansen, R. L.; Harris, J. M. *Anal. Chem.* **1996**, *68*, 2879.

(26) Hansen, R. L.; Harris, J. M. *Anal. Chem.* **1998**, *70*, 4247.

(27) Wirth, M. J.; Swinton, D. J. *Anal. Chem.* **1998**, *70*, 5264.

(28) Swinton, D. J.; Wirth, M. J. *Anal. Chem.* **2000**, *72*, 3725.

(29) Wirth, M. J.; Swinton, D. J.; Ludes, M. D. *J. Phys. Chem. B* **2003**, *107*, 6258.

(30) Wirth, M. J.; Legg, M. A. *Annu. Rev. Phys. Chem.* **2007**, *58*, 489.

(31) Honciuc, A.; Schwartz, D. K. *J. Am. Chem. Soc.* **2009**, *131*, 5973.

(32) Elliott, L. C. C.; Barhoum, M.; Harris, J. M.; Bohn, P. W. *PCCP* **2011**, *13*, 4326.

(33) Elliott, L. C. C.; Barhoum, M.; Harris, J. M.; Bohn, P. W. *Langmuir* **2011**, *27*, 11037.

(34) McCain, K. S.; Harris, J. M. *Anal. Chem.* **2003**, *75*, 3616.

(35) McCain, K. S.; Hanley, D. C.; Harris, J. M. *Anal. Chem.* **2003**, *75*, 4351.

(36) Fu, Y.; Ye, F.; Sanders, W. G.; Collinson, M. M.; Higgins, D. A. *J. Phys. Chem. B* **2006**, *110*, 9164.

(37) Ye, F.; Higgins, D. A.; Collinson, M. M. *J. Phys. Chem. C* **2007**, *111*, 6772.

(38) Ye, F.; Collinson, M. M.; Higgins, D. A. *PCCP* **2009**, *11*, 66.

(39) Brinker, C. J.; Scherer, G. W. *Sol-Gel Science: The Physics and Chemistry of Sol-Gel Processing*; Academic Press: Boston, 1990.

(40) Zhong, Z.; Lowry, M.; Wang, G.; Geng, L. *Anal. Chem.* **2005**, *77*, 2303.

(41) Zhong, Z.; Geng, M. L. *Anal. Chem.* **2007**, *79*, 6709.

(42) Gasser-Ramirez, J. L.; Harris, J. M. *Anal. Chem.* **2009**, *81*, 2869.

(43) Gasser-Ramirez, J. L.; Harris, J. M. *Anal. Chem.* **2009**, *81*, 7632.

(44) Gasser-Ramirez, J. L.; Harris, J. M. *Anal. Chem.* **2010**, *82*, 5743.

(45) Wirth, M. J.; Fatunmbi, H. O. *Anal. Chem.* **1992**, *64*, 2783.

(46) Olson, L. G.; Lo, Y.-S.; Beebe; Harris, J. M. *Anal. Chem.* **2001**, *73*, 4268.

(47) Peterson, E. M.; Harris, J. M. *Anal. Chem.* **2009**, *82*, 189.

(48) Ludes, M. D.; Anthony, S. R.; Wirth, M. J. *Anal. Chem.* **2003**, *75*, 3073.

(49) Smith, E. A.; Wirth, M. J. *J. Chromatogr. A* **2004**, *1060*, 127.

(50) Nawrocki, J. *J. Chromatogr. A* **1997**, *779*, 29.

(51) Wirth, M. J.; Ludes, M. D.; Swinton, D. J. *Anal. Chem.* **1999**, *71*, 3911.

(52) Newby, J. J.; Legg, M. A.; Rogers, B.; Wirth, M. J. *J. Chromatogr. A* **2011**, *1218*, 5131.

(53) Barlow, R. J. *Statistics, A Guide to the Use of Statistical Methods in the Physical Sciences*; John Wiley & Sons: Chichester, 1989.

(54) Berg, H. C. *Random Walks in Biology*; Princeton University Press: Princeton, 1993.

(55) Sonnleitner, A.; Schütz, G. J.; Schmidt, T. *Biophys. J.* **1999**, *77*, 2638.

(56) Smith, P. R.; Morrison, I. E. G.; Wilson, K. M.; Fernández, N.; Cherry, R. J. *Biophys. J.* **1999**, *76*, 3331.

(57) Michalet, X.; Berglund, A. J. *Physical Review E* **2012**, *85*, 061916.

(58) Giddings, J. C. *Anal. Chem.* **1963**, *35*, 1999.

(59) Fornstedt, T.; Zhong, G.; Guiochon, G. *J. Chromatogr. A* **1996**, *741*, 1.

(60) Davis, J. M.; Giddings, J. C. *Anal. Chem.* **1985**, *57*, 2168.

(61) Chen, D.; Dovichi, N. J. *Anal. Chem.* **1996**, *68*, 690.

(62) Hanley, D. C.; Harris, J. M. *Anal. Chem.* **2001**, *73*, 5030.

(63) Hwang, W.; Bae, S.; Hohng, S. *Opt. Express* **2012**, *20*, 29353.

2.6 Supporting Information

2.6.1 Agilent Zorbax C_{18} particle characterization

The Zorbax chromatographic silica particles were characterized by nitrogen BET by Porous Materials, Inc. (Ithica, NY). The results are summarized in Table 2.1.

Table 2.1. Agilent Zorbax C_{18} particle characterization

Specific Surface Area	145.6 m^2/g
Average Pore Diameter	8.4 nm
Porosity	0.23

2.6.2 Epifluorescence Microscopy Details

Epi-illumination and collection was accomplished with an Eclipse TE200 inverted microscope (Nikon Corporation) equipped with a 100x 1.49 NA Apo-TIRF oil immersion objective having a working distance of 120 μm. Silica particles were first located using bright field illumination, and the objective was adjusted vertically until the focal plane was located at the center of the particle, where the particle perimeter is in sharp focus. Samples were excited using the 514.5 nm line from a Lexel Model 95 argon ion laser. The laser radiation was coupled into a polarization-maintaining single-mode optical fiber (Thorlabs) using an aspheric fiberport collimator/coupler (Thorlabs). Light emerging from the fiber was collimated using planoconvex achromatic lens and passed through a 514-nm narrow width band-pass filter (Semrock). The filtered excitation light intensity was measured at ~11 mW before the objective. This radiation was focused onto the back focal plane of the objective, which resulted in collimated light having a 50-μm beam diameter passing into the sample from the objective lens. Fluorescence emission from molecules within the particles was collected back through the same objective and passed through a filter cube containing a 532-nm single-edge dichroic beamsplitter and a 585-nm bandpass emission filter (Semrock). Filtered fluorescence emission was imaged at 100x magnification by a tube lens onto an Andor iXon^{EM}+ 897 EMCCD camera. See Figure 2.12.

Manipulation of the objective in order to have the focal plane lie in the center of the silica particle was accomplished via bright-field imaging, where the edges of the silica spheres are in sharp focus and well resolved (see Figure 2.13). Upon initial illumination with 514-nm laser light, the silica spheres were highly fluorescent, likely due

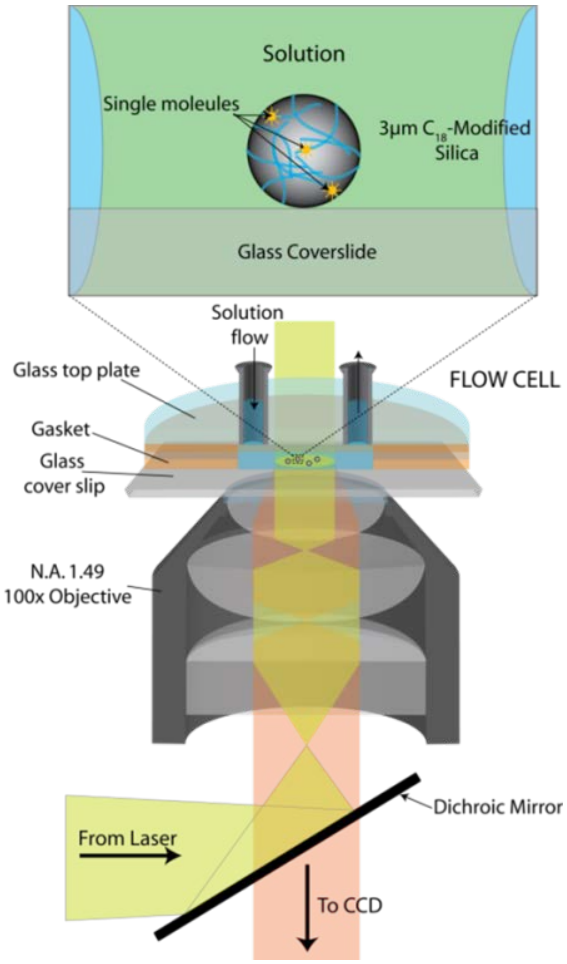

Figure 2.12. Schematic of single-molecule imaging microscopy optical setup.

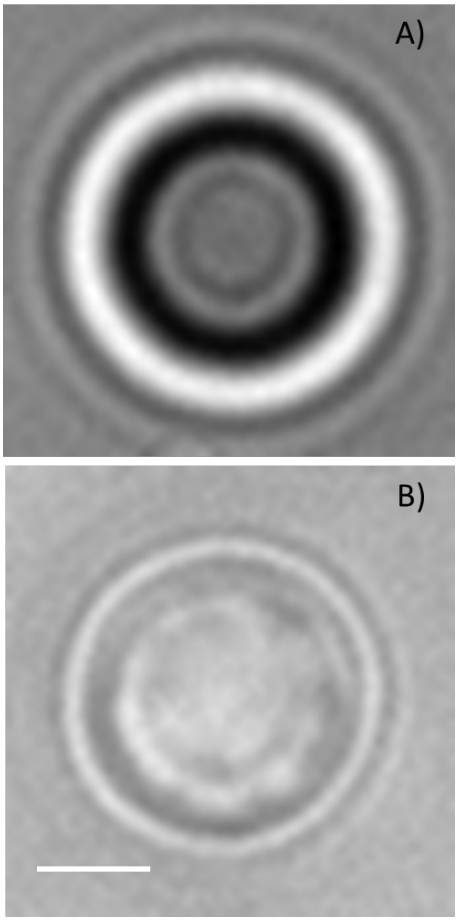

Figure 2.13**.** Bright field image with (A) the focal plane located above the particle and (B) the focal plane located at the center of the particle. Scale bar is 1 μm.

to fluorescent contaminants that had partitioned into the ODS stationary phase. This contaminant fluorescence was removed though photobleaching by exposing the silica particle of interest to continuous high intensity laser light (~400 W/cm^2) for 15–20 min which lowered the signal coming from within the particle to the level of the detector noise. Following photobleaching, a solution of 5 pM R18 in 30% methanol/water solution was introduced at 0.25 mL/min. This flow rate was kept constant throughout the experiment and an equilibration time of 15 min was allowed for complete solution exchange in the flow cell. Image sequences of single R18 molecules diffusing inside the porous silica particles were captured continuously for 4000 frames at 30-ms integration times (33.3 fps) and ~100x electron multiplication gain.

2.6.3 Image processing algorithms

Single-molecule movies were analyzed using custom analysis algorithms written in the Matlab (Mathworks) numerical computing environment. The algorithm for finding single molecules in the fluorescence images has been described previously.[1] Molecules in each frame are located by identifying regions that have at least three adjacent pixels with intensities greater than 2.5 standard deviations above the average background. This criterion utilizes the spatial distribution of intensity from single-molecule fluorescence imaged through the objective to discriminate against single-pixel background noise. The false positive probability (α) was determined with combinatorial statistics applied to the background noise to determine the probability of 3-adjacent pixels being above the 2.5-σ threshold.[1] The false negative probability was determined from the distribution of measured single-molecule intensities. The center-of-intensity-mass coordinates for each molecular spot, thus identified, were recorded in each frame for tracking the molecular

locations in two dimensions.

A custom single-molecule tracking algorithm was used to generate the molecular trajectories from the center of intensity mass coordinates of identified molecular spots. This algorithm measured the displacement, r_{ij}, of the center-of-intensity-mass coordinates of an identified molecular spot in one frame, i, relative to identified spots in the previous frame, j:

$$r_{ij} = \left[\left(x_j - x_i\right)^2 + \left(y_j - y_i\right)^2\right]^{\frac{1}{2}} \quad [2.3]$$

where $(x_j - x_i)^2$ and $(y_j - y_i)^2$ are the displacements of the x and y coordinate of the center-of-intensity mass, respectively. A maximum displacement limit (r_{max}) was chosen to limit the probability of two distant molecules being logged as a displacement of the same molecule. This was done by tracking the center-of-mass coordinates for well isolated, moving molecules over the course of their trajectories and measuring their displacements between frames. These measured displacements were then used to estimate the mean-squared displacement of diffusing molecules, ‹ r^2 ›. The root-mean-squared displacement was then scaled by a factor of 2.5 to produce the desired 99% confidence limit, where the integral from 0 to r_{max} = 2.5 ‹ r^2 ›$^{1/2}$ of the radial displacement distribution (Equation 2.1 in the manuscript) captures 99% of the single-frame radial displacements of R18 molecules. Thus r_{max} defines a circular region in the image centered at the coordinates of a located molecule where there is 99% chance of finding it in the next frame. If the coordinates of a located molecular spot in the subsequent frame are within r_{max}, then it was considered a displacement of the previous molecule, and its location and time stamp were added to the current trajectory. In this

way, the locations of molecules in each frame were correlated in space and time and stitched together to form displacement trajectories. If more than one molecule was found in the subsequent frame within the r_{max} radius, the location with smallest displacement is added to the current trajectory.

Because single-molecule fluorescence emission is a stochastic process, the number of photons collected from a single-molecule during the acquisition time of the camera varies from frame to frame and has a finite probability of being below the set intensity threshold. Furthermore, previous single-molecule experiments have reported on-off blinking behavior due to molecules entering dark states.[2–6] In order to mitigate the effect of single-molecule intensity fluctuations, a single frame blinking parameter was included in the tracking algorithm. If a spot intensity suddenly dropped below threshold or became dark for a frame, the tracking algorithm continues to look ahead to the next frame to see if the molecule had reappeared. If in this frame a molecule was detected within $1.4*r_{max}$, it was presumed that the molecule blinked off for one frame, and both the blinking frame and the subsequent frame were added to the current trajectory. Blinking times for rhodamine-like molecules in hydrophobic conditions have been reported in the μs time scale[7], making it unlikely that a molecule will blink for longer than a duration of one frame (30 ms). Tracking in this fashion continued until no molecules were found within the maximum radial displacement parameter in the subsequent frame in which case a new trajectory was begun for the next identified molecule not assigned to a previously recorded trajectory. This process was repeated until all identified molecules were assigned to a displacement trajectory.

2.6.4 References for Supporting Information

(1) Peterson, E. M.; Harris, J. M. *Anal. Chem.* **2009**, *82*, 189.

(2) Ambrose, W. P.; Goodwin, P. M.; Martin, J. C.; Keller, R. A. *Phys. Rev. Lett.* **1994**, *72*, 160.

(3) Lu, H. P.; Xie, X. S. *Nature* **1997**, *385*, 143.

(4) Yip, W.-T.; Hu, D.; Yu, J.; Vanden Bout, D. A.; Barbara, P. F. *J. Phys. Chem. A* **1998**, *102*, 7564.

(5) Gensch, T.; Böhmer, M.; Aramendía, P. F. *J. Phys. Chem. A* **2005**, *109*, 6652.

(6) Gao, F.; Mei, E.; Lim, M.; Hochstrasser, R. M. *J. Am. Chem. Soc.* **2006**, *128*, 4814.

(7) Zondervan, R.; Kulzer, F.; Orlinskii, S. B.; Orrit, M. *J. Phys. Chem. A* **2003**, *107*, 6770.

CHAPTER 3

IMAGING-FLUORESCENCE CORRELATION SPECTROSCOPY FOR MEASURING FAST SURFACE DIFFUSION AT LIQUID/SOLID INTERFACES

3.1 Introduction

The dynamics of molecules at liquid-solid interfaces plays a fundamental role in governing the chemistry of heterogeneous catalysis, chemical sensors, molecular recognition at biological membranes, and chemical separations. Characterizing the kinetic behavior of molecules at liquid-solid interfaces represents a measurement challenge due to the relatively small population of molecules at the interface compared with the overlaying bulk solution. Fluorescence spectroscopy techniques are well suited to measuring interfacial molecular populations due to high surface selectivity through internal-reflection excitation.[1,2] In addition, the high quantum yield of fluorescent probe molecules and the improved sensitivity of photodetectors have pushed detection limits for interfacial populations to the single-molecule limit. Fluorescence correlation spectroscopy (FCS), in which the signal fluctuations from a small population of molecules are correlated over time,[3–5] has provided a wealth of information about interfacial behavior of molecules including adsorption/desorption kinetics and the surface diffusion rates. Thompson and coworkers pioneered using total-internal-reflection

fluorescence-correlation spectroscopy (TIR-FCS) to measure biomolecule binding and unbinding rates of surface bound immunoglobulin.[2,6] Hansen and Harris employed TIR-FCS to measure the adsorption and desorption rates of rhodamine 6G at a C_{18}-modified fused silica interface while quantifying the surface population under varying solvent conditions.[7,8] Elson, Webb, and coworkers used TIR-FCS to measure the diffusion coefficient of fluorescently labeled lipids in cell membranes and compared results to those measured by fluorescence photobleach recovery.[9]

Wirth and coworkers pioneered the use of FCS and single-molecule residence time measurements to determine the surface diffusion rates of 1,1'-dioctadecyl-3,3,3'3'-tetramethylindocarbocyanine perchlorate (DiI) fluorescent probe molecules at model reversed-phase chromatographic (planar, C_{18}-modified) surfaces.[10,11] They were able to measure the diffusion rates of molecules at the interface by FCS under varying solvent conditions and to identify strong adsorption sites within the probing region that arrest motions of molecules for a period of time, producing a steady intensity while a molecule remains "stuck."[10,12,13] These strong sites are evidence of heterogeneity in surface interactions, which can be related to tailing of chromatographic peaks arising from a distribution of residence times on the surface.[12,14]

While FCS is a versatile technique for measuring diffusion at homogenous interfaces, the technique has limitations for surfaces that exhibit adsorption heterogeneity or mixed relaxation kinetics (diffusion together with adsorption and desorption, for example). In the former case, when long-lived adsorption events occur during a segment of FCS data being used to measure the diffusion coefficient of moving molecules, one observes a long-lived tail in the autocorrelation that obscures the measurement of the

surface diffusion coefficient. In the latter case, the autocorrelation function decay used to measure diffusion also responds to other sources of fluorescence fluctuations, including desorption of molecules from the surface. To distinguish autocorrelation decay from diffusion versus surface desorption, it is advantageous to measure the decay rate as a function of the size of the probing region.[15] By changing the distance over which diffusional relaxation occurs, one can observe changes in the relaxation time that are related directly to the diffusion coefficient.[16,17] With typical FCS measurements made at a focused laser spot, however, varying the size of the probe volume is challenging because it involves modifying the optics used for fluorescence excitation and emission collection.

Another approach to measuring interfacial molecular diffusion that overcomes some of the above limitations of FCS is fluorescence imaging and tracking of motions of individual molecules. This methodology was first pioneered to track the motions of fluorescently labeled proteins on cell membranes[18,19,20] and supported lipid bilayers.[20,21] For studies of transport at liquid-solid interfaces, tracking motions of individual fluorescent molecules over large areas of a flat surface can provide important insight into the heterogeneity of diffusional trajectories and its relationship to the chemistry of the underlying surface. This concept was demonstrated for diffusion of fluorescently labeled alkanoic acids at a fused silica-hydrocarbon[22] and methylated silica-water interfaces[23] and of amphiphilic dyes in stimulus-responsive thin films of poly(N-isopropylacrylamide) below and above their critical transition temperature.[24,25] Single-molecule imaging and tracking have also been adapted to porous silica films and particles to investigate the influence of pore structure and surface interactions on molecular transport within both thin porous sol-gel films[26–29] and reversed-phase chromatographic silica particles.[30]

These measurements reveal spatial heterogeneities in silica structure that lead to localized variations in molecular diffusivities, where molecular motions depend on the chemistry of the fluorescent probe molecule, the ordering of the film during deposition, and treatment of the pore surface. Single-molecule tracking can provide information about molecular transport over large surface areas (typically greater than FCS measurements at a fixed focused spot); however, temporal resolution is limited by the exposure time needed to achieve a signal-to-noise ratio sufficient to identify and track molecules and/or by the time to readout the CCD image.[19,31–33] When molecular motion is faster than the minimum exposure time or detector readout time, the single-molecule fluorescence will be spread over many pixels and have low a signal-to-noise ratio, making it difficult to identify and track molecules. Measuring fast dynamics by single-molecule tracking can be accomplished with fast EM-CCD detectors,[34,35]; however, this approach requires the use of very high excitation power densities (5 to 10 kW/cm^2) to provide adequate signal-to-noise, along with the use of robust labels (quantum dots) or photostabilizing chemical agents to mitigate fluorophore photobleaching.[36] Single-molecule tracking has typically been limited to systems that exhibit slow diffusion, such as labeled biomolecules in lipid membranes or dyes that strongly interact with polymer networks, n-alkyl chains, or sol-gel micropores.

In the present work, we employ a combination of fluorescence imaging with an autocorrelation analysis, termed imaging-fluorescence-correlation spectroscopy or imaging-FCS, to characterize fast molecular transport at model (planar) chromatographic interfaces. This technique has been previously developed as an alternative to traditional confocal FCS and used to measure solution diffusion of fluorescent dyes,[37] as well as

diffusion of fluorescently labeled polystyrene beads and small molecule fluorescent probes in high-viscosity media and lateral diffusion of membrane-bound proteins on cell surfaces.[38,39] The technique has also been adapted to total-internal-reflection excitation for measuring lateral diffusion of labeled lipids in supported lipid bilayers[39,40] and has been characterized in terms of the influence of time- and spatial-resolution and the total measurement time and area on the precision of the results.[41,42] Because the read-out of an entire CCD image is relatively slow, camera-based imaging-FCS has generally been applied to slower, homogeneous diffusion in lipid bilayers and cell membranes. This technique, however, is versatile and can be used to characterize faster molecular transport at liquid-solid interfaces. By limiting the acquisition region on the CCD to a subset of pixels, the readout is more rapid than reading the entire chip, allowing kHz-framing rates capable of following fast diffusion comparable to small molecules in free solution. With modest excitation powers (~100 mW/cm^2), the S/N ratios of the resulting images are too low to allow tracking of individual molecules; the total intensity within the small interrogated region, however, generates a fluorescence time trace that can be autocorrelated and analyzed to determine the timescale of diffusional relaxation across that region. The location of the small interrogated region on the surface can be selected electronically to avoid strong adsorption sites that generate stuck-molecule events, which interfere with the analysis of the moving population. These events can still be identified and characterized in the sequence of images, as previously accomplished in single-molecule tracking experiments.[30] The most important advantage of this method is that the size (area) of the interrogated region can be controlled digitally so that diffusional contributions to the relaxation rate can be unambiguously separated from other sources of

fluorescence fluctuations in the data. These concepts are applied to a study of 1,1'-dioctadecyl-3,3,3'3'-tetramethylindocarbocyanine (DiI) at model (planar) reversed-phase chromatographic surfaces. By varying the alkyl ligands (C_{18} versus C_1) on the surfaces, we observe significant differences in surface-diffusion rates, surface homogeneity, molecule retention, and adsorption-desorption rates, which provide insight into the nature of interfacial molecular dynamics at long- and short-chain alkylsilane-modified surfaces.

3.2 Experimental Section

3.2.1 Chemicals and materials

1,1'-dioctadecyl-3,3,3'3'-tetramethylindocarbocyanine perchlorate (DiI) was purchased from Invitrogen (Carlsbad, CA). Serial dilutions of DiI were made into Omnisolv spectroscopy grade methanol from EMD chemicals (Darmstadt, Germany). Glass coverslips, used as substrates for derivatization were obtained from VWR International (Radnor, PA). Coverslips were silanized using trichloro(octadecyl)siliane (C_{18}) and trichloro(methyl)siliane (C_1) in n-heptane, acquired from Sigma-Aldrich Corp. (St. Louis, MO). Custom flow cells were constructed using luer-lock adapters and tubing from Value Plastics Inc. (Fort Collins, CO). All aqueous solutions were made using 18 MΩ-cm water, purified using a Barnstead NANOpure II system (Boston, MA). ACS-grade sodium chloride from Mallinckrodt (Phillipsburg, NJ) was used as supporting electrolyte (10-mM) in all aqueous solutions.

3.2.2 Preparation of model RPLC surfaces.

Planar analogs of reversed-phase chromatographic materials were prepared by chemically modifying the surface of 22-x-22-mm No. 1.5 glass coverslips with alkyl-

silane reagents. Coverslips were first cleaned in UV-generated ozone for 25 min on each side, yielding a water contact angle of ~0˚. Trichloro(octadecyl)silane was reacted by self-assembly onto the glass surface by a procedure similar to that introduced by Sagiv[43] and refined by Wirth et al.[44] Briefly, 12 coverslips in a ceramic holder were placed into a beaker containing 150 mL n-heptane; trichloro(octadecyl)silane was added to achieve a 0.5-mM concentration, and self-assembly from n-heptane solution proceeded at room temperature for a period of ~12 h. Reaction with the C_{18} silane was followed by endcapping with trichloro(methyl)silane from a 0.5-mM solution in n-heptane for another 12 h. Coverslips were then rinsed in n-heptane and dried in an oven at 120 ˚C for 1 h to promote crosslinking. Dried coverslips were then rinsed with dichloromethane and methanol and stored in methanol until use. The quality of surface modification was assessed by determining the water contact angle using a sessile drop method. Contact angles for C_{18}-derivatized coverslips generally fell between 110˚ and 112˚, indicating a high alkylsilane coverage and a strongly hydrophobic surface. A second set of coverslips was prepared with methyl groups on the surface, where trichloro(methyl)silane was reacted from a 0.5-mM solution in n-heptane for 12 h. Coverslips were then rinsed in n-heptane and dried in an oven at 120˚ C for 1 h to promote crosslinking. These C_1 surfaces were used to generate a less hydrophobic interface as evidenced by a smaller water contact angle of ~95˚.

3.2.3 Imaging-FCS data acquisition and processing

C_{18} and C_1 derivatized slides were placed in a flow cell though which a 20 pM solution of DiI molecules in 90/10 (v/v) methanol/water solution was flowed at 200 μL/min continuously throughout each experiment. DiI molecules diffusing at the

hydrophobic interface were imaged using an Eclipse TE200 inverted microscope (Nikon Corp.), illuminated with a 20-mW 514.5-nm laser beam, fiber-optically coupled into the back of a 60x 1.49 N.A. Apo-TIRF oil immersion objective lens producing 114 mW/cm^2, total-internal-reflection excitation of sample fluorescence, which is imaged onto an Andor iXon^{EM}+ 897 EMCCD camera (details in Supporting Information). Fluorescence correlation spectroscopy is based on measuring fluorescence fluctuations of molecules within a probing region.[3,4] An autocorrelation analysis of the fluorescence time-trace reveals the rate at which fluorescence is fluctuating by calculating the self-similarity of the fluorescence signals at varying time shift, τ (Equation 3.1).

$$G(\tau) = \lim_{T\to\infty} \frac{1}{T} \int_{-T/2}^{T/2} F(t)F(t+\tau)dt \qquad [3.1]$$

The autocorrelation function can be fit to a model with parameters relating to the physical processes responsible for the fluorescence fluctuations. For the case of surface diffusion, the decay of the autocorrelation function depends on the size of the probed area and the diffusion coefficient (Equations 3.2 and 3.3):

$$G(\tau) = A * \frac{1}{1+{}^{\tau}/_{\tau_{1/2}}} + B \qquad [3.2]$$

where the diffusion-controlled decay rate of the fluctuations is given by Einstein's relation for diffusion in two dimensions applied to diffusion across a spot of radius, ω,[3,45]

$$(1/\tau_{1/2}) = 4D_S/\omega^2 \qquad [3.3]$$

where D_s is the surface diffusion coefficient and ω^2 is the square of the radius of the

detection region.[3,41]

The surface is illuminated by total-internal-reflection, which limits excitation of fluorescent molecules to within a small distance (~100 nm) from the glass surface. Because the internal-reflection excitation covers a large area (~75-by-75 μm), the FCS probing region is instead restricted in the lateral dimension by a small, 8-by-8 pixel region acquired by the CCD detector. Fluorescence intensity time traces from this 64 pixel region were generated with 1.09-ms (exposure + read time) resolution by summing the total intensity within the entire region or subregion depending on the characteristic measurement area, ω^2, being tested. The acquired region could be chosen anywhere on the 512-by-512 pixel CCD chip resulting in a high degree of flexibility in the location and size of the active region, where the imaging time resolution of the CCD depends linearly on the number of rows that are acquired (see Supporting Information).

The total intensity in each acquired region or subregion produce fluorescence intensity time traces that were autocorrelated using an algorithm written in Matlab (Math-works), where their Fourier-transforms were multiplied by their complex conjugates to generate power spectra and then inverse Fourier-transformed to produce autocorrelation functions. To mitigate noise in the autocorrelation functions, the average of 10 autocorrelations was determined for each experimental condition by co-adding their power spectra and inverse Fourier-transforming the result. Background subtraction was accomplished by averaging 10 autocorrelation functions of a C_{18}- or C_1-aqueous solution interface with no fluorescent dye. This gives a measure of the intensity arising from fluorescence contamination and Raman scattering. The square root of this blank autocorrelation was then subtracted from the square root of the autocorrelation functions

of diffusing DiI taken under equivalent experimental conditions, and the result was resquared.[8,46]

3.3 Results and Discussion

3.3.1 Measuring surface diffusion at a model chromatographic interface

Imaging-FCS was used to measure the surface diffusion rates of the amphiphilic fluorescent probe DiI at a model (planar) reversed-phase (C_{18}) chromatographic interface. The interface comprised a high-contact-angle, C_{18} monolayer, in contact with a 90% methanol 10% water solution. An example of a slow framing-rate imaging series (33 Hz) frame showing DiI diffusing at this interface is shown in Figure 3.1 to illustrate the subregion sampled for FCS analysis. Sampling an 8-by-8 pixel sub-region allows a nearly 30-fold higher framing-rate, where 32768 images are acquired with 1.09-ms time resolution and then autocorrelated. Background-corrected averages of 10 such autocorrelation functions are plotted in Figure 3.2a, which fit well to the surface diffusion model (Equation 3.2).

In order to determine the diffusion coefficient and resolve it from other possible sources of autocorrelation decay, the dependence of the decay rate on the size of the probing region was explored. While accomplishing this task with traditional confocal FCS would require tedious manipulation of the focusing optics, it is easily achieved in imaging-FCS by redefining the dimensions of the imaging region, which could be done by an image processing step on the same kinetic series. Fluorescence time traces were autocorrelated using the central 4-by-4 and 2-by-2 pixel regions within the original 8-by-8 pixel kinetic series and are compared in Figure 3.2a. The measured decay rates depend

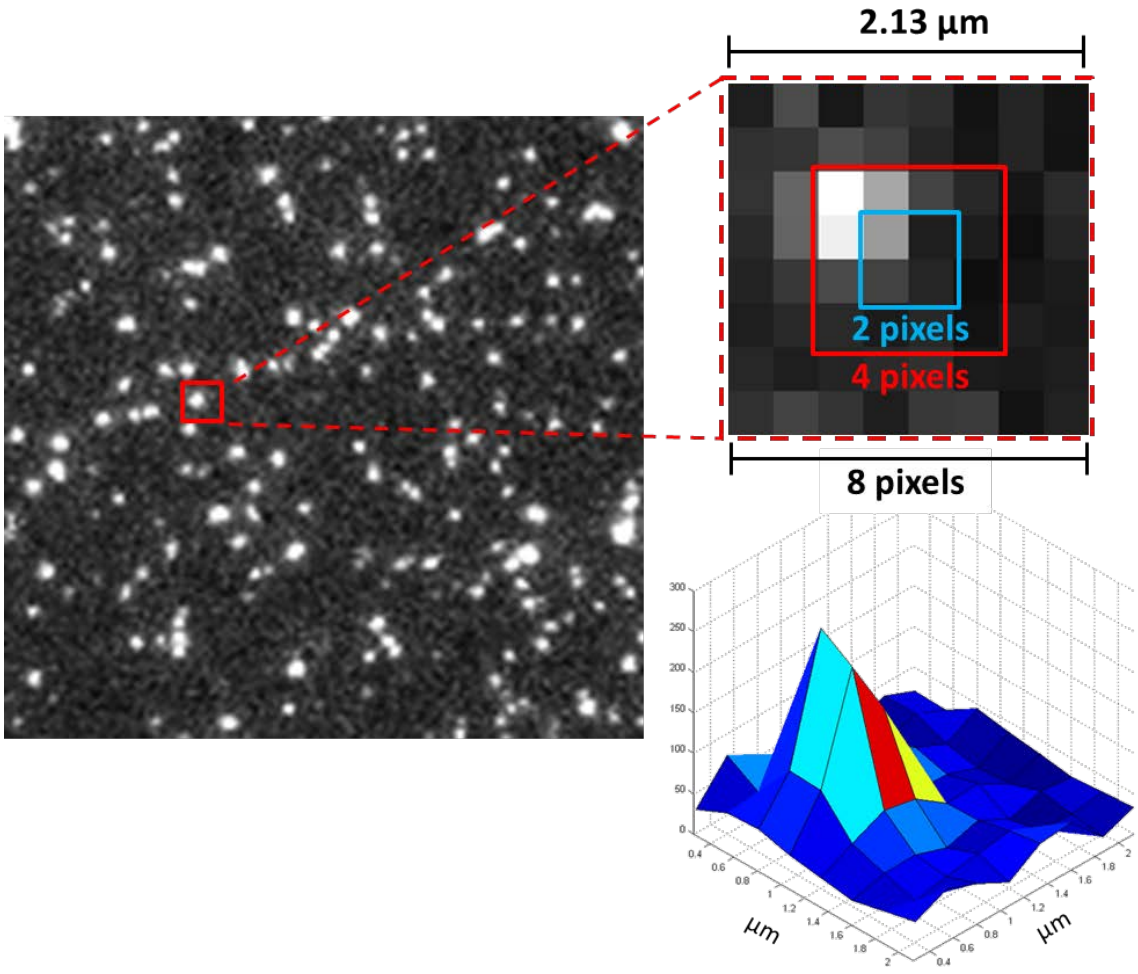

Figure 3.1. 128x128 pixel imaging of DiI on C_{18}-modified surface (30-ms acquisition time). Expansion shows the imaging-FCS acquisition areas, and a surface plot below illustrates the fluorescence intensity profile for the imaged molecule over the 8 x 8 pixel area. Molecular spots had an average signal-to-noise ratio of ~4.

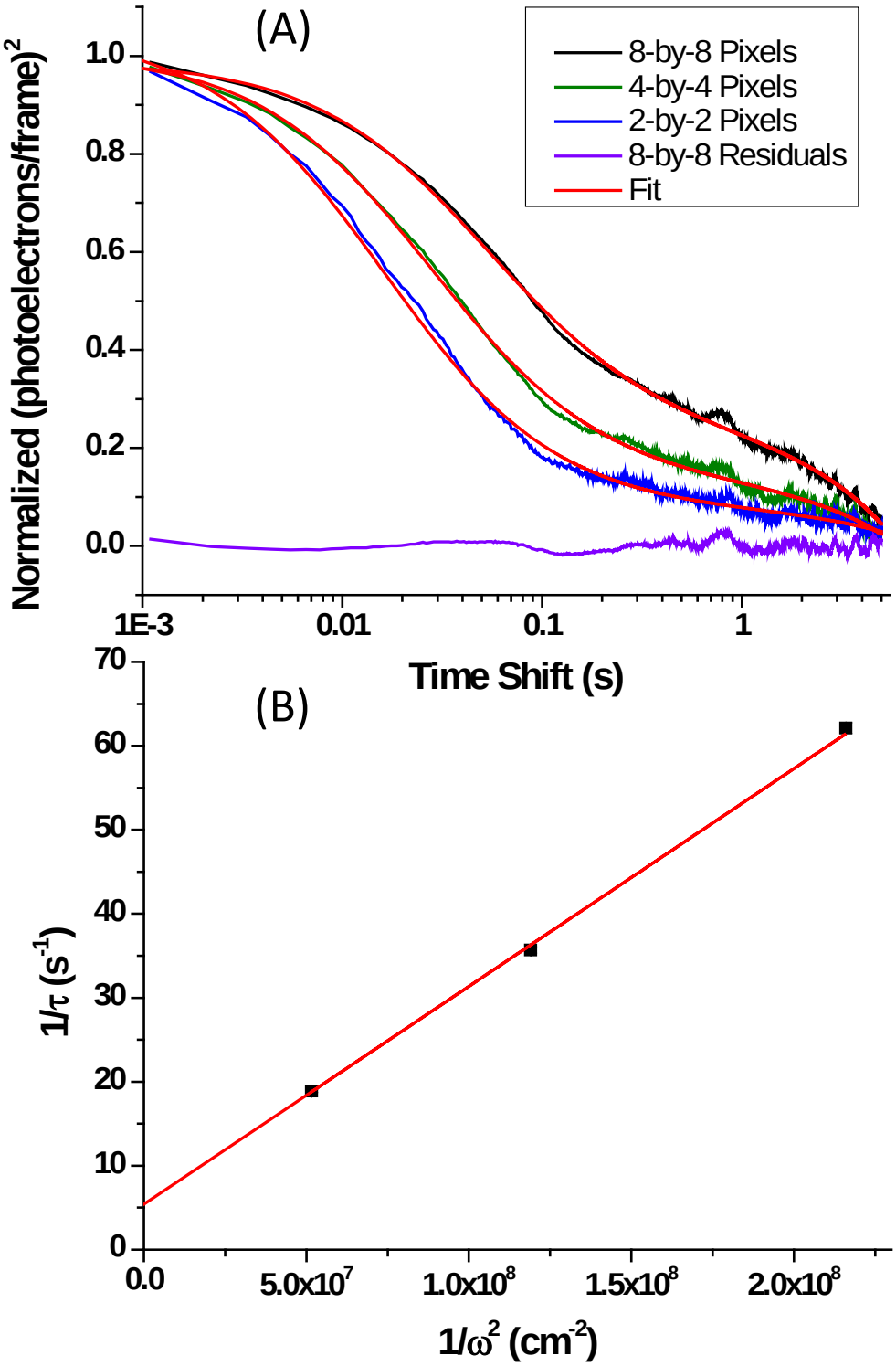

Figure 3.2. Probing region size dependent analysis of autocorrelation functions for DiI diffusion on a C_{18} interface (A) Normalized autocorrelation functions for varying probe region sizes fit to Equation 3.2. An example residual plot is from the 8-by-8 pixel autocorrelation included. (B) A plot of $1/\tau$ versus $1/\omega^2$ fit to Equation 3.3 with an intercept.

on the size of the probed region as predicted by Equation 3.3, where the decay rate, $1/\tau_{1/2}$, is proportional to $1/\omega^2$, where ω is the e^{-2} radius of the probed region determined by convoluting the square-imaging region with the point-spread function.[41] The decay rates were plotted as a function of the inverse of the effective area (Equation 3.3) yielding a linear relationship whose slope is proportional to the surface diffusion coefficient; see Figure 3.2b. The surface diffusion coefficient for DiI at the interface of a 90% MeOH 10% H_2O solution and a C_{18}-modified surface, thus determined, is D_S = 6.5 ± 0.2 x 10^{-8} cm^2/s. The intercept occurs where $1/\omega^2$ in Equation 3.3 is equal to zero, an extrapolation to an infinite probed area. The nonzero intercept at this limit indicates that there is a component of the autocorrelation decay that is independent of molecular diffusion on the surface.

In a total-internal-reflection-excitation geometry, intensity fluctuations that are independent of the probed area could be photobleaching of the DiI probe molecules, their diffusion in the evanescent wave, and adsorption-desorption kinetics. In order for photobleaching to influence the measured intercept, photobleaching lifetimes of DiI would need to be comparable to the inverse of the measured intercept rate. To determine the photobleaching lifetime of DiI, a large surface population of DiI was deposited on the C_{18} surface from a 0.5-nM solution in 90% methanol, and the solution was switched to a 10%-methanol solution having no DiI to produce a stable DiI surface population. Photobleaching of this population was measured at the same laser power used in FCS measurements (see Supporting Information), producing an average photobleaching lifetime, τ_{pb} = 12.5 ±0.1 s. This photobleaching rate is 1.6% of the intercept rate in Figure 3.2b and only 15% of the intercept uncertainty; thus, photobleaching does not contribute

to the intensity changes that are independent of probed area. Diffusion of DiI through the evanescent wave in solution might also contribute to area-independent relaxation. To determine the possible contribution of this process to the intercept rate, the diffusion coefficient of DiI in 90% methanol was estimated from the viscosity of 90% methanol, the van der Waals radius of DiI,[47,48] and the Stokes–Einstein equation, $D = k_b T/6\pi\eta r \sim 4$ x 10^{-6}cm^2/s. The one-dimensional diffusion time of DiI through the evanescent-field distance of x = 150 nm, $\tau_{ef} = x^2/2D$ = 27 μs, is 36 times faster than the millisecond interval between frames. Diffusional relaxation in the evanescent wave is therefore entirely contained in the $\tau = 0$ point, which is not fitted because it is dominated by high-bandwidth photoelectron shot noise.[7]

Thus, area-independent fluorescence fluctuations likely arise from adsorption-desorption kinetics,[7] where the sum of the adsorption and desorption rates governs the relaxation from a fluctuation back to equilibrium.[49] Because of fast flow of solution over the surface, concentration fluctuations of DiI in the solution phase are removed from the observation region more than 20-times faster than the intercept rate in Figure 3.2b. Because the solution concentration fluctuations are relaxed quickly to the equilibrium (bulk) concentration by solution flow, the adsorption rate does not contribute significantly (< 5%) to relaxation of the surface population, and the desorption rate of DiI dominates the measured area-independent relaxation rate (see Supporting Information). Thus, the intercept of Figure 3.2 reports the desorption rate of DiI from the C_{18} surface, where k_{desorb} = 5.4 (±0.6) s^{-1}. The ability to manipulate easily the size of the imaged area facilitates determining the diffusion coefficient and desorption rate with confidence, based on a fit to Equation 3.3.

3.3.2 Avoiding immobile molecules on strong adsorption sites

It is known that reversed-phase chromatographic interfaces are spatially heterogeneous with respect to their interactions with adsorbed molecules, which can influence the transport of molecules along the surface.[50–53] Aside from the delocalized interactions with the C_{18} stationary phase, which characterize the majority molecules diffusing along the surface, reversed-phase silica also contains strong adsorption sites to which molecules may bind and remain immobile for extended periods of time.[10,12] Fluorescence-correlation and single-molecule spectroscopies have provided evidence of surface sites where analyte adsorption is particularly strong and has linked these strong adsorption sites to chemically unmodified, isolated, or *active* silanols on the silica surface.[10,12,13,54] Direct evidence of the heterogeneity of molecular transport due to strong adsorption sites on the reversed-phase surfaces in the present experiments can be seen in the movies acquired at longer (30 ms) framing rates. In these data, it is evident that the majority of molecules diffuse freely over the surface; however, it is also apparent that there is a fraction of the molecular population on the surface that is immobile for relatively long times. Fluorescence correlation studies have shown that these strong adsorption events have an significant influence on the decay of the autocorrelation function in an FCS experiment.[55,56] Because the residence times of molecules adsorbed to strong sites are much longer than those of molecules freely diffusing through the probing region, the decay rate of fluorescence fluctuations from strong adsorption is dramatically slowed. This slower rate is manifested in an autocorrelation decay with a long tail, characteristic of the rate of molecule becoming “unstuck” from the adsorption site. In an FCS experiment, these longer decay times from strongly adsorbed molecules

can overwhelm the characterization of moving molecules.

Conventional FCS instrumentation does not allow for visualization of the surface being measured. Camera-based imaging, however, allows a large area on the surface to be viewed prior to the acquisition of FCS data. Molecular visits to strong adsorption sites are identified by mean-square displacements that do not exceed the molecular position uncertainty over multiple frames.[30] Using this criterion, strong adsorption sites can be located and then avoided in designating the active region for acquiring FCS data of moving molecules. Applying this analysis to movies of DiI diffusion on the C_{18} surface, the number of stuck molecules averaged 21.8 (±0.6) molecules per 128-by-128 pixel (1,160 μm^2) image area per frame. The probability of sampling a strongly adsorbed molecule in a random 8-by-8 pixel (4.5 μm^2) region of the surface is large, 8.5%. Sites where repeated (2 or more in 30 s) strong adsorption events occur can also be identified with a spatial resolution of 190 nm,[30] and these stable, revisited sites account for 90% of the strong absorption events, as is shown in Figure 3.3b. The impact of strong adsorption sites on autocorrelation results is illustrated in Figure 3.4, where the autocorrelation decay from the same sample is measured in two 8-by-8 pixel regions, one that contains a strong adsorption site and a second region where the molecules are all freely diffusing. The fitted autocorrelation decay time in the region of a strong adsorption site was $\tau_{1/2}$ = 2.6 (±0.3) s, while the decay time in the region of only free diffusion was $\tau_{1/2}$ = 0.47 (±0.01) s. Without prior knowledge of the heterogeneity of molecular transport on the surface, or without testing the dependence of the decay constant on the size of the probing region, the presence of one or more strong adsorption sites would bias the measured diffusion coefficient of moving molecules to a much slower result. Finally,

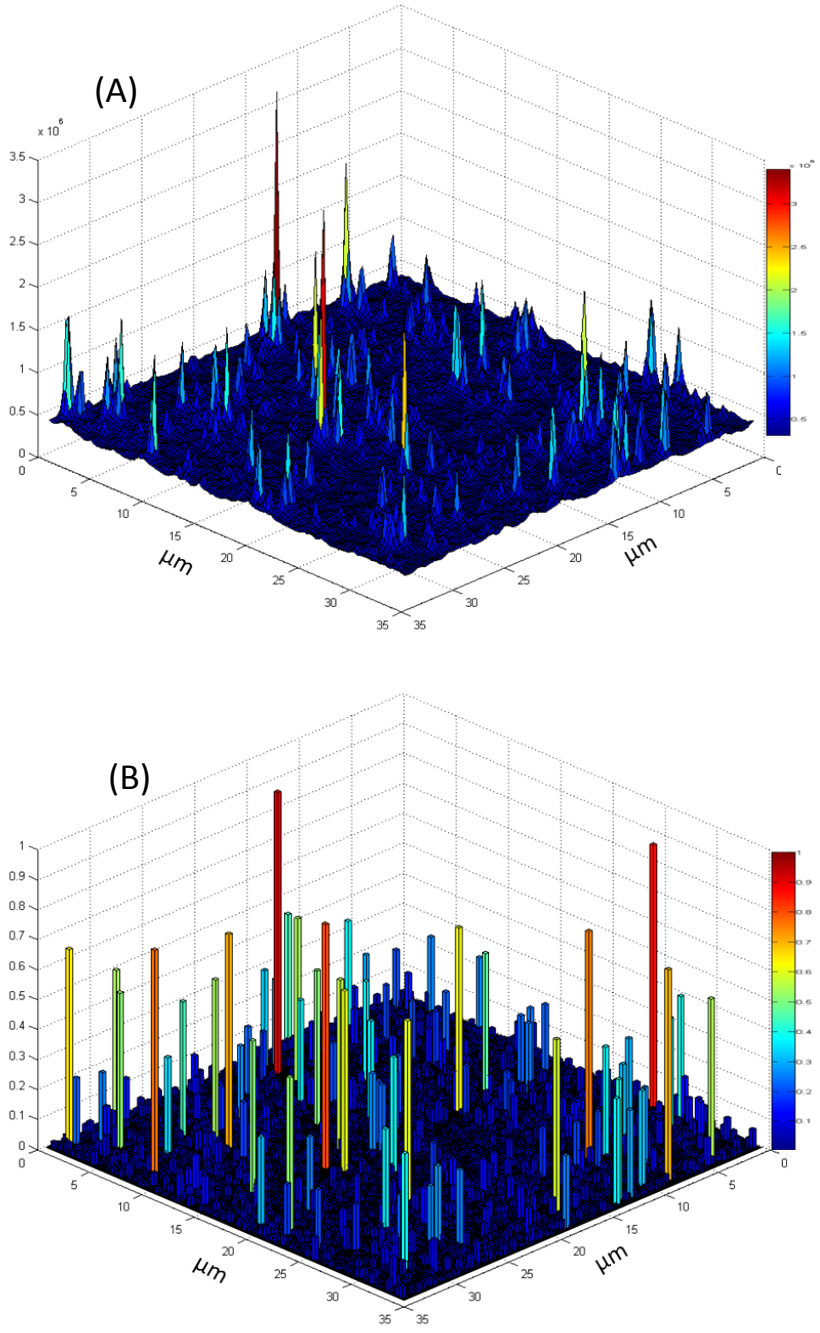

Figure 3.3. Spatial distribution of strong-adsorption events. (A) Total pixel intensity over a 30-s observation. (B) Stuck-sites are identified by radial displacements that do not exceed the molecular position uncertainty (0.19 μm) for two or more frames, and the probability of these sites being occupied is plotted. Strong adsorption is localized specific sites that are revisited; regions between these sites can be used to characterize the diffusion of moving molecules.

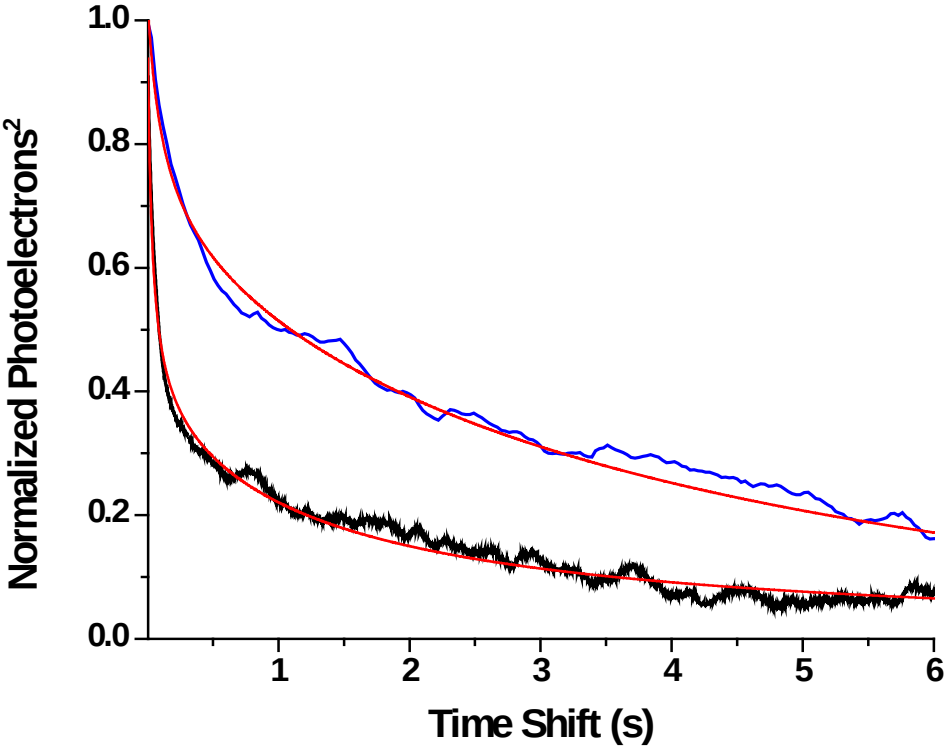

Figure 3.4. Autocorrelation decay from an 8-by-8 pixel region with negligible strong adsorption, $\tau_{1/2}$ = 0.47 ± 0.01 s (black points) and 8-by-8 pixel region with a strong adsorption site, $\tau_{1/2}$ = 2.6 ± 0.3 s (blue points), both fit to Equation 3.2.

using an imaging detector to identify strong adsorption sites not only allows one to avoid their influence in the acquisition of FCS data, one can also determine the spatial distribution of these sites on a surface,[30] as shown in Figure 3.3.

3.3.4 Measuring rapid interfacial diffusion under weaker retention conditions

In order to characterize the ability of imaging-FCS to measure faster interfacial diffusion rates, the diffusion coefficient of DiI was also measured at a methylated (C_1-derivatized) glass surface that exhibited weaker solute retention and faster surface diffusion. When DiI fluorescence is imaged at this interface, it was seen that its interfacial transport at the C_1 surface differs from that of the C_{18}-modified surface. A smaller population of molecules that are strongly adsorbed is observed, and the number of stuck molecules averages only 2.03 (±0.04) molecules per frame, or about $1/10^{th}$ the number on the C_{18} surface (see above), which is insufficient to generate a spatial distribution of sites. The vast majority of molecules diffuse freely and rapidly on this more homogeneous surface; their rapid motion is evident in their fluorescence being spread over a larger area during a 30-ms acquisition time (compare single-frame images of moving molecules on the C_{18} versus the C_1 surfaces in Figure 3.5). Thus the fluorescence of these rapidly diffusing molecules exhibits a low signal-to-noise ratio, which makes tracking their trajectories impossible. Shorter exposure times could reduce their motion during acquisition of an image, but this strategy further degrades the signal-to-noise ratio, so that tracking individual molecules would remain unachievable without significantly increasing the excitation power density.

Imaging-FCS analysis provides a means of acquiring diffusion data for rapidly-

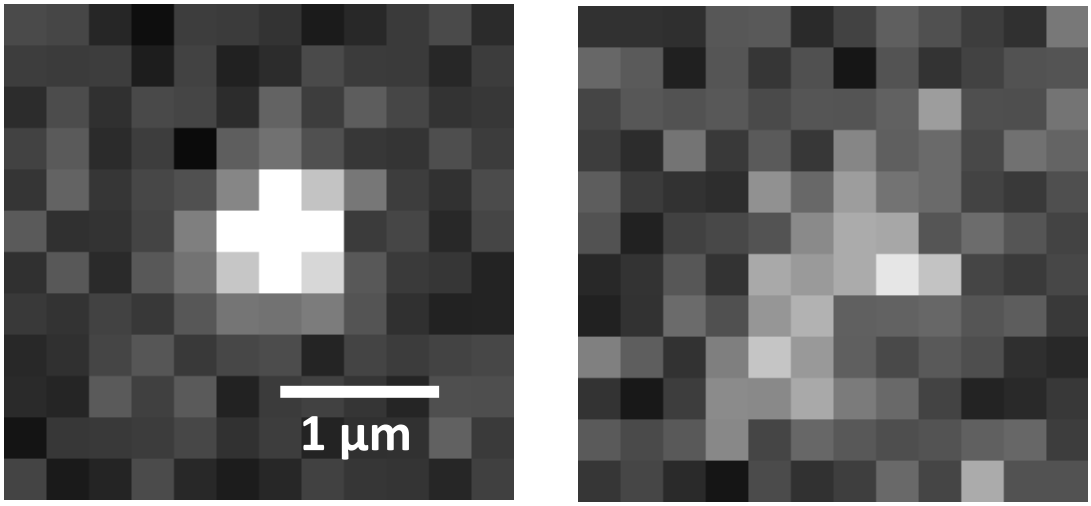

Figure 3.5. Single 30-ms frame images of DiI diffusing slowly on a C_{18} surface (left) versus fast diffusion on a C_1 surface (right). The motion of the molecule is nearly arrested within 30 ms on the C_{18} surface yielding a high S/N of ~4, while the rapid motion of DiI on the C_1 surface lowers the S/N to ~2 and smears out the fluorescence intensity, making localization not feasible.

moving molecules, and the resulting autocorrelation curves for a series of probe-region sizes and their corresponding relaxation rates are plotted in Figure 3.6. The relaxation rate depends linearly on the inverse of the probed area as predicted by Equation 3.3, and from the least-squares slope of the line, the diffusion coefficient of DiI at the C_1-surface was determined to be D_S = 3.3 (±0.2) x 10^{-7} cm^2/s. This result is 5-times faster than the diffusion of DiI on the C_{18} surface and about an order-of-magnitude slower than the diffusion of DiI in free solution (~ 4 x 10^{-6} cm^2/s for DiI under these conditions). The $(1/\tau)$ intercept corresponds to a desorption rate of DiI from the C_1 surface of k_{desorb} = 75.5 (±5.3) s^{-1} which is almost a factor of 14 faster than desorption of DiI from the C_{18} surface and is consistent with weaker DiI retention on the C_1 surface.

3.3.5 Quantifying interfacial molecular populations with imaging-FCS.

The fluorescence intensity fluctuations that are responsible for the autocorrelation response derive from the small numbers of molecules that are arriving and leaving the probed region. From the magnitude of the fluctuations, one can determine the number of fluorescing molecules being detected using Poisson statistics that govern their deviations from equilibrium.[8] The average fluorescence signal that is detected, $\langle F \rangle$, depends on the product of the number of molecules, $\langle N \rangle$, in the probing region and a sensitivity factor, k, which is the average detected photons per molecule per frame,

$$\langle F \rangle = k \langle N \rangle \qquad [3.4]$$

where k depends on a product of the excitation intensity, fluorophore absorption cross section, fluorescence quantum yield, and collection and detection efficiencies. The variance in the fluorescence signal, σ_F^2, can be estimated from the difference between the

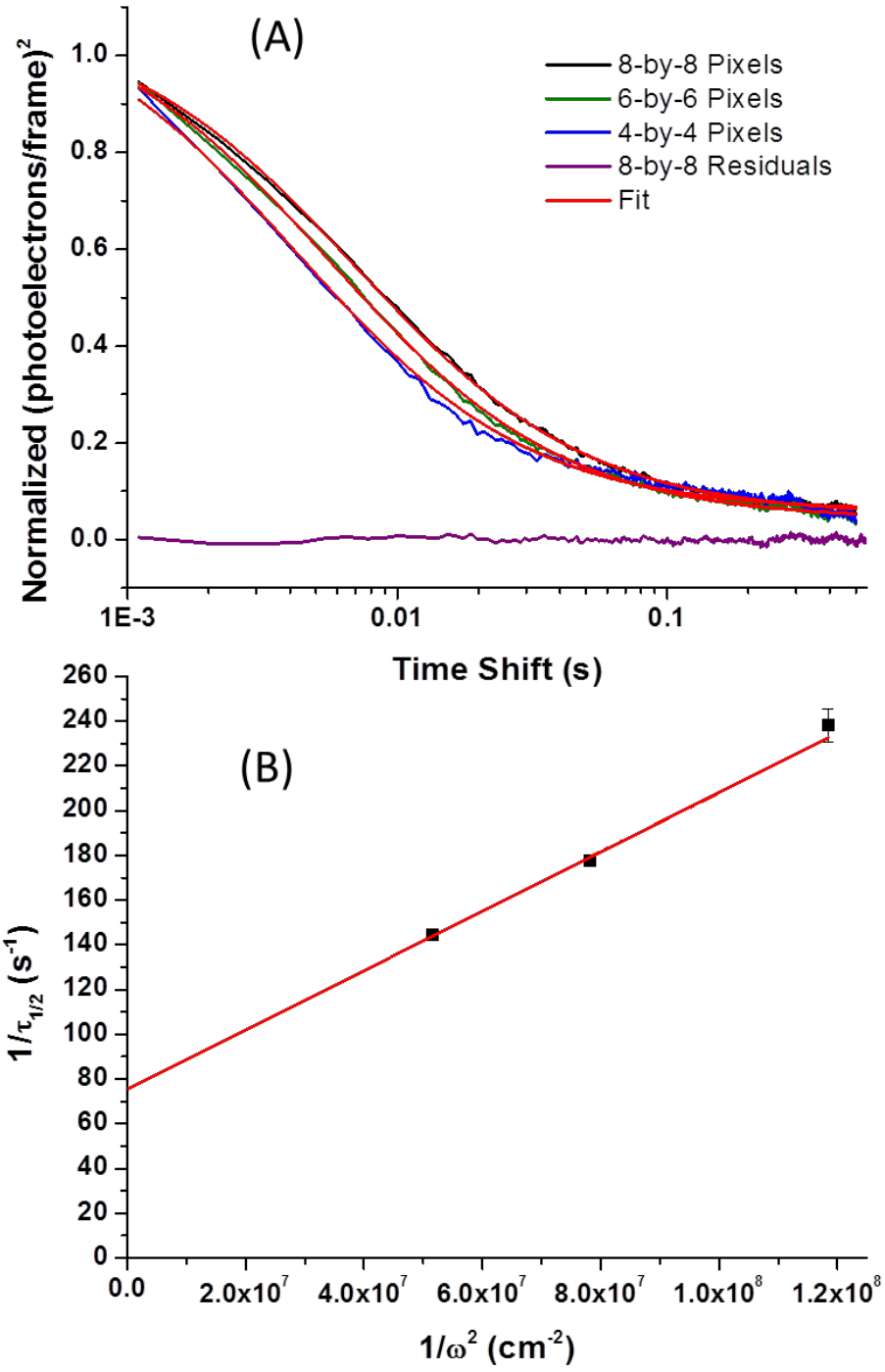

Figure 3.6. Probing region size dependent analysis of autocorrelation functions for DiI diffusion on a C_1 interface. (A) Normalized ACFs for varying probing region sizes (2.1 μm, 1.6 μm, and 1.1 μm) for DiI on a C_1-modified surface. An example residual plot for the 8-by-8 pixel autocorrelation is included. (B) Plot of $1/\tau$ versus $1/\omega^2$ and fit to Equation 3.3 with an intercept.

peak of the autocorrelation function at $\tau = 0$ relative to its amplitude at long times:

$$G(0) - G(\infty) = \langle F^2 \rangle - \langle F \rangle^2 = \sigma_F^2 \quad [3.5]$$

The fluorescence variance can be predicted from propagation of errors through Equation 3.4 and the variances in the number of molecules, σ_N^2, and also in the sensitivity factor, σ_k^2,

$$\sigma_F^2 = \left(\frac{d\langle F \rangle}{d\langle N \rangle}\right)^2 \sigma_N^2 + \left(\frac{d\langle F \rangle}{dk}\right)^2 \sigma_k^2 \quad [3.6]$$

$$= k^2 \sigma_N^2 + \langle N \rangle^2 \sigma_k^2 \quad [3.7]$$

Because the number of molecules in the probed region is a small, random sample of the large population in solution, this number should follow Poisson statistics, where σ_N^2 is equal to its mean ($\sigma_N^2 = \langle N \rangle$). The variance in k can arise from several sources, including the variation in excitation intensity across the beam profile; this variation should be small in the present experiments because the diameter of the probing region is less than 2% of the diameter of illumination profile and is centered near its the peak. A more significant source of variation in k is fluctuations in the fluorescence yield of probe molecules, which can depend on orientation,[57] interactions with their local environment,[58,59] or excited-state photoblinking.[60]

Substituting the mean number of molecules for their variance in Equation 3.6 shows that the dependence of the fluorescence variance should exhibit a linear and quadratic dependence on the average number of molecules:

$$\sigma_F^2 = k^2 \langle N \rangle + \sigma_k^2 \langle N \rangle^2 \quad [3.8]$$

This relationship can be converted to a dependence on the average fluorescence by substituting Equation 3.4 into Equation 3.8, which shows that the variance in the fluorescence signal varies linearly and quadratically with average fluorescence signal:

$$\sigma_F^2 = k\langle F\rangle + (\sigma_k^2/k^2)\langle F\rangle^2 \qquad [3.9]$$

To quantify the number of molecules from the fluctuations in the fluorescence, one can plot the dependence of σ_F^2 on $\langle F\rangle$ to determine k from the fit of the results to Equation 3.9. In the present work, the total fluorescence detected is easily varied by controlling the size of the active area on the CCD camera, which in turn increases the total number of molecules contributing to the measured fluorescence. Plots of σ_F^2 versus $\langle F\rangle$, for DiI on both the C_{18}- and C_1-surfaces, are shown in Figure 3.7a, and both sets of data are fit to Equation 3.9 with both a linear and quadratic dependence on $\langle F\rangle$. The fitted values of the sensitivity factor are k = 0.60 (±0.07) and 0.13 (±0.01) photoelectrons molecule^{-1} frame^{-1} for the C_{18} and C_1 surfaces, respectively, which likely reflects the more dispersed intensity of faster moving molecules on the C_1 surface (Figure 3.5). The relative standard deviations of the sensitivity factor determined from the curvature of the data in Figure 3.7a are σ_k/k = 0.38(±0.08) for the C_{18} surface and 0.37(±0.02) for the C_1 surface; the results show a comparable dispersion of emission yields on the two surfaces.

Having determined k from the fits of σ_F^2 versus $\langle F\rangle$ in Figure 3.7a, the number of molecules within the sampled region can then be determined from the measured fluorescence, $\langle F\rangle$, where $\langle N\rangle = \langle F\rangle/k$. The numbers of molecules thus determined are plotted in Figure 3.7b versus the area of the probing region, and the data are linear with no intercept. The linearity of the measured surface populations with increasing probed

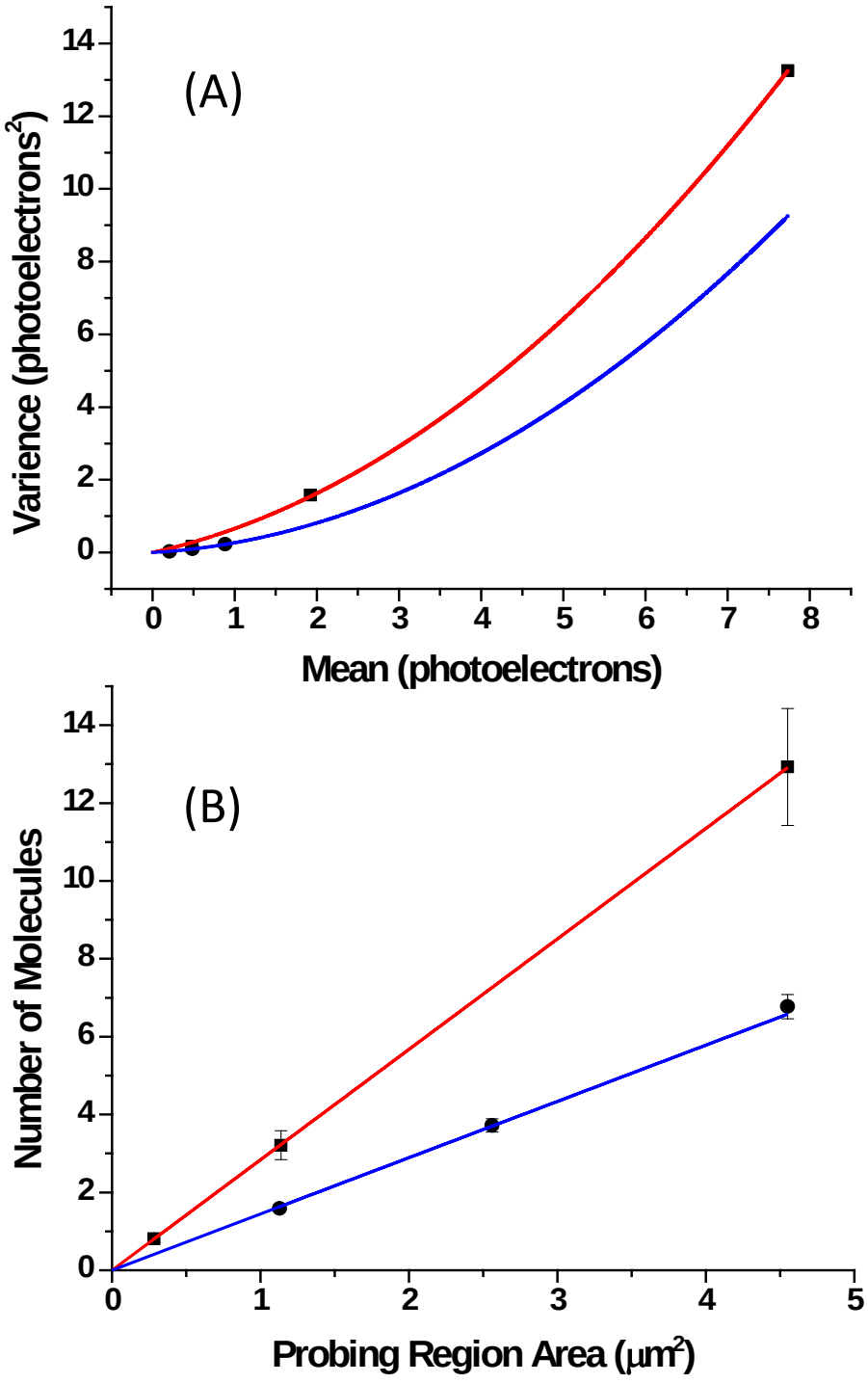

Figure 3.7. Determination of the photon count rate, *k*, and the DiI surface concentration. (A) Plots of variance in fluorescence versus mean fluorescence signal for varying probing region sizes fit to Equation 3.9, for DiI diffusion on C_{18} (squares, red line) and C_1 (circles, blue line). (B) Number of molecules versus area of probing region, with linear fits for the two surfaces.

area supports a quantitative interpretation of the results. The resulting surface populations at equilibrium with the 20 pM solution of DiI are 2.84 (±0.01) x 10^8 molecules/cm^2 and 1.45 (±0.03) x 10^8 molecules/cm^2 on the C_{18} and C_1 surfaces, respectively. These results reveal a two-fold greater affinity of the hydrophobic tails of the DiI solute for association with the long-chain C_{18} surface.

The above approach to determining the relationship between the fluorescence variance and its mean in order to quantify the number of molecules in a sample separates fluctuations arising from the number of molecules being observed from the variations in the fluorescence yield. This approach differs from the usual scaling of autocorrelation data, which are customarily normalized by subtracting the squared mean of the fluorescence, $\langle F\rangle^2$ and dividing the difference by the squared mean, $\langle F\rangle^2$. This ideally results in the scaled amplitude being equal to the inverse of the number of molecules in the probed region.[3] This approach could be correct if the fluorescence efficiency noise, σ_k^2/k^2, is negligible so that Equation 3.9 exhibits a linear relationship between the fluorescence variance and its mean: $\sigma_F^2 = k\langle F\rangle$. Thus $\sigma_F^2/\langle F\rangle^2 = k/\langle F\rangle = 1/\langle N\rangle$, and the τ = 0 point of the traditionally normalized autocorrelation function[3] $\left(\langle F(t)F(t+\tau)\rangle - \langle F\rangle^2\right)/\langle F\rangle^2\right)$ is indeed equal to $1/\langle N\rangle$. As can be seen in the significant nonlinearity in the dependence of the fluorescence variance on its mean in Figure 3.7a, however, the assumptions made in the traditional scaling of autocorrelation data clearly do not hold, even when the relative standard deviation of the fluorescence efficiency is as small as 37%. If this variance in the fluorescence yield is neglected, the number of molecules reported by traditional scaling of the autocorrelation would result in a significant overestimate of the number of molecules being samples.

3.3.6 Comparison of interfacial dynamics at C_{18} and C_1 surfaces

The results of this study show significant differences in DiI surface affinities and diffusion rates on C_{18}- and C_1-modified surfaces. First, the surface diffusion coefficient of DiI on the C_{18} surface is 4-times slower than on the C_1 surface, which is consistent with the alkyl-chains on the dye having greater contact[23] and possible entanglement with the C_{18} chains. This conclusion is also supported by the observed 14-fold slower desorption rate of DiI from the C_{18} surface, indicating stronger interactions of the dye with the long-chain surface ligands. Despite the much slower desorption rate, the surface population of DiI on the C_{18} surface was only two-times greater than on the C_1 surface, which implies that the adsorption rate of DiI to the C_1 surface must be faster than its adsorption to the C_{18} surface.

The adsorption rate can be determined from the product of adsorption equilibrium constant and desorption rate, where $k_{ads} = K_{ads}\, k_{des}$. K_{ads} is obtained from the ratio of the DiI surface concentration (see above) to its solution concentration, where $K_{ads} = \Gamma_{DiI}/[\text{DiI}]$ = 2.36 (±0.01) x 10^{-2} cm and 1.20 (±0.02) x 10^{-2} cm for the C_{18} and C_1 surfaces, respectively. The adsorption rate constants, $k_{ads} = K_{ads}\, k_{des}$ = 0.13 (±0.01) cm/s and 0.91 (±0.07) cm/s for the C_{18} and C_1 surfaces, respectively, indeed show that the adsorption of DiI is *seven-times faster* onto the C_1 surface than onto C_{18}. These results can be compared to the diffusion-limited or surface-collision rate, estimated by Fick's law[61] as the flux of molecules diffusing through a unit area to the surface at a given concentration, $v = J/[\text{DiI}] = D(d[\text{DiI}]/dx)/[\text{DiI}]$. The diffusion coefficient of DiI in solution was estimated from the Stokes–Einstein equation and van der Waals radius of DiI[47,48] (see above) $D \sim 4 \times 10^{-6}\text{cm}^2/\text{s}$. The concentration gradient ($(d[\text{DiI}]/dx$) is given by

the bulk concentration divided by the encounter distance,[62] estimated as twice the radius of DiI, $2r \sim 1.4$nm.[48] This diffusion-controlled surface-collision rate, v ~ 28 cm/s, can be divided into the observed adsorption rates to predict the adsorption efficiencies of DiI collisions with the C_{18} and C_1 surfaces, 0.0045 and 0.032, and the corresponding free-energy barriers to adsorption: $\Delta G^{\neq} = -\mathrm{RT}ln(k_{ads}/\mathrm{v}) = 13.4\ (\pm 0.3)$ kJ/mol and 8.5 (±0.2) kJ/mol, respectively.

Therefore, while adsorption of DiI to C_{18} leads to stronger surface interactions (slower desorption rates and slower diffusion), the C_{18} surface exhibits a much larger barrier to DiI surface association. This barrier may arise from the solvophobic collapse of the surface alkyl chains in the polar solvent[63] requiring the surface alkyl chains to expand in order for DiI alkyl tails to intercalate. Intercalation of DiI is not possible on the C_1 surface, which would reduce the barrier to adsorption and thus lead to more rapid surface-association and interfacial diffusion. The intercalation of DiI into the C_{18} chains is consistent with the much slower desorption of DiI from the C_{18} surface and with its slower interfacial diffusion, hindered by interactions with surface alkyl chains.

In summary, camera-based imaging-FCS technique was adapted to the analysis of rapid interfacial dynamics at model reversed-phase chromatographic surfaces. Limiting the data collection to a small number of CCD pixels allows imaging with 1-ms time resolution, while digital control of the probed region location is useful for locating, counting, and then avoiding strong adsorption sites when measuring diffusion coefficients of moving molecules. Varying the area of the probed region provides a means of distinguishing the autocorrelation decay due to surface diffusion from other sources of fluorescence fluctuations, such as those arising from desorption kinetics.

Varying the probed area is also useful in determining the photon rate per molecule and its relative standard deviation, which in turn allows accurate reporting of molecular surface densities, especially in circumstances where there are significant molecule-to-molecule variations in emission rates. The combination of these data provides insight into the differences in the interfacial molecular dynamics at short-chain (C_1) versus long-chain (C_{18}) alkyl-silane modified surfaces. Future applications could be directed toward characterizing the dependence of interfacial diffusion and adsorption/desorption rates on alkyl-chain length and functionality and to compare the results to data taken from within actual chromatographic media.[30]

3.4 Acknowledgements

This research was supported in part by the U.S. Department of Energy under Grant DE-FG03-93ER14333. Additional support from Agilent Technologies in the form of a University Relations Grant is gratefully acknowledged.

3.5 References

(1) Axelrod, D. *J. Cell Biol.* **1981**, *89*, 141.

(2) Thompson, N. L.; Burghardt, T. P.; Axelrod, D. *Biophys. J.* **1981**, *33*, 435.

(3) Elson, E. L.; Magde, D. *Biopolymers* **1974**, *13*, 1.

(4) *Fluorescence Correlation Spectroscopy: Theory and Applications*; Rigler, R.; Elson, E. S., Eds.; Springer: Berlin, 2001.

(5) Haustein, E.; Schwille, P. *Annu. Rev. Biophys. Biomol. Struct.* **2007**, *36*, 151.

(6) Thompson, N. L.; Axelrod, D. *Biophys. J.* **1983**, *43*, 103.

(7) Hansen, R. L.; Harris, J. M. *Anal. Chem.* **1998**, *70*, 4247.

(8) Hansen, R. L.; Harris, J. M. *Anal. Chem.* **1998**, *70*, 2565.

(9) Elson, E. L.; Schlessinger, J.; Koppel, D. E.; Axelrod, D.; Webb, W. W. *Prog. Clin. Biol. Res.* **1976**, *9*, 137.

(10) Wirth, M. J.; Swinton, D. J.; Ludes, M. D. *J. Phys. Chem. B* **2003**, *107*, 6258.

(11) Swinton, D. J.; Wirth, M. J. *Anal. Chem.* **2000**, *72*, 3725.

(12) Wirth, M. J.; Legg, M. A. *Annu. Rev. Phys. Chem.* **2007**, *58*, 489.

(13) Wirth, M. J.; Swinton, D. J. *Anal. Chem.* **1998**, *70*, 5264.

(14) Kisley, L.; Chen, J.; Mansur, A. P.; Shuang, B.; Kourentzi, K.; Poongavanam, M.-V.; Chen, W.-H.; Dhamane, S.; Willson, R. C.; Landes, C. F. *Proc. Natl. Acad. Sci. U.S.A.* **2014**.

(15) Widengren, J.; Mets, Ü.; Rigler, R. *Chem. Phys.* **1999**, *250*, 171.

(16) Hansen, R. L.; Zhu, X. R.; Harris, J. M. *Anal. Chem.* **1998**, *70*, 1281.

(17) Wawrezinieck, L.; Rigneault, H.; Marguet, D.; Lenne, P.-F. *Biophys. J.* **2005**, *89*, 4029.

(18) Barak, L.; Webb, W. *J. Cell Biol.* **1982**, *95*, 846.

(19) Ghosh, R. N.; Webb, W. W. *Biophys. J.* **1994**, *66*, 1301.

(20) Saxton, M. J.; Jacobson, K. *Annu. Rev. Biophys. Biomol. Struct.* **1997**, *26*, 373.

(21) Knight, J. D.; Michael G. Lerner; Joan G. Marcano-Velázquez; Richard W. Pastor; Falke, J. J. *Biophys. J.* **2010**, *99*, 2879.

(22) Honciuc, A.; Harant, A. W.; Schwartz, D. K. *Langmuir* **2008**, *24*, 6562.

(23) Honciuc, A.; Schwartz, D. K. *J. Am. Chem. Soc.* **2009**, *131*, 5973.

(24) Elliott, L. C. C.; Barhoum, M.; Harris, J. M.; Bohn, P. W. *Langmuir* **2011**, *27*, 11037.

(25) Elliott, L. C. C.; Barhoum, M.; Harris, J. M.; Bohn, P. W. *PCCP* **2011**, *13*, 4326.

(26) McCain, K. S.; Hanley, D. C.; Harris, J. M. *Anal. Chem.* **2003**, *75*, 4351.

(27) Fu, Y.; Ye, F.; Sanders, W. G.; Collinson, M. M.; Higgins, D. A. *J. Phys. Chem. B* **2006**, *110*, 9164.

(28) Ye, F.; Higgins, D. A.; Collinson, M. M. *J. Phys. Chem. C* **2007**, *111*, 6772.

(29) Ye, F.; Collinson, M. M.; Higgins, D. A. *PCCP* **2009**, *11*, 66.

(30) Cooper, J. T.; Peterson, E. M.; Harris, J. M. *Anal. Chem.* **2013**, *85*, 9363.

(31) Thompson, R. E.; Larson, D. R.; Webb, W. W. *Biophys. J.* **2002**, *82*, 2775.

(32) Michalet, X.; Berglund, A. J. *Phys. Rev. E* **2012**, *85*, 061916.

(33) Michalet, X. *Phys. Rev. E* **2010**, *82*, 041914.

(34) Ritter, J. G.; Veith, R.; Siebrasse, J.-P.; Kubitscheck, U. *Opt. Express* **2008**, *16*, 7142.

(35) Ritter, J. G.; Veith, R.; Veenendaal, A.; Siebrasse, J. P.; Kubitscheck, U. *PLoS ONE* **2010**, *5*, e11639.

(36) Vermot, J.; Fraser, S. E.; Liebling, M. *HFSP .l* **2008**, *2*, 143.

(37) Burkhardt, M.; Schwille, P. *Opt. Express* **2006**, *14*, 5013.

(38) Kannan, B.; Har, J. Y.; Liu, P.; Maruyama, I.; Ding, J. L.; Wohland, T. *Anal. Chem.* **2006**, *78*, 3444.

(39) Kannan, B.; Guo, L.; Sudhaharan, T.; Ahmed, S.; Maruyama, I.; Wohland, T. *Anal. Chem.* **2007**, *79*, 4463.

(40) Guo, L.; Har, J. Y.; Sankaran, J.; Hong, Y.; Kannan, B.; Wohland, T. *Chem. Phys. Chem.* **2008**, *9*, 721.

(41) Boening, D.; Groemer, T. W.; Klingauf, J. *Opt. Express* **2010**, *18*, 13516.

(42) Sankaran, J.; Bag, N.; Kraut, R. S.; Wohland, T. *Anal. Chem.* **2013**, *85*, 3948.

(43) Maoz, R.; Sagiv, J. *J. Colloid Interface Sci.* **1984**, *100*, 465.

(44) Fairbank, R. W. P.; Xiang, Y.; Wirth, M. J. *Anal. Chem.* **1995**, *67*, 3879.

(45) Berg, H. C. *Random Walks in Biology*; Princeton University Press: Princeton, 1993.

(46) Koppel, D. E. *Phys. Rev. A* **1974**, *10*, 1938.

(47) Hashimoto, F.; Tsukahara, S.; Watarai, H. *Langmuir* **2003**, *19*, 4197.

(48) Barton, A. F. M. *CRC Handbook of Solubility Parameters and Other Cohesion Parameters,* 2nd Ed.; CRC Press: Boca Raton, FL, 1991.

(49) Bernasconi, C. F. *Relaxation Kinetics*; Academic Press, Inc.: New York, 1976.

(50) Nawrocki, J. *J. Chromatogr. A* **1997**, *779*, 29.

(51) Rogers, S. D.; Dorsey, J. G. *J. Chromatogr. A* **2000**, *892*, 57.

(52) Köhler, J.; Chase, D. B.; Farlee, R. D.; Vega, A. J.; Kirkland, J. J. *J. Chromatogr. A* **1986**, *352*, 275.

(53) Cox, G. B. *J. Chromatogr. A* **1993**, *656*, 353.

(54) Wirth, M. J.; Ludes, M. D.; Swinton, D. J. *Anal. Chem.* **1999**, *71*, 3911.

(55) Ludes, M. D.; Wirth, M. J. *Anal. Chem.* **2001**, *74*, 386.

(56) Zhong, Z.; Lowry, M.; Wang, G.; Geng, L. *Anal. Chem.* **2005**, *77*, 2303.

(57) Tokimoto, T.; Bethea, T. R. C.; Zhou, M.; Ghosh, I.; Wirth, M. J. *Appl. Spectrosc.* **2007**, *61*, 130.

(58) Gao, F.; Mei, E.; Lim, M.; Hochstrasser, R. M. *J. Am. Chem. Soc.* **2006**, *128*, 4814.

(59) Issac, A.; Borczyskowski, C. v.; Cichos, F. *Phys. Rev. B* **2005**, *71*, 161302.

(60) Yip, W.-T.; Hu, D.; Yu, J.; Bout, D. A. V.; Barbara, P. F. *J. Phys. Chem. A* **1998**, *102*, 7564.

(61) Bard, A. J.; Faulkner, L. R. *Electrochemical Methods: Fundamentals and Applications*; 2 ed.; Wiley: New York, 2001.

(62) Rice, S. A. In *Comprehensive Chemical Kinetics*; Bramford, C. H., Tipper, C. F. H., Compton, R. G., Eds.; Elsevier: Amsterdam, 1985; Vol. 25.

(63) Löchmuller, C. H.; Wilder, D. R. *J. Chromatogr. Sci.* **1979**, *17*, 574.

3.6 Supporting Information

3.6.1 Total-internal-reflection fluorescence microscopy

Imaging of DiI molecules was accomplished using an Eclipse TE200 inverted microscope (Nikon Corp.) with a 60x 1.49 N.A. Apo-TIRF oil immersion objective lens, with a working distance of 0.12 mm, in a total internal reflection illumination geometry,

as depicted in Figure 3.8. Total internal reflection was achieved by translation of the excitation beam entering the objective lens off the optical axis until the emerging beam was incident at an angle greater than the critical angle for the glass/aqueous solution interface. Samples were illuminated using the 514.5 nm line from a Lexel Model 95 argon ion laser. The laser light was coupled into a polarization maintaining single mode optical fiber (Thorlabs) using an aspheric fiber-port collimator/coupler (Thorlabs). Light emerging from the fiber was collimated using planoconvex achromatic lens and passed through a 514 nm narrow width band-pass filter. The filtered excitation light intensity was measured to be 20 mW prior to being refocused into the back focal plane of the microscope objective. Fluorescence emission from molecules at the interface was collected back through the same objective lens and passed through a filter cube containing 532 nm single-edge dichroic beamsplitter and a 585 nm bandpass emission filter. The filtered fluorescence emission was imaged onto an Andor iXon^{EM}+ 897 EMCCD camera.

3.6.2 Imaging cycle time versus number of rows acquired

The imaging acquisition cycle time is the exposure time of the camera plus the pixel read out time. Horizontal rows of pixels in the image are sequentially shifted downward on the CCD array into a readout register; thus the read out time and the total kinetic cycle time roughly scales with the number of rows in the image, as shown in Figure 3.9. This allowed for a small subset of pixels (2–8 rows) to be imaged at a fast time resolution (~1 ms).

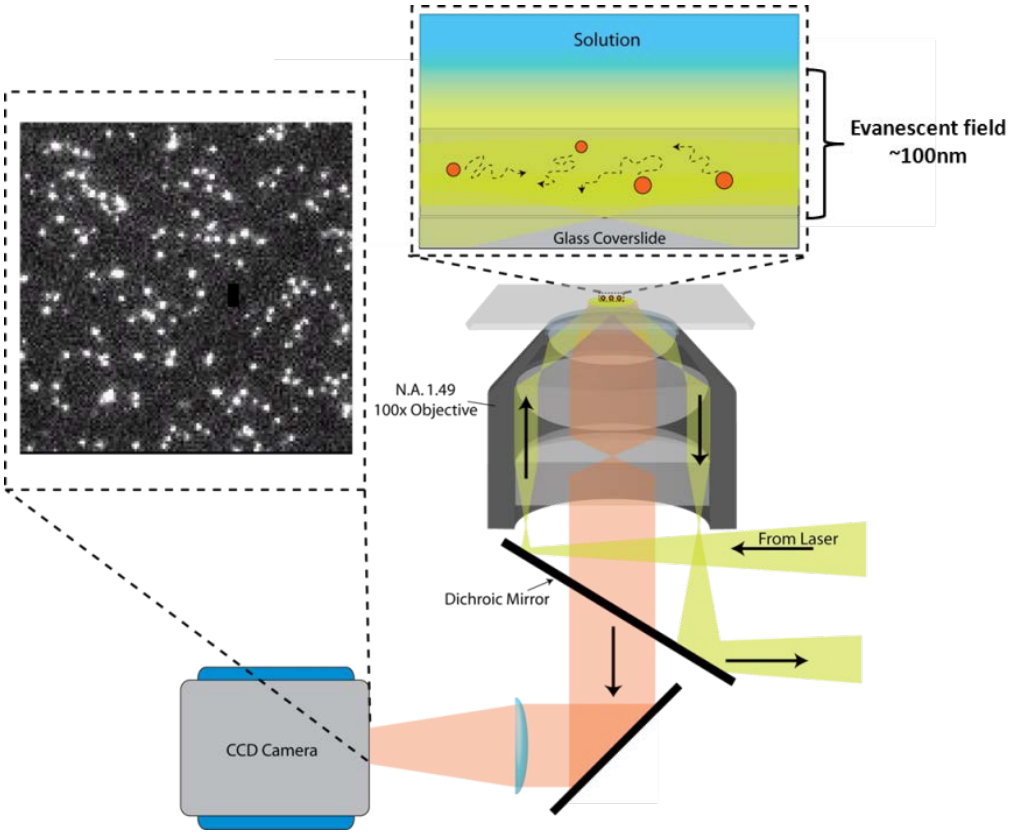

Figure 3.8. Total-internal reflection fluorescence microscope for imaging-fluorescence-correlation spectroscopy experiments.

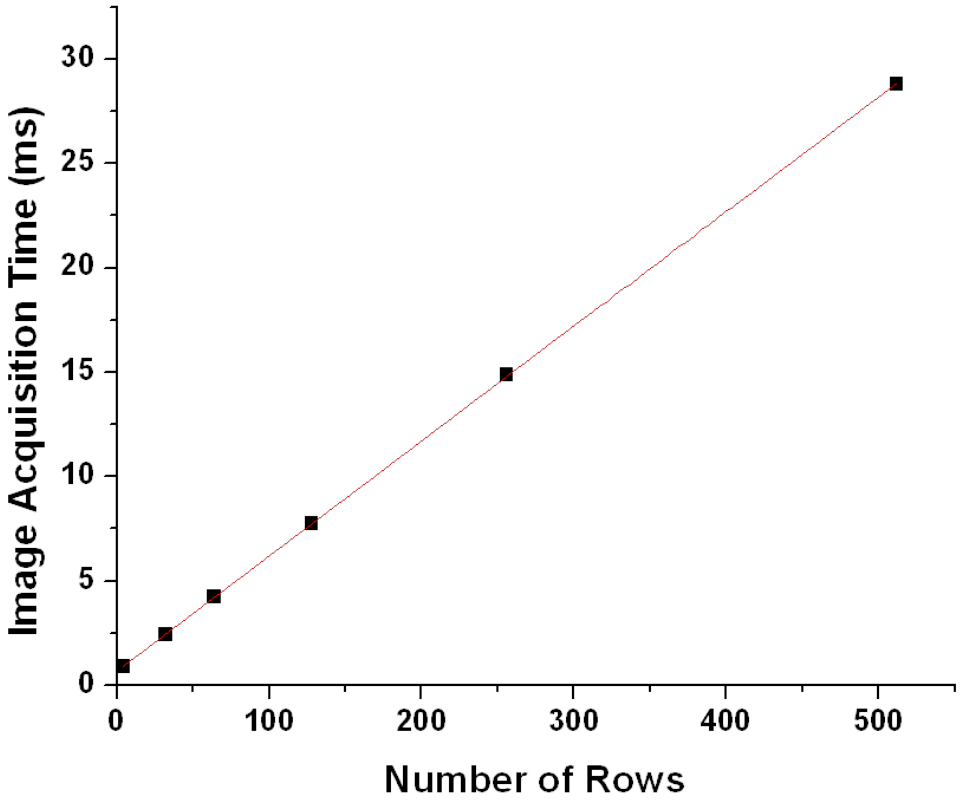

Figure 3.9. Image acquisition cycle time versus the number of rows being read from the CCD camera.

3.6.3 Photobleaching lifetime of DiI

To determine the photobleaching lifetime of DiI, a large surface population of DiI was deposited on the C_{18} surface from a 0.5-nM solution in 90% methanol, and the solution was then switched to a 10%-methanol solution having no DiI, producing a stable population of DiI on the C_{18} surface. Photobleaching of this population was measured in a 64-by-64 pixel region by the change in fluorescence intensity over time, using the same laser power (20 mW) as in FCS measurements to excite the sample. The results show a 2-exponential survival function with 82% of the population exhibiting a 6.0-s lifetime, and 18% of the population surviving with 41-s lifetime (Figure 3.10). The population-weighted average photobleaching lifetime was 12.5 ± 0.1 s.

3.6.4 Relaxation from small fluctuations of an adsorption equilibrium

The relaxation of small fluctuations of a surface concentration of an adsorbed species in equilibrium with an overlaying solution population is derived in similar fashion to that of a homogenous relaxation kinetics case,[49] with the exception that we must account for the change in dimensionality associated with adsorption from solution. For the present work, we assume a surface-association reaction:

$$A \underset{k_2}{\overset{k_1}{\leftrightarrow}} B \qquad [3.10]$$

where A is the solution concentration of molecules in cm^{-3}, B is surface molecular concentration in cm^{-2}, and k_1 and k_2 are the rate constants for the adsorption and desorption reactions, respectively, having units of $cm^{-1}\ s^{-1}$ and s^{-1}, respectively. For this scenario, the rate of change of the surface concentration B can be expressed by the following rate equation:

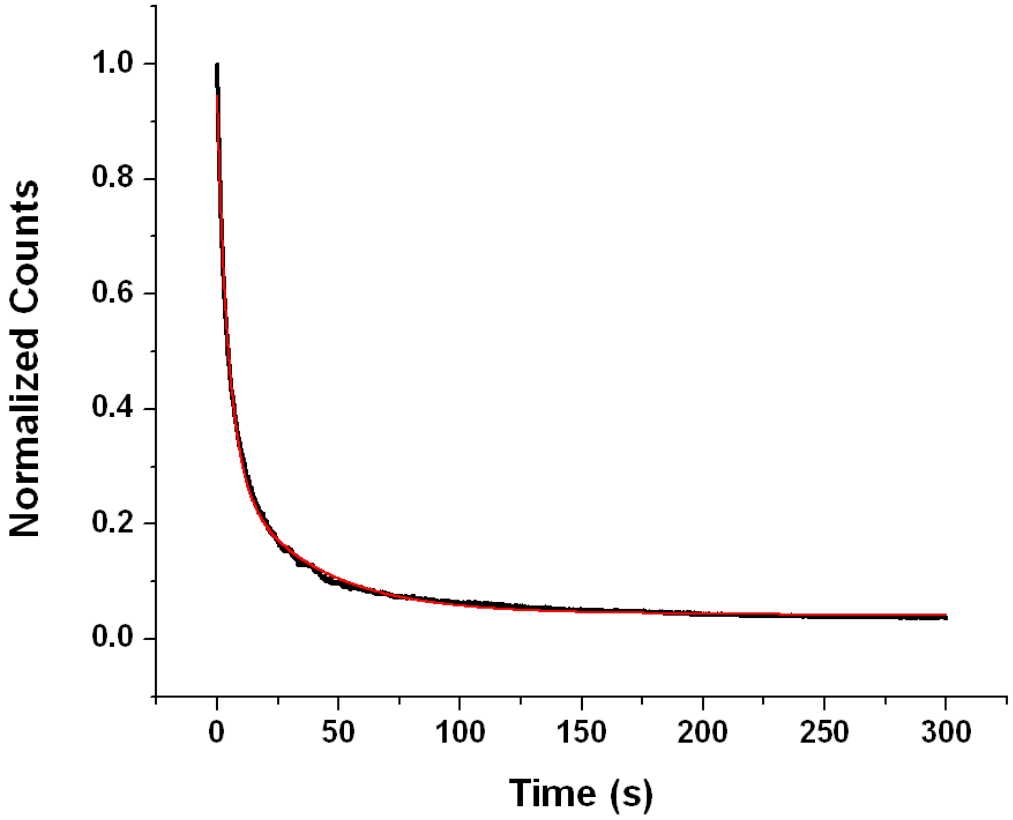

Figure 3.10. Photobleaching of fixed population of DiI on a C_{18} surface measured as a decay of fluorescence intensity (black line). Excitation power was matched to the FCS measurements (20 mW). The red line is a fit to a 2-exponential decay.

$$\frac{dB}{dt} = k_1 A - k_2 B \qquad [3.11]$$

A small perturbation from equilibrium can be expressed in terms of changes in the populations of A and B.

$$A = A_{eq} + \delta A \qquad [3.12]$$

$$B = B_{eq} + \delta B \qquad [3.13]$$

where the deviations, δA and δB, are of opposite sign. Substituting Equations 3.12 and 3.13 into Equation 3.11,

$$\frac{d(B_{eq}+\delta B)}{dt} = k_1\left(A_{eq} + \delta A\right) - k_2(B_{eq} + \delta B) \qquad [3.14]$$

or

$$\frac{dB_{eq}}{dt} + \frac{d(\delta B)}{dt} = k_1 A_{eq} + k_1 \delta A - k_2 B_{eq} - k_2 \delta B \qquad [3.15]$$

The rate of change in the surface concentration at equilibrium is zero, given by:

$$\frac{dB_{eq}}{dt} = k_1 A_{eq} - k_2 B_{eq} = 0 \qquad [3.16]$$

which can be substituted into Equation 3.15 indicating that the relaxation of the fluctuation depends on the sum of the two rates, where recall that δA and δB, are of opposite sign:

$$\frac{d(\delta B)}{dt} = k_1 \delta A - k_2 \delta B \qquad [3.17]$$

This result indicates that a decrease, for example, in the surface concentration relative to equilibrium, $\delta B < 0$, is relaxed by both a reduced rate of desorption from the smaller concentration of molecules leaving the surface and an elevated rate of adsorption to the surface by the higher concentration of molecules in solution, δA.

3.6.4.1 No-flow conditions. In the absence of solution flow, the rate of return to equilibrium is governed by the deviations in both the surface population, δB, and the solution concentration, δA. The number of molecules involved in a fluctuation must be conserved so that the change in solution concentration times the volume equals a change of opposite sign in the surface concentration times the corresponding surface area:

$$\delta A * Vol = -\delta B * Area \qquad [3.18]$$

For adsorption equilibria, the distance into solution that contains the same number of molecules that are adsorbed to the surface (for the same unit area) is given by the adsorption equilibrium constant,[64]

$$K_{ads} = B_{eq}/A_{eq} = k_1/k_2 \qquad [3.19]$$

which provides the ratio of the volume to surface area, within which the number of molecules is conserved at equilibrium: $Vol/Area = K_{ads}$ and substitution into Equation 3.18 gives

$$\delta A = -\delta B / K_{ads} \qquad [3.20]$$

Substituting Equation 3.18 followed by Equation 3.19 into Equation 3.17 yields

$$\frac{d(\delta B)}{dt} = \left(-k_1/K_{ads}-k_2\right)\delta B = -2\ k_2\delta B \qquad [3.21]$$

Integrating this differential equation shows that in the absence of flow, a small fluctuation in an adsorbate concentration from equilibrium relaxes from the initial fluctuation, δB_0, by a first-order exponential decay:

$$\delta B = \delta B_0\left(e^{-k_0 t}\right) \qquad [3.22]$$

where the relaxation rate is equal to twice the desorption rate, $k_0 = 2\ k_2$.

3.6.4.2 Fast-flow conditions. In the present experiments, the solution is flowing over the surface, which transfers the concentration fluctuation in solution, δA, beyond the observation area in a time that is less than 5% of the measured relaxation time for the change in the surface population, δB. Note, the solution flow rate that for the volume containing the correlated concentration fluctuation, δA, is estimated from a parabolic flow profile averaged through a distance above the surface given by the equilibrium constant (see above).[64] Thus, δA is driven quickly to zero, and A is restored to A_{eq} by flow so that the observed relaxation of the surface concentration to equilibrium depends only on the desorption rate:

$$\frac{d(\delta B)}{dt} = -k_2\delta B \qquad [3.23]$$

Integrating the differential equation shows that a fluctuation in an adsorbate concentration from equilibrium relaxes from the initial fluctuation, δB_0, by a first-order exponential decay:

$$\delta B(t) = \delta B_0\left(e^{-k_2 t}\right) \quad [3.24]$$

where the relaxation rate is equal to desorption rate, k_2.

3.6.5 References for supporting information

(1) Bernasconi, C. F. *Relaxation Kinetics*; Academic Press, Inc.: New York, 1976.

(2) Myers, G. A.; Gacek, D. A.; Peterson, E. M.; Fox, C. B.; Harris, J. M. *J. Am. Chem. Soc.* **2012**, *134*, 19652.

CHAPTER 4

FLUORESCENCE-CORRELATION SPECTROSCOPY STUDY OF MOLECULAR TRANSPORT WITHIN REVERSED-PHASE CHROMATOGRAPHIC PARTICLES COMPARED TO PLANAR MODEL SURFACES

4.1 Introduction

The dynamics of molecules at chemical interfaces play a fundamental role in governing the chemistry relied upon by numerous applications including heterogeneous catalysis, chemical sensors, molecular recognition at biological interfaces, and chemical separation technologies. Many of these applications employ high surface area materials so that *interfacial* phenomena dominate the chemistry that occur in these applications and the high surface area provides the capacity for dealing with large numbers of molecules. In chromatographic separations, for example, molecules are retained on the surface of porous supports that exhibit specific surface areas between 10^2 and 10^3 m^2/g and a surface area to volume ratio of approximately 10^6 m^{-1}.[1] Analyte retention is governed by the kinetics of analyte interactions with the stationary phase at the mobile-phase/stationary-phase interface, where the retention equilibrium depends on the rates of adsorption and desorption to and from the stationary phase.[2] The efficiency of separations is degraded by band spreading, which is dominated in liquid phase separations by the rates of molecular transport to and from the surface of particles, the majority (>99%) residing within the particle interior.[2] For highly retained species, diffusion rates of

molecules on the stationary-phase surface is a critical contributor to intraparticle diffusion rates in chromatographic media.[3]

Characterizing the transport behavior of molecules in chromatographic media has represented a measurement challenge because most of the surface area in chromatographic porous silica particles resides within the particle. Thus, most of the chemical interactions and transport processes responsible for chromatographic retention and band spreading take place inside the particles, making direct interrogation of dynamics difficult. Despite these difficulties, intraparticle transport rates have been measured using chromatographic based techniques. Techniques such as frontal analysis of breakthrough curves[4,5] and the shallow bed method[6,7] have been used to determine mass transfer rate coefficients within various types of porous chromatographic media. Guichon et al. have also studied intraparticle mass transfer kinetics, with particular attention given to the surface diffusion component, using the pulse response method combined with moment analysis.[8–10] These techniques rely on analysis of elution profile broadening to infer the contributions of surface diffusion to the total intraparticle transport occurring within the column.

Fluorescence microscopy techniques are uniquely suited to measuring interfacial kinetics, where the high quantum yield of fluorescent probes and the sensitivity of detectors have pushed detection to the single-molecule limit. These techniques have been employed in measuring adsorption-desorption kinetics and surface diffusion rates of molecules at varying reversed phase chromatographic interfaces and chromatographic solvent conditions. Fluorescence recovery after patterned photobleaching (FRAPP) has been used to measure the lateral diffusion coefficients of rubrene on an interface of n-

alkyl chains bound to a planar silica substrate under varying ligand bonding densities, chain lengths, and overlying solution conditions.[11,12] Fluorescence correlation spectroscopy combined with a total internal reflection illumination (TIR-FCS) to measure the adsorption and desorption rates of rhodamine 6G at a C_{18}-modified planar fused-silica surface under varying solvent conditions.[13,14] FCS in a confocal illumination/detection geometry has been used at an interface to measure the surface diffusion rates of 1,1'-dioctadecyl-3,3,3'3'-tetramethylindocarbocyanine perchlorate (DiI) hydrophobic fluorescent probe molecules at C_{18}-modified silica surface.[15,16] These studies represent experiments done on planar model n-alkylsilane modified silica substrates, which are intended to mimic the interface existing within porous reversed-phase chromatographic silica. While planar silica substrates may produce a reasonable model for the interface chemistry of porous reversed-phase chromatographic particles, planar substrates provide a much simpler geometry for molecular transport compared to porous silica particles, which may influence the relationship between dynamic measurements made on planar analogs versus porous particles. Porous silica structures have been engineered into a planar geometry with thin films deposited as sol-gel structures and studied using fluorescence-correlation spectroscopy and single-molecule imaging microscopy to investigate the influence of pore structure and chemical interactions on molecular transport within the porous film.[17–21] However, the pore structure and surface chemistry silica sol-gel films[22] differ significantly from porous silica particles used as chromatographic media because the latter are usually sintered at high temperature to collapse micropores and then subjected to hydrothermal treatment[1,23] to increase their average pore diameter, tighten the pore-size distribution, and hydrolyze surface siloxane

bonds.

Recently, progress has been made in using fluorescence microscopy techniques to measure molecular dynamics within actual chromatographic media. Scanning confocal microscopy combined with FCS has been to measure the time-scale of strong adsorption events within C_{18}-silica gel under RPLC conditions.[24] More recently, single-molecule fluorescence imaging was used to measure analyte residence times, diffusion coefficients, and heterogeneous transport characteristics within commercially available RPLC media.[25] As the body of literature concerning fluorescence microcopy studies of RPLC interfaces now includes both studies done at planar analogs of chromatographic media and those done within porous chromatographic particles, comparison of results for the two systems requires an understanding of what effects the differing transport geometries may have on measured transport rates.

In this work, we attempt to reconcile the rates of surface diffusion measured on a planar analogue of a reversed-phase chromatographic surface with diffusion rates of the same probe molecule measured within an authentic C_{18}-derivatized chromatographic silica particle. We employ a methodology that combines fast fluorescence imaging with fluorescence-correlation spectroscopy (imaging-FCS), where a small portion of a CCD camera chip images a small area region of the sample at a high frame rate, resulting in a fast fluorescence intensity time trace that can be autocorrelated to yield dynamic information.[26–28] The acquisition speed of this methodology is needed to measure the faster lateral diffusion rates observed on planar surfaces. The technique provides control over the probing region size and location, allowing the resolution of both transport and adsorption/desorption kinetics from an autocorrelation function.[29] Imaging-FCS is used to

measure the diffusion coefficient of the fluorescent probe 1,1'-dioctadecyl-3,3,3'3'-tetramethylindocarbocyanine perchlorate (DiI) diffusing within the porous network of a reversed-phase chromatographic silica particle and compared with the diffusion coefficients of DiI measured at a planar analog of a reversed-phase chromatographic interface consisting of a C_{18}-modified glass coverslip. Upon correcting the porous particle dynamics for the effective surface area explored by the probe molecule as it diffuses laterally in the fluorescence image, the results indicate that fundamental diffusion rates on the two surfaces on the molecular scale are very similar. The results support the use of planar substrates as models for chromatographic interfaces to gain detailed understanding of the interfacial dynamics that influence chromatographic retention behavior.

4.2 Experimental Section

4.2.1 Chemicals and materials

1,1'-dioctadecyl-3,3,3'3'-tetramethylindocarbocyanine perchlorate (DiI) fluorescent dye was purchased from Invitrogen (Carlsbad, CA). Serial dilutions of DiI were made into Omnisolv spectroscopy grade methanol (MeOH) from EMD chemicals (Darmstadt, Germany). Glass coverslips for use as substrate for derivatization were obtained from VWR International (Radnor, PA). Coverslips were cleaned via UV-Ozone cleaning for 25 min on each side. Coverslip cleanliness was verified by a water contact angle of 0˚. The coverslips were subsequently silanized using trichloro(octadecyl)silane (C_{18}) and trichloro(methyl)silane (C_1) obtained from Sigma-Aldrich Corp. (St. Louis, MO). Silanization reactions were conducted in n-heptane. Custom flow cells were constructed using luer lock adapters and tubing from Value Plastics Inc. (Fort Collins,

CO) and the silanized glass coverslips. Three micron diameter Zorbax ODS bonded chromatographic media was obtained from Agilent Technologies (Santa Clara, CA); the particles were characterized by nitrogen BET by Porous Materials (Ithaca, NY). All aqueous solutions were made using 18 MΩ water, purified using a Barnstead NANOpure II system (Boston, MA). A 10 mM ACS grade sodium chloride solution from Mallinckrodt (Phillipsburg, NJ) was used as a supporting electrolyte in all aqueous solutions.

4.2.2 Preparation of chromatographic silica particles for imaging

Approximately 20 mg of Zorbax 3-μm ODS silica was suspended in 10 mL of methanol. A 10–20 μL aliquot of this suspension was added to 10 mL of a 90/10 by volume methanol/water solution and left overnight to equilibrate the interior pore volume. A dilute suspension of chromatographic particles in a 90% MeOH/aqueous solution was pumped into a flow cell constructed over a glass coverslip and was placed on the inverted microscope stage. After several minutes the particles settled to the glass coverslip, the surface of which had been previously functionalized with a C_{18}-silane by self-assembly,[30,31] in order to help immobilized the C_{18}-particles on their surface. Hydrophobic interactions between the ODS particles and the C_{18}-modified glass coverslip fix the particles to the surface and allow for solution flow without detaching the particles from the surface. A 1.0-pM solution of DiI in 90/10 methanol/water by volume was flowed continuously through the cell containing particles at 0.25 mL/min with a syringe pump (Harvard Apparatus PHD 2000).

4.2.3 Preparation of planar model RPLC interfaces

Planar analogs of reversed-phase chromatographic materials were prepared by chemically modifying the surfaces of 22x22 mm No. 1.5 glass coverslips. C_{18}-modification was accomplished by reaction with 0.5-mM trichloro(octadecyl)silane in n-heptane for 12 h followed by an endcapping step consisting of 0.5-mM trichloro(methyl)silane reacted for 12 h. Following the silanization, coverslips were rinsed in n-heptane and dried in an oven at 120˚ C for 1 hour to stimulate crosslinking polymerization between adjacent silanes. Dried coverslips were then rinsed with copious amounts of dichloromethane and methanol and stored in methanol until use. The degree of hydrophobic modification was qualitatively characterized by measurement of the water contact angle using the sessile drop method measured with a goniometer. Contact angles for C_{18}/C_1 dervatized coverslips used in experiments fell between 110˚ and 112˚, indicating a high silane surface coverage. Derivatized slides were placed in a flow cell though which a 20-pM DiI solution in 90/10 MeOH/water by volume was flowed at 0.20mL/min continuously throughout each experiment.

4.2.4 Fluorescence microscopy

Fluorescence images were acquired using an Eclipse TE200 inverted microscope (Nikon Corporation) with 1.49 N.A. Apo-TIRF oil immersion objective lenses (60x and 100x, Nikon). For total-internal-reflection excitation of planar interfaces, the excitation beam was directed into a 60x objective lens and translated off the optical axis until the emerging beam was incident at an angle greater than the critical angle for the glass/aqueous solution interface. Samples were illuminated using the 514.5 nm line from a Lexel Model 95 argon ion laser. The laser light was coupled into a polarization

maintaining single-mode optical fiber (Thorlabs) using an aspheric fiberport collimator/coupler (Thorlabs). Light emerging from the fiber was collimated using a plano-convex achromatic lens and passed through a 514 nm narrow width band-pass filter. The filtered excitation light intensity was measured at ~20 mW prior to being refocused at the back focal plane of the microscope objective. Fluorescence emission from molecules at the interface was collected back through the same 60x objective and passed through a filter cube containing a 532 nm single-edge dichroic beamsplitter and a 585 nm bandpass emission filter. The filtered fluorescence emission was imaged onto an Andor iXon^{EM}+ 897 EMCCD camera. For epi-illumination of chromatographic silica particles, the same microscope setup was employed; however, the focused excitation beam was directed along the optical axis to the center of the 100x objective. This produces a collimated excitation beam into the sample, producing uniform illumination throughout the particle. The procedure for positioning the objective to center the focal plane in the center of the particle are available.[25]

4.2.5 Imaging-FCS data collection and processing

Fluorescence correlation spectroscopy is based on examining the fluorescence fluctuations of a system within a given probing region.[32] An autocorrelation analysis of the fluorescence time trace reveals the time scale at which fluorescence fluctuation is taking place by calculating the self-similarity of the fluorescence signals at varying time shift, τ (Equation. 4.1). The autocorrelation function can be fit to a model that includes parameters relating to the physical processes inducing the fluorescence fluctuations.

$$G(\tau) = \lim_{T\to\infty} \frac{1}{T} \int_{-T/2}^{T/2} F(t)F(t+\tau)dt \qquad [4.1]$$

For the case of diffusion, the autocorrelation function (ACF) can be fit to a model that relates the time dependence of the autocorrelation decay to the diffusion in two dimensions across the probe region,[32,33]

$$G(\tau) = A * \frac{1}{1+\tau/\tau_{1/2}} + B \qquad [4.2]$$

$$(1/\tau_{1/2}) = 4D_p/\omega^2 \qquad [4.3]$$

where D_p is the diffusion coefficient and ω^2 is the square of the e^{-2} radius of the probed region determined by convoluting the square-imaging region with the point-spread function.[33]

The imaging-FCS instrumentation setup and methodology have been described previously.[29] Briefly, a surface is illuminated via epi-illumination or total internal reflection, for silica particles and planar RPLC interfaces, respectively. The FCS probing region is bounded in the axial dimension by either the depth-of-field of the objective for the case of imaging silica particles or penetration depth of the evanescent field (~100 nm) in the case of total internal reflection illumination. The lateral dimension is bounded by the active area of the CCD detector, the size and location of which was selected by electronically defining the pixel ranges in the x and y dimensions. The active region of the CCD camera was limited to an 8x8 pixel region, and fluorescence intensity time traces were generated by imaging the active region at a high frame rate (917 Hz) in the case of the planar surface, and 25 Hz in the case of intraparticle measurements, and then summing the pixel intensity in each frame. A kinetic series of images of this pixel area was acquired, and the total pixel intensity in each image corresponds to a point in the fluorescence intensity time trace, with the time coordinate corresponding to the frame

number in the kinetic series multiplied by the inverse of the framing rate (Hz^{-1}). The raw fluorescence time traces were then autocorrelated using an algorithm written in the Matlab (Mathworks) where the time traces were Fourier-transformed, multiplied by their complex conjugate to generate the power spectrum and then inverse Fourier-transformed to produce an the autocorrelation function. To mitigate noise in the autocorrelation functions, the average of 10 autocorrelations was calculated for each experimental condition by coadding their power spectra and inverse Fourier-transforming the result. Background subtraction was accomplished by averaging 10 autocorrelation functions of a C_{18}/aqueous solution interface with no fluorescent dye. This gives a measure of the intensity arising from fluorescence contamination or Raman scatter. The square root of this blank autocorrelation was then subtracted from the square root of the autocorrelation functions taken under the experimental conditions, and the result was resquared.[13,34]

4.3 Results and Discussion

4.3.1 Measuring diffusion within chromatographic silica particles

While measuring diffusion at planar analogs of chromatographic materials is more convenient for spectroscopic techniques, a planar model represents a significantly different transport geometry than chromatographic media, which usually take the form of high surface area, high porosity silica gel particles. Previous work has demonstrated the ability to image and track single molecules within chromatographic silica particles at high retention conditions.[25] It has also been shown that FCS can be used to measure the adsorption kinetics of strong adsorption sites within chromatographic silica particles.[24] In the present work, imaging-FCS is used to measure diffusion of DiI within Zorbax ODS 3-μm chromatographic particles while varying the probing region size to measure the

diffusion coefficient.[29]

Kinetic image series were collected at a rate of 25 Hz at 100x magnification, and the size of the probing region was varied to be 8x8, 6x6, 4x4, and 2x2 pixels. Following convolution of the sampled area with the point-spread function (see above),[33] the values of the radii squared of the probing region correspond to ω^2 = 0.68, 0.46, 0.28, and 0.17 μm^2, respectively. The total intensities from each frame in the image series were autocorrelated, and the results were fit to Equation 4.2 and are plotted in Figure 4.1a. The diffusion coefficient was determined by plotting the decay rate of the autocorrelation, $1/\tau_{1/2}$, versus the inverse of the squared radius of the probed region, $1/\omega^2$, which produces a linear result with a zero intercept, as predicted by Equation 4.3. The observed DiI diffusion coefficient in the particle, calculated from the slope of the line, was found to be D_p = 1.8±0.04 x 10^{-9} cm^2/s. The lack of detectable intercept indicates that there was no fluorescence fluctuation that is independent of the varying probing region size, and the fluorescence fluctuations are entirely due to the diffusion of DiI through the probed region.[29]

4.3.2 Diffusion at a planar hydrophobic interface

Many of the spectroscopic based studies of molecular transport at chromatographic-like interfaces have been conducted on *planar* glass or quartz substrates that have been functionalized with an n-alkane ligand to serve as a model of the reversed-phase interactions found in porous silica particles used in chromatography.[15,16,35,36] Molecular transport rates at a planar surface should differ from those found within actual chromatographic media on a molecular scale from differences in the interface structure and on a long-range scale from differences geometry and dimensionality of diffusional

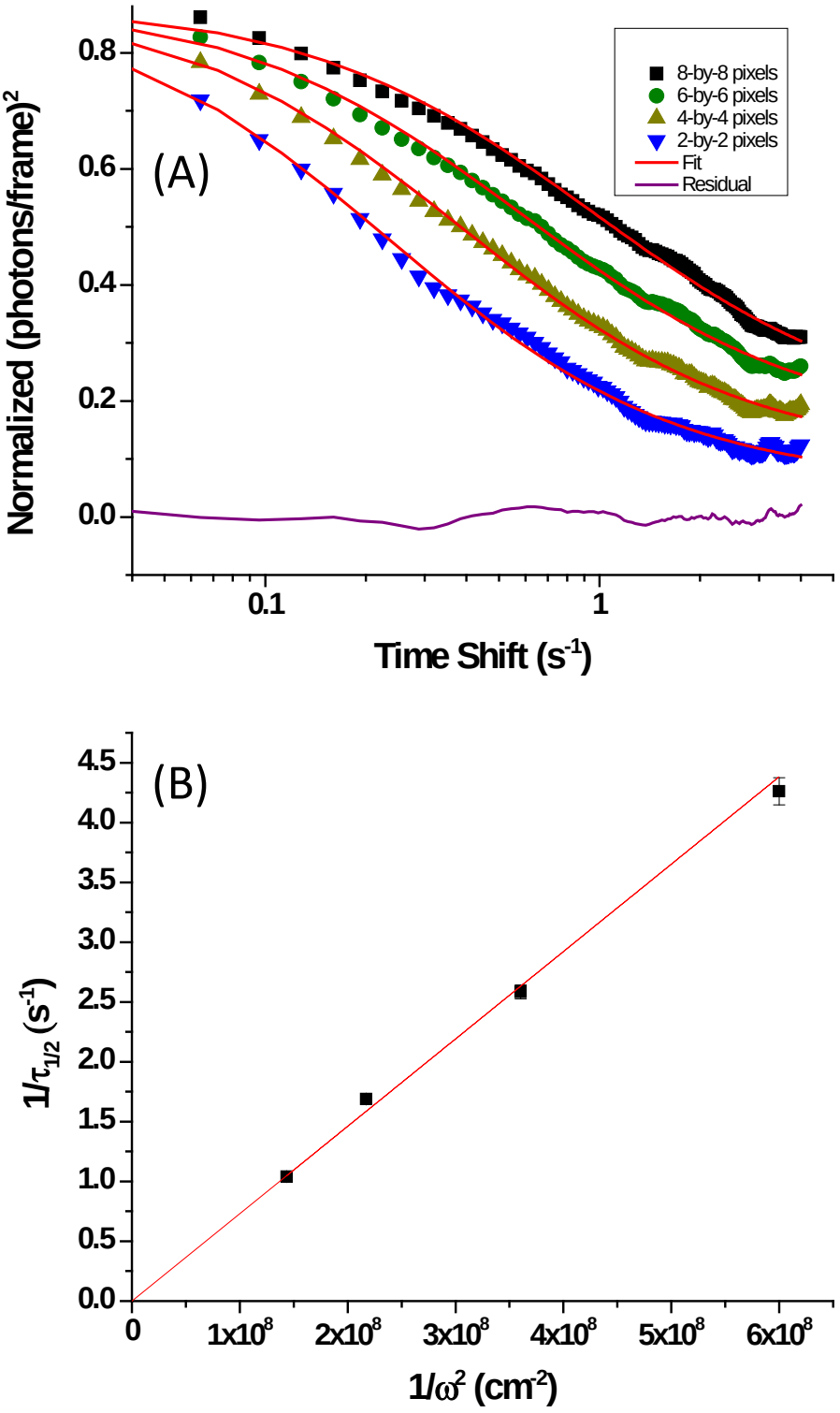

Figure 4.1. Probing region size dependent autocorrelation function analysis. (A) Normalized autocorrelation functions for molecules diffusing within a 3-μm chromatographic particle for varying probe region sizes fit to Equation 4.2. (B) A plot of $1/\tau$ versus $1/\omega^2$ fit to Equation 4.3.

trajectories. To elucidate the effect that these differences may cause in measured transport rates between these two experiments, the surface diffusion of DiI was also measured at a C_{18}-modified planar interface in equilibrium with a 20 pM DiI in 90/10 MeOH/H_2O solution and compared with that measured within reversed-phase porous silica particles.

As with the Zorbax particles, the active region of the CCD detector was limited to 8x8, 6x6, 4x4, and 2x2 pixel regions. Because the diffusional relaxation rates are much faster on the planar surface, kinetic image series were acquired ~40-times faster at a framing rate of 917 Hz. Time traces of the fluorescence intensities within each pixel region per frame were autocorrelated and fit to Equation 4.2, as above, and are plotted in Figure 4.2b. The relaxation rate versus the inverse of the squared radius of the probed region is linear (Figure 4.2b), the slope of which corresponds to a diffusion coefficient on the flat surface, D_s = 6.5(±0.1) x 10^{-8} cm^2/s, which is 36-times faster than diffusion rate measured within the porous particle. Also unlike within-particle diffusion, the dependence of the flat-surface relaxation rate on the inverse of the probed region area exhibits a nonzero intercept. The intercept corresponds to where $1/\omega^2$ in Equation 4.3 is equal to zero, an extrapolation to an infinite probed area. Thus, the intercept corresponds to a relaxation that is independent of area of the probed region and, therefore, independent of diffusion on the surface. With total-internal-reflection-excitation of a flat surface, an area-independent relaxation arises from desorption of the fluorescent probe molecule from the surface followed by diffusion away from the surface into the bulk solution.[29] The intercept in Figure 4.2b provides a measurement of the desorption rate, k_{desorb} = 5.5 (±0.4) s^{-1} or a characteristic desorption time, $\tau = 1/k_{desorb}$ ~ 182 ms.

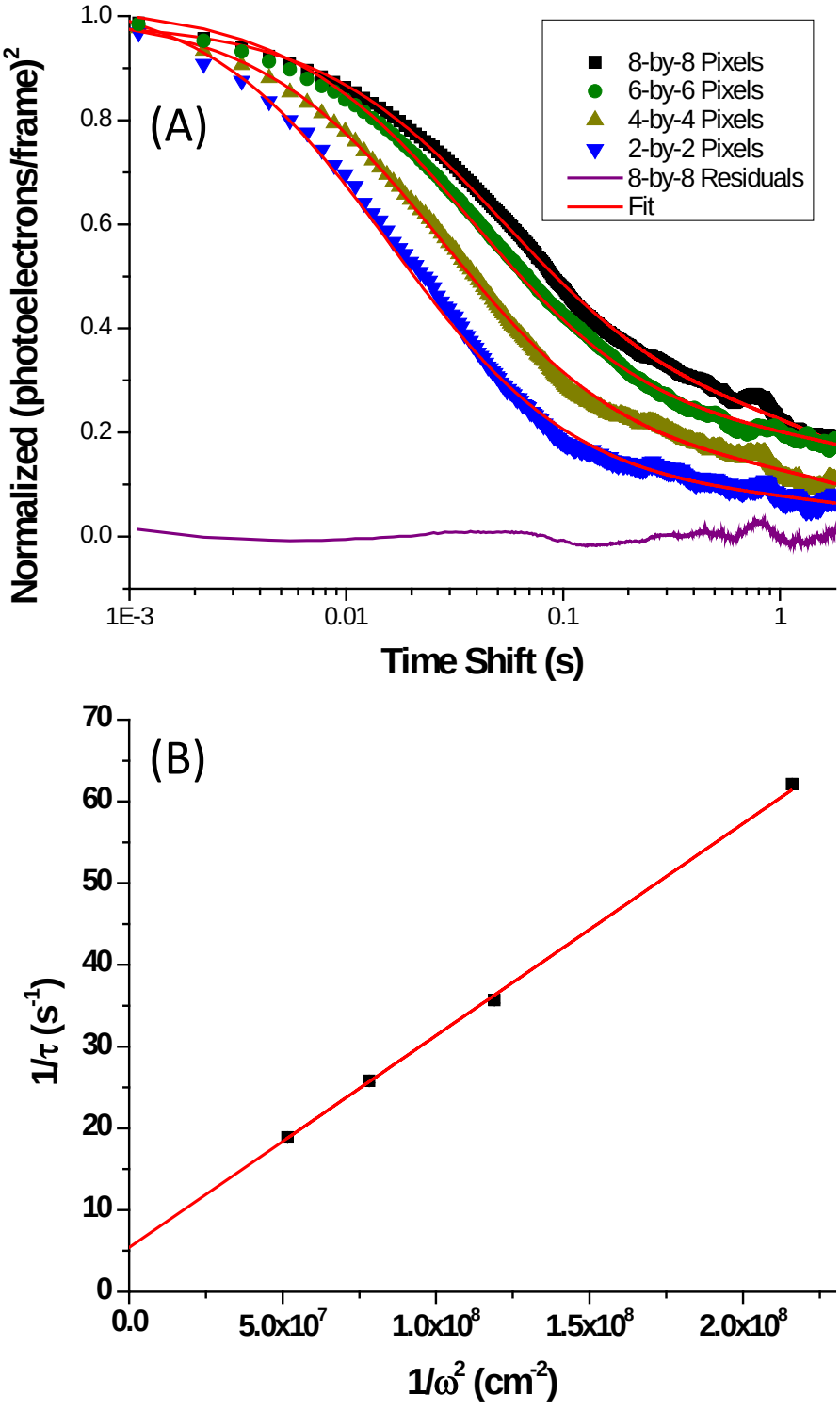

Figure 4.2. Probing region size dependent autocorrelation function analysis. (A) Normalized autocorrelation functions for molecules diffusing a planar chromatographic interface for varying probe region sizes fit to Equation 4.2. (B) A plot of $1/\tau$ versus $1/\omega^2$ fit to Equation 4.3.

Desorption of molecules from the C_{18} surface within a porous particle does not lead to diffusion into bulk solution, but rather is followed by rapid encounter and re-adsorption to nearby C_{18} surface within the small (5-nm radius) pores. From the measured adsorption rate of DiI to a C_{18} surface[29], k_{ads} = 0.13±0.01cm/s, and the average pore radius, r_p=5 nm, the average reabsorption rate for a molecule can be estimated by calculating in flux of one molecule in a unit volume to the surface area of a cylindrical pore of unit volume ($J*2/r_p = k_{ads}[1\ \text{molecule/cm}^3]*2/r_p$). One would expect readsorption to the walls of 5-nm pores within ~2 μs. Thus, unlike results acquired at a planar surface, desorption of DiI within a porous particle does not lead to a measureable relaxation because the desorbed DiI is quickly readsorbed by the surrounding C_{18} surface, where it can continue diffusing on the interior C_{18} surfaces of the porous particle.

4.3.3 Populations of molecules on planar versus porous chromatographic surfaces

The numbers of DiI molecules at the planar chromatographic surface and within the porous chromatographic particles can be determined from an analysis of the mean and variance of the fluorescence signals, which are available from the amplitudes of the autocorrelation functions[13] where $\langle F\rangle = [G(\tau=\infty)]^{1/2}$ and $\sigma_F^2 = [G(\tau=0) - G(\tau=\infty)]$. Analysis of the fluorescence variance must account for both the Poisson-distributed molecular number fluctuations and the noise due variation in fluorescence yields.[13,29] Briefly, the fluorescence intensity in the FCS probing region, F, is proportional to the number of molecules, N, $F = k\,N$, where k is the average photon count rate per molecule and depends on the illumination intensity, fluorophore absorption cross section, fluorescence quantum yield and blinking, and collection and detection efficiencies. The

variance in the fluorescence intensity can be derived via propagation of error,[13,29] where the variance in the number of molecules is given by its mean, $\sigma_N^2 = \langle N \rangle$:

$$\sigma_F^2 = k^2\langle N\rangle + \sigma_k^2\langle N\rangle^2 = k\langle F\rangle + (\sigma_k^2/k^2)\langle F\rangle^2 \qquad [5.4]$$

Thus, the fluorescence variance depends both linearly and quadratically on the average fluorescence intensity, which can be fit to determine *k* and thereby the average number of molecules being observed. Figure 4.3a shows a plot of the DiI fluorescence variance versus the fluorescence intensity as the probed area within a porous particle is varied, and the data are fit to Equation 4.4, to determine k = 213 ± 25 photons molecule^{-1} s^{-1}. This result is used to determine the number of molecules from the average fluorescence intensities, and the results are linear with the probed area, as expected (Figure 4.3b), where the slope of the line is 55.1(±0.5) molecules/μm^2.

This same analysis can be applied to the autocorrelation results for DiI on the planar C_{18} surface, and the results are shown in Figure 4.4. The sensitivity factor for observing DiI in TIRF at a planar surface is k = 569 ± 73 photons molecule^{-1} s^{-1}, which is 2.6-times greater than the sensitivity of detecting DiI within a porous C_{18} particle in epifluorescence. This is a realistic result because TIRF illumination leads to enhanced intensity at the interface,[37] by roughly three-fold in the present experiment estimated from the refractive indices of the glass substrate and aqueous solution and the excitation incident angle. A more dramatic difference between flat C_{18} surface and porous particle is the much smaller DiI population (2.84 [±0.008] molecules/μm^2) on the planar surface compared to the within-particle results (see above). Accounting for the 20-fold higher DiI solution concentration used in the planar surface experiment (well within the linear

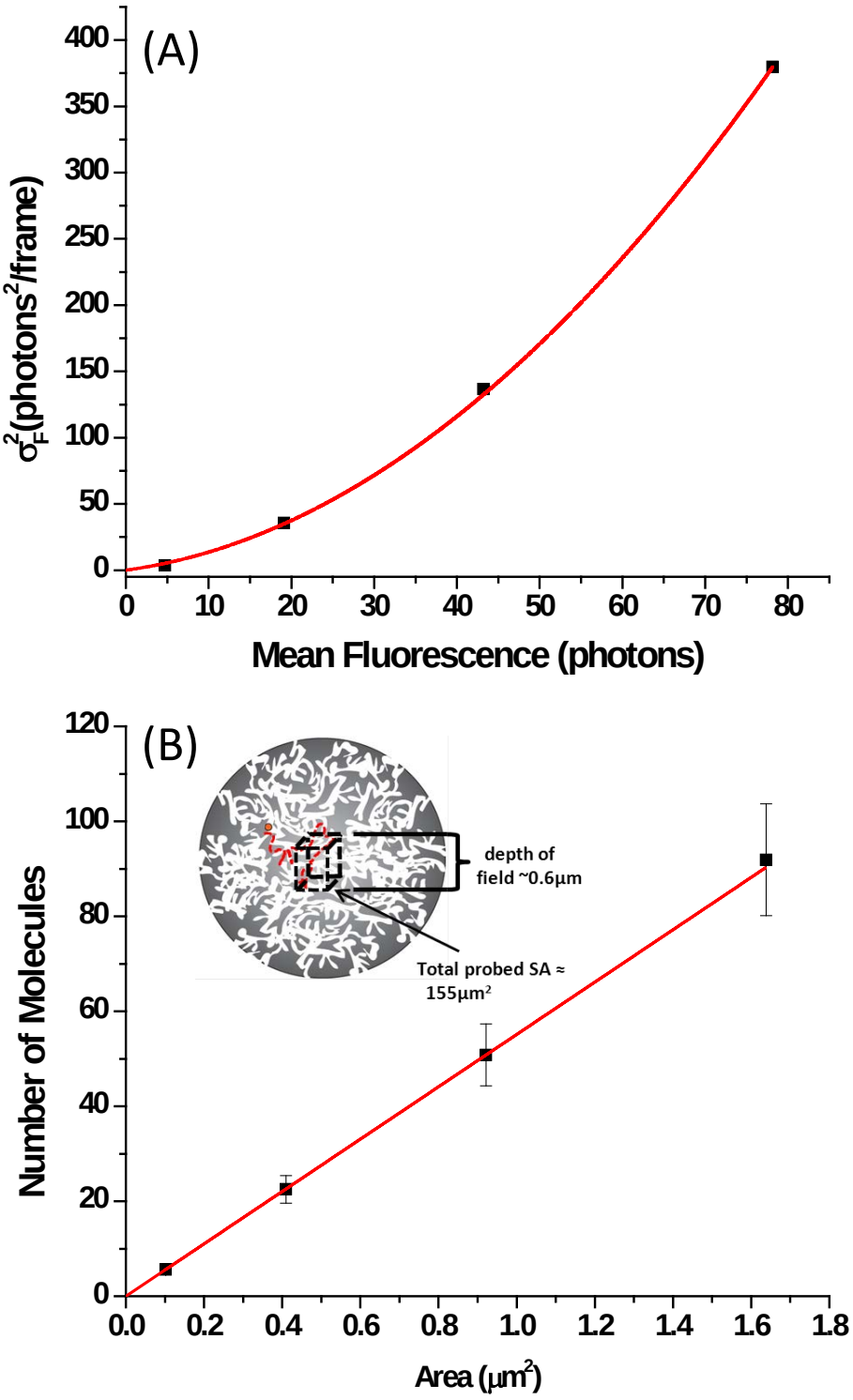

Figure 4.3. Determination of the photon count rate, *k*, and the DiI surface concentration. (A) Plots of variance in fluorescence versus mean fluorescence signal for varying probing region sizes fit to Equation 4.4, for DiI diffusion within Zorbax ODS chromatographic particle. (B) Number of molecules versus area of probing region, with linear fit.

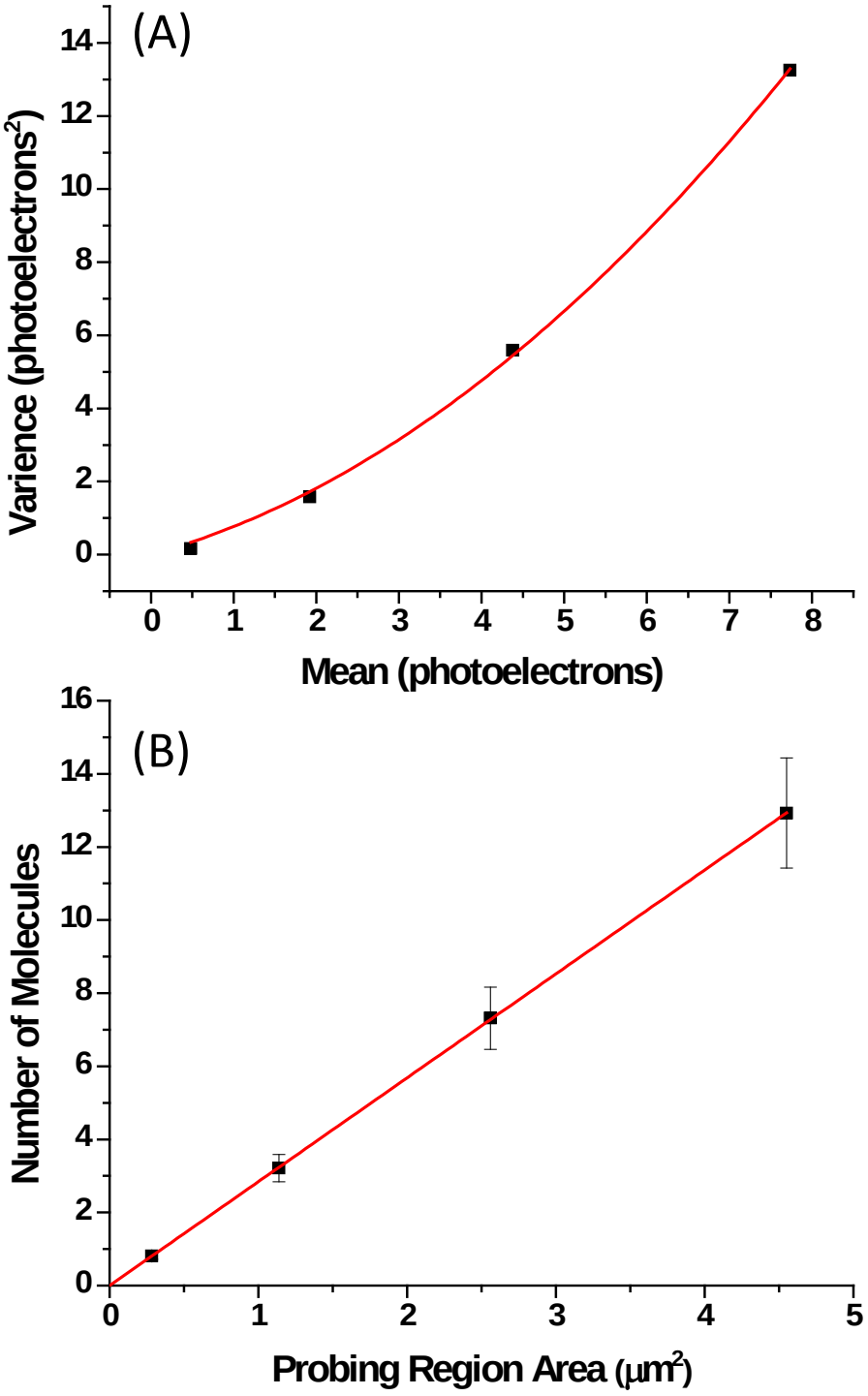

Figure 4.4. Determination of the photon count rate, *k*, and the DiI surface concentration. (A) Plots of variance in fluorescence versus mean fluorescence signal for varying probing region sizes fit to Equation 4.4, for DiI diffusion on C_{18} (squares, red line) (B) Number of molecules versus area of probing region, with linear fits for the two surfaces.

isotherm region), the apparent adsorption to the porous silica surface is 388-times greater than the planar interface.

While small differences in C_{18}-surface affinity might arise from differences in the density of C_{18} ligands, the greatest contributor to the much larger apparent DiI population observed in the particles should be due to the large difference in the actual surface area within the probing region for a planar surface compared to the large surface area in the particle projected onto two dimensions. The surface area imaged on the CCD camera from a planar surface is simply the sampled area of the camera divided by the magnification, which for an 8x8 pixel region at 100x is 1.64 μm^2. However, the total surface area sampled within the chromatographic silica particle is a volume bounded by the sampled region in the xy-plane and by the depth of field of the microscope objective in the z-dimension (Figure 4.3 inset). The depth of field is the region above and below the focal plane within which objects remain in focus, where $DOF = \lambda n/NA^2$.[38] For the 1.49 NA objective, the depth of field is ~0.6 μm, resulting in a total probed volume of 0.98 μm^3 for the 8x8 (1.64 μm^2). For the reversed-phase chromatographic silica particles, the specific surface area (146 m^2/g) and average density (1.1 g/cm^3) from the BET-measured pore volume (0.31 cm^3/g) and the density of solid fused silica (2.2 g/cm^3) predicts a surface area within an 8x8 pixel sampled region of 155 μm^2, which is 95-times larger than its projection onto the detector. Thus the number of molecules counted in the porous particle must be divided by this factor to account for the greater surface area being sampled to predict the surface concentration on an equivalent planar surface.

Correcting the slope of the line in Figure 4.3b for the greater surface area sampled within a particle and multiplying by a factor 20 to account for the 20-fold higher solution

concentration of DiI needed for the planar surface experiments predicts a DiI surface concentration on the chromatographic silica surface (adsorbed from a 20 pM solution) of 11.5 (±0.1) molecules/μm^2. This surface concentration is comparable to (4.0-times larger) than DiI 2.84 (±0.008) molecules/μm^2 on a C_{18}-modified planar glass surface. The fairly close agreement between the populations of DiI on these two surfaces is reassuring, indicating that retention of molecules on reversed-phase chromatographic silica can indeed be represented by planar surface models, within a factor of 4 in the sorption equilibrium constant. The higher partitioning of DiI onto the chromatographic reversed-phase silica surface is likely due to differences in chain density, conformation, and solvation of the C_{18} ligands bound to a porous silica substrate versus ligands bound to a planar substrate.

4.3.4 Surface diffusion rates at porous-particle versus planar-surfaces

A significant issue with understanding *intraparticle* molecular transport is that it can involve both diffusion of the analyte adsorbed to the pore-wall surfaces and solution diffusion through the mobile-phase within the particle.[3] The measured diffusion rate represents the average of the two diffusional processes weighted by the fraction of time spent by the analyte in each phase. The fraction of time an analyte spends adsorbed to the surface is estimated from the capacity factor, *k'*, defined as the ratio of the number of analyte molecules in the stationary phase to those in the mobile phase, N_s/N_m. The total number of molecules for each probed volume of the particle, N_T, was determined above, and these represent the total number of molecules, $N_T = N_s + N_m$, in the stationary phase, N_s, and the intraparticle mobile phase, N_m. The number of molecules in the intraparticle

mobile phase can be calculated from the solution concentration of DiI and the void fraction of the particle within the probed volume, which in the case of 1-pM DiI measured within the 8x8 pixel region is N_m = 5.4x10^{-4} molecules. This value N_m is a very small fraction of N_T = 91.8 ± 0.3 for this case, so it can be assumed that $N_T \approx N_s$ and the capacity factor k' = N_s/N_m ~ 1.7 x 10^5, within a factor of 2 predicted by adsorption and desorption rates above. Under these very high retention conditions, analyte molecules within a particle spend effectively all (99.999%) of their time adsorbed to the stationary phase surface; thus the mobile phase diffusion component of the intraparticle transport can be neglected. This situation allows a direct comparison of measured intraparticle diffusion coefficients to surface diffusion coefficients at planar interfaces.

The apparent diffusion rate of DiI measured within the chromatographic silica particles was measured above (Figure 4.1b) to be 1.8 ± 0.4 x 10^{-9} cm^2/s, which is approximately 36-times slower than DiI diffusion at the planar surface. From Einstein's relation for diffusion in two dimensions (Equation 4.3),[32,39] the time constant for diffusional relaxation is proportional to the *area* explored by the molecule within the probed region. For molecules diffusing at a planar surface, the area over which they diffuse is defined by the probed region (convoluted with the point spread function), the radius squared of which is 1.68 μm^2 in the case of a 8x8 pixel sampled region. For molecules are diffusing on the *interior* surfaces of a porous particle; however, the surface area explored by the molecule during its trajectory is much larger than the projection of that area onto a two-dimensional image in the microscope. Diffusing molecules adsorbed to the interior surfaces of the particle must follow the tortuous contours of the high surface area porous network. This surface diffusion takes place in three dimensions over

a much larger area than is projected in two dimensions on the CCD camera. The diffusion rate measured by the camera reports the rate at which molecules move into and out of the particle on a macroscopic, two-dimensional scale[25]; that diffusion is not the rate at which molecules diffuse with respect to the *interior surfaces* of the particle on a molecular scale.

To estimate the rate of diffusion with respect to the interior surface, knowledge of the surface area explored by molecules while traversing the probing region is required, which can be gained by estimating the overall volume explored by diffusing molecules. From Equation 4.3, $\tau_{1/2}$ is the characteristic time for molecules with an apparent diffusion coefficient in the particle, D_p, to diffuse across a *probed* region of macroscopic area, $A_p = \omega^2$. Because intraparticle molecular transport is homogenous, where molecular trajectories and spatial distributions well modeled by a random walk in three dimensions,[25] displacements in each orthogonal dimension on distance scales larger than the pore structure are independent and equivalent, where $r = \sqrt{2D_p t}$. Thus, in a given time of $\tau_{1/2}$, molecules executing a 3-D random walk would also undergo a random displacement in the z-dimension of $r_z = \sqrt{2D_p \tau_{1/2}}$, which in turn defines a volume, $V_p = A_p r_z$, which molecules explore during the time $\tau_{1/2}$. The *total interior surface area* over which molecules diffuse, S_i, contained within the volume $A_p r_z$ is given by

$$S_i = \rho A_p r_z S_{spec} \qquad [5.5]$$

where ρ is the particle density and S_{spec} is the specific surface area. In the present experiment, detectable radial displacements in the z-direction, r_z, have an upper bound given by half the depth of field, *DOF*/2, which impacts S_i at longer relaxation times.

Using this concept to estimate the interior surface area, S_i, explored by a DiI molecule within the porous chromatographic particle for a given probed area, A_p, one can plot of the relaxation rate, $1/\tau_{1/2}$, versus $1/S_i$, which is shown in Figure 4.5. The slope of this plot is four-times the *interior surface* diffusion coefficient, D_i = 8.6 (±0.2) x 10^{-8} cm^2/s, which is 1.32-times faster than the DiI diffusion coefficient measured at the planar C_{18} model surface. The fairly close agreement between the diffusion coefficient of DiI measured on the interior surface of a particle and that observed on a planar model surface is again reassuring, indicating that the interfacial dynamics molecules in reversed-phase chromatographic silica can indeed be represented by planar surface models where only 26% difference in the diffusion coefficient is observed between the authentic particle and the model surface. This relatively small difference could arise from differences in the bound C_{18} ligand density or conformations. Previous studies have shown that retention of nonpolar compounds tends to scale with bonded-phase loading or ligand density.[40] Furthermore, it has been shown that increased reversed-phase ligand density results in faster analyte diffusion rates, possibly due to a more homogenous and continuous bonded phase on the high density surfaces.[12] Thus, assuming a more complete derivatization and higher n-alkane surface density on the commercially prepared chromatographic media, as evidenced by its higher retention (as determined above), the diffusion behavior behaves as predicted and is more rapid compared to the lower retention planar reversed-phase surface.

Another possible explanation for the faster diffusion rates observed within the particles compared to the planar surface could arise from a smaller internal surface area sampled by the DiI probe molecules compared to N_2 molecules used in the BET isotherm

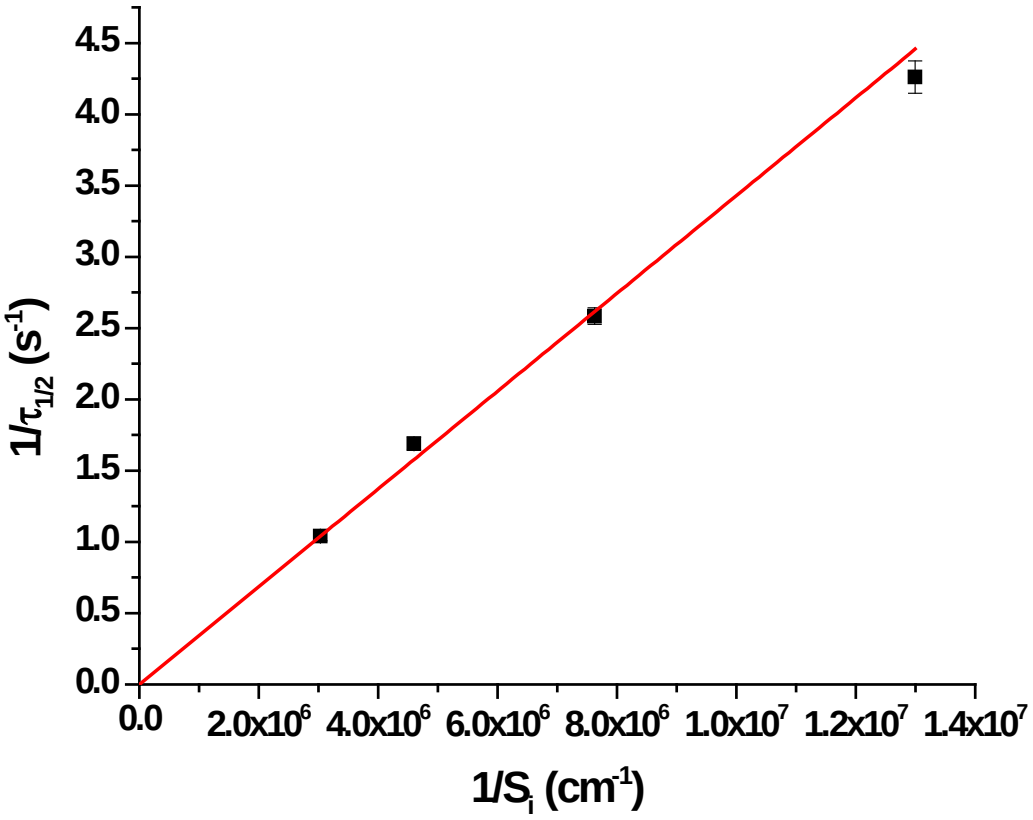

Figure 4.5. Plot of the inverse decay constant versus the inverse total interior surface area contained within the volume explored by molecules diffusing within a particle during a time of $\tau_{1/2}$, with a linear fit.

measurement of the specific surface area of the chromatographic particles. Due to the larger size of DiI molecules compared with N_2, DiI would not be able to sample small surface structures accessible to N_2, resulting in a smaller actual surface area than derives from the nitrogen adsorption analysis. This would artificially inflate the diffusion coefficient calculated for DiI using the larger N_2-BET derived surface area. In either case, it is clear that taking into account the larger probed surface area in the case of porous particles and scaling the effective diffusion coefficients accordingly is key to measuring surface diffusion within porous chromatographic media by spectroscopic techniques.

4.3.5 Summary and conclusions

In this work, a comparison is made between analyte transport and retention made within actual reversed-phase chromatographic silica particles and C_{18}-modified planar surfaces used as models for reversed-phase chromatographic interfaces. Historically, spectroscopic based studies of analyte transport and retention at chromatographic interfaces have been conducted on planar models due to their ease in being adapted to fluorescence microscopy. However, C_{18}-modified planar substrates can differ from actual chromatographic porous silica gel in both surface chemistry and transport geometry. Imaging-FCS was used to measure the diffusion coefficients and quantify surface populations of the fluorescent probe DiI within actual reversed-phase chromatographic silica particles and at C_{18}-modifed glass coverslips. The surface density of DiI was initially found to be almost a factor of 400 larger within the particles than those found on planar interfaces. However, after considering the increased surface area within the particle probed by the detection volume of the instrumentation, it was found

that the surface densities measured within the particle were actually within a factor of 4 larger than those measured on the planar chromatographic model interfaces. This factor can be explained by differences in derivatization, and thus surface chemistry, in the commercial chromatographic particles that result in higher retention. Furthermore, the actual diffusion coefficient of DiI with respect to the interior surface area was calculated by accounting for the volume the molecules explore during the characteristic diffusion time obtained from the autocorrelation analysis. The interior surface transport rate was found to be within a factor of 1.32 of that measured on the planar models.

4.4 References

(1) Iler, R. K. *The Chemistry of Silica: Solubility, Polymerization, Colloid and Surface Properties and Biochemistry of Silica*; Wiley: New York, 1979.

(2) Giddings, J. C. *Unified Separation Science*; Wiley: New York, 1991.

(3) Miyabe, K.; Guiochon, G. *J. Chromatogr. A* **2010**, *1217*, 1713.

(4) Guan-Sajonz, H.; Sajonz, P.; Zhong, G.; Guiochon, G. *Biotechnol. Progr.* **1996**, *12*, 380.

(5) Miyabe, K.; Guiochon, G. *J. Chromatogr. A* **2000**, *890*, 211.

(6) Gowanlock, D.; Bailey, R.; Cantwell, F. F. *J. Chromatogr. A* **1996**, *726*, 1.

(7) Li, J.; Cantwell, F. F. *J. Chromatogr. A* **1996**, *726*, 37.

(8) Gritti, F.; Guiochon, G. *Anal. Chem.* **2006**, *78*, 5329.

(9) Miyabe, K.; Guiochon, G. *J. Phys. Chem. B* **1999**, *103*, 11086.

(10) Miyabe, K.; Guiochon, G. *J. Chromatogr. A* **2002**, *961*, 23.

(11) Hansen, R. L.; Harris, J. M. *Anal. Chem.* **1995**, *67*, 492.

(12) Hansen, R. L.; Harris, J. M. *Anal. Chem.* **1996**, *68*, 2879.

(13) Hansen, R. L.; Harris, J. M. *Anal. Chem.* **1998**, *70*, 2565.

(14) Hansen, R. L.; Harris, J. M. *Anal. Chem.* **1998**, *70*, 4247.

(15) Wirth, M. J.; Swinton, D. J.; Ludes, M. D. *J. Phys. Chem. B* **2003**, *107*, 6258.

(16) Swinton, D. J.; Wirth, M. J. *Anal. Chem.* **2000**, *72*, 3725.

(17) McCain, K. S.; Harris, J. M. *Anal. Chem.* **2003**, *75*, 3616.

(18) McCain, K. S.; Hanley, D. C.; Harris, J. M. *Anal. Chem.* **2003**, *75*, 4351.

(19) Fu, Y.; Ye, F.; Sanders, W. G.; Collinson, M. M.; Higgins, D. A. *J. Phys. Chem. B* **2006**, *110*, 9164.

(20) Ye, F.; Higgins, D. A.; Collinson, M. M. *J. Phys. Chem. C* **2007**, *111*, 6772.

(21) Ye, F.; Collinson, M. M.; Higgins, D. A. *PCCP* **2009**, *11*, 66.

(22) Brinker, C. J.; Scherer, G. W. *Sol-Gel Science: The Physics and Chemistry of Sol-Gel Processing*; Academic Press: Boston, 1990.

(23) Unger, K. K. *Porous Silica: Its Properties and Use as Support in Column Liquid Chromatography*; Elsevier Science: Amsterdam, 1979.

(24) Zhong, Z.; Lowry, M.; Wang, G.; Geng, L. *Anal. Chem.* **2005**, *77*, 2303.

(25) Cooper, J. T.; Peterson, E. M.; Harris, J. M. *Anal. Chem.* **2013**.

(26) Burkhardt, M.; Schwille, P. *Opt. Express* **2006**, *14*, 5013.

(27) Kannan, B.; Har, J. Y.; Liu, P.; Maruyama, I.; Ding, J. L.; Wohland, T. *Anal. Chem.* **2006**, *78*, 3444.

(28) Sankaran, J.; Bag, N.; Kraut, R. S.; Wohland, T. *Anal. Chem.* **2013**, *85*, 3948.

(29) Cooper, J. T.; Harris, J. M. *Anal. Chem.* **2014**, *86*, 7618.

(30) Wirth, M. J.; Fatunmbi, H. O. *Anal. Chem.* **1992**, *64*, 2783.

(31) Olson, L. G.; Lo, Y.-S.; Beebe; Harris, J. M. *Anal. Chem.* **2001**, *73*, 4268.

(32) Elson, E. L.; Magde, D. *Biopolymers* **1974**, *13*, 1.

(33) Boening, D.; Groemer, T. W.; Klingauf, J. *Opt. Express* **2010**, *18*, 13516.

(34) Koppel, D. E. *Phys. Rev. A* **1974**, *10*, 1938.

(35) Wirth, M. J.; Ludes, M. D.; Swinton, D. J. *Anal. Chem.* **1999**, *71*, 3911.

(36) Zulli, S. L.; Kovaleski, J. M.; Zhu, X. R.; Harris, J. M.; Wirth, M. J. *Anal. Chem.* **1994**, *66*, 1708.

(37) Hansen, W. N. *J. Opt. Soc. Am.* **1968**, *58*, 380.

(38) Corle, T. R. *Confocal Scanning Optical Microscopy and Related Imaging Systems* Academic Press: San Diego, 1996.

(39) Berg, H. C. *Random Walks in Biology*; Princeton University Press: Princeton, 1993.

(40) Wise, S. A.; Sander, L. C. *HRC & CC, J. High Resolut. Chromatogr. Chromatogr. Commun.* **1985**, *8*, 248.

CHAPTER 5

CONCLUSIONS AND FUTURE WORK

5.1 Conclusions and Future Work

Single-molecule fluorescence imaging and tracking was used to measure the trajectories of molecules visiting chromatographic porous silica particles. This approach proved to be a versatile technique to measure kinetic information such as the intraparticle diffusion coefficient, residence times, and the spatial distribution of molecules within the particles. The wide-field high resolution associated with imaging was also used to develop statistical spatial criteria to distinguish moving molecules from stationary molecules. This yielded the ability to divide molecular trajectories into moving events and stuck events and characterize them independently to determine how each transport behavior influences residence times within the particle. Residence times of molecules that exhibit no stuck events were found to be indistinguishable from residence times of simulated molecular trajectories undergoing a three-dimensional random walk with the measured intraparticle diffusion coefficient. This is an important result that indicates that the internal porous structure, as well as the transport of molecules through the structure, is homogenous in three dimensions within the spatial and temporal resolution of our experiment. This is in agreement with studies of the porous structure of silica xerogels conducted via electron microscopy or neutron scattering.[1,2] Furthermore, the predictive ability of the random walk based Monte Carlo simulation could be extended to model

chromatographic media with varying porous structure. One example would be core-shell chromatographic media, where the chromatographic particles are comprised of a solid silica core surrounded by a porous silica shell in order to mitigate retention time dispersion from varying diffusional path lengths through the interior of the particle.[3,4] Preliminary results indicate that the majority of molecules do not penetrate into the interior of fully porous particles. Thus to significantly affect residence times, core diameters must be large with respect to the thickness of the outer porous shell.

Single-molecule imaging microscopy can also characterize strong adsorption events, which has potential for application in the development of improved chromatographic media. Strong adsorption events have been linked to chromatographic peak asymmetry[5–7] and are likley to be caused by defect sites in the underlying silica that produce free *active* silanols and bind organic bases more strongly than the C_{18} layer.[8–11] The spatial histogram of stuck events confirms that there are specific locations where an anomalous number of strong adsorption events are occurring, probably due to the underlying chemistry of the modified silica. Furthermore, the intraparticle residence time of molecules that become strongly adsorbed is an order of magnitude greater than those that do not. This stuck molecule analysis has potential for use as a stationary phase characterization method to gauge the efficacy of the derivitization process and to determine the strong adsorption behavior and its dependence on the surface chemistry. Preliminary experiments have been conducted on endcapped versus nonendcapped stationary phase media, where endcapping involves the back filling of the stationary phase with smaller molecular-weight silanes to reduce the number of free silanols left unreacted due to steric hindrance by the primary stationary phase ligand. Results show

that endcapping drastically reduces both the number of strong adsorption sites and residence times for the detected stuck molecules.

Imaging-fluorescence correlation spectroscopy was used to measure the surface dynamics of amphiphilic fluorescent probe molecules (DiI) at model (planar) reversed-phase chromatographic interfaces. The use of a small region of a CCD camera as the detector proved to be advantageous and allowed for measurement of rapid diffusion with fast time resolution and the simultaneous measurement of diffusion and sorption kinetics through control of the probing region size. Surface transport rates, adsorption-desorption kinetics, and DiI adsorption equilibrium constants were measured at both C_{18}- and C_1-modifed interfaces and compared. Compared to the C_{18} interface, surface diffusion was found to be much faster (~5X) at the C_1 interface where hydrophobic interactions between the amphiphillic probe molecule and the surface ligands are minimized. The adsorption equilibrium constant followed the opposite trend where the decreased hydrophobic interactions at the C_1 interface resulted in decreased retention of molecules at the surface (~2X). The dependence of the surface diffusion coefficient on the retention equilibria is still poorly understood,[12] and these experiments suggest that the dependence may be nonlinear. Future studies could exploit the high kinetic dynamic range of imaging-FCS to probe the dependence of diffusion and adsorption-desorption rates on a wide range of retention conditions by varying the n-alkane chain length, surface density, or overlaying solvent conditions.

In this work, the ability to measure molecular transport and interaction kinetics was demonstrated within actual reversed-phase chromatographic particles. The imaging-FCS studies presented here represented the typical experimental geometry for

spectroscopic based studies of reversed-phase chromatographic interfaces conducted on model planar surfaces consisting of reversed-phase modified glass or fused silica. A study was thus undertaken to compare transport and adsorption-desorption kinetics measured both at planar model chromatographic interfaces and within actual porous chromatographic media. Measured diffusion rates between the two systems were in reasonable agreement with each other when the intraparticle diffusion coefficient was scaled by the increased surface area encountered by molecules within the three-dimensional porous structure within particles versus on a planar surface. These results shed light on the effect that the porous network has on the observed transport within the particle. Molecules diffuse with approximately the same rate along the surface on the molecular scale. However, the pore surface within the particle is tortuous and extends in three dimensions; thus molecular diffusion along the tortuous surface produces a slower effective diffusion in the particles over longer distance scales. This is the surface diffusion analogue of the tortuosity factor, used in characterization of chromatographic material, which compares the effective intraparticle diffusion coefficient to the free solution diffusion rate of the analyte.[13] Furthermore, the results indicate that planar interfaces are reasonable models of porous chromatographic media for characterizing diffusion over molecular scale distances.

Single-molecule fluorescence microscopy techniques were adapted and applied to measuring the interaction and transport of molecules at reversed-phase chromatographic interfaces. The technique was successfully applied to measuring analyte interactions within actual reversed-phase chromatographic porous silica particles, measuring fast interfacial kinetics at model planar interfaces and comparing results between the two

systems. Intraparticle molecular transport is known to play a significant role in the resolution and separation efficiency of reversed-phase chromatographic techniques. This research provides unprecedented information regarding the transport of individual molecules at model chromatographic interfaces and within actual porous silica particles and yields insight into the timescale of fundamental processes that govern chromatographic separations. Agreement between experimental data and simulation also demonstrates the potential of this technique to be extended to other systems where molecular transport within particles is of fundamental importance including solid-phase extraction, biomolecule immobilization, supported catalysts, and particle based sensors. Furthermore, as applications of porous materials continue to increase, this technique has potential to be the standard method for interrogation of molecular processes within these materials.

5.2 References

(1) Glinka, C. J.; Sander, L. C.; Wise, S. A.; Hunnicutt, M. L.; Lochmuller, C. H. *Anal. Chem.* **1985**, *57*, 2079.

(2) Longman, G. W.; Wignall, G. D.; Hemming, M.; Dawkins, J. V. *Colloid. Polym. Sci.* **1974**, *252*, 298.

(3) Cunliffe, J. M.; Maloney, T. D. *J. Sep. Sci.* **2007**, *30*, 3104.

(4) Gritti, F.; Cavazzini, A.; Marchetti, N.; Guiochon, G. *J. Chromatogr. A* **2007**, *1157*, 289.

(5) Fornstedt, T.; Zhong, G.; Guiochon, G. *J. Chromatogr. A* **1996**, *741*, 1.

(6) Giddings, J. C. *Anal. Chem.* **1963**, *35*, 1999.

(7) Giddings, J. C. *Dynamics of Chromatography*; Marcel Dekker: New York, 1965.

(8) Wirth, M. J.; Swinton, D. J. *Anal. Chem.* **1998**, *70*, 5264.

(9) Wirth, M. J.; Ludes, M. D.; Swinton, D. J. *Anal. Chem.* **1999**, *71*, 3911.

(10) Wirth, M. J.; Swinton, D. J.; Ludes, M. D. *J. Phys. Chem. B* **2003**, *107*, 6258.

(11) Wirth, M. J.; Legg, M. A. *Annu. Rev. Phys. Chem.* **2007**, *58*, 489.

(12) Miyabe, K.; Guiochon, G. *J. Chromatogr. A* **2010**, *1217*, 1713.

(13) Barrande, M.; Bouchet, R.; Denoyel, R. *Anal. Chem.* **2007**, *79*, 9115.